August 1973 LMSC-D352320

UNSTEADY AERODYNAMIC ANALYSIS OF SPACE SHUTTLE VEHICLES

Part II: STEADY AND UNSTEADY AERODYNAMICS OF SHARP-EDGED DELTA WINGS

Final Technical Report

Prepared by
Lars E. Ericsson
Consulting Engineer, Engineering Technology
J. Peter Reding
Research Specialist, Aero-Thermodynamics

Prepared Under Contract NAS 8-28130
for
National Aeronautics and Space Administration

Lockheed MISSILES & SPACE COMPANY, INC.
SUNNYVALE, CALIFORNIA

UNSTEADY AERODYNAMIC ANALYSIS OF SPACE SHUTTLE VEHICLES

Part II: STEADY AND UNSTEADY AERODYNAMICS OF SHARP-EDGED DELTA WINGS

by
Lars E. Ericsson and J. Peter Reding

August 1973

Prepared Under Contract NAS 8-28130
for
National Aeronautics and Space Administration

Lockheed Missiles & Space Company, Inc.
A Subsidiary of Lockheed Aircraft Corporation
Sunnyvale, California

ABSTRACT

An analysis of the steady and unsteady aerodynamics of sharp-edged slender wings has been performed. The results show that slender wing theory can be modified to give the potential flow static and dynamic characteristics in incompressible flow. A semiempirical approximation is developed for the vortex-induced loads, and it is shown that the analytic approximation for sharp-edged slender wings gives good prediction of experimentally determined steady and unsteady aerodynamics at M = 0 and M = 1. The predictions are good not only for delta wings but also for so-called arrow and diamond wings. The results indicate that the effects of delta planform lifting surfaces can be included in a simple manner when determining elastic launch vehicle dynamic characteristics.

CONTENTS

			Page
		Abstract	ii
Section 1		Introduction	1-1
Section 2		Discussion	2-1
	2.1	Static Characteristics	2-1
		2.1.1 Comparison with Experiments	2-7
		2.1.2 Sideslip Effects	2-11
	2.2	Unsteady Aerodynamic Characteristics	2-16
		2.2.1 Attached Flow	2-16
		2.2.2 Separated Flow	2-24
		2.2.3 Comparison with Experimental Data	2-35
		2.2.4 Lateral Stability Characteristics	2-42
Section 3		Conclusions	3-1
Section 4		Recommendations for Future Study	4-1
		References	R-1
Appendix A		Nomenclature	A-1

PRECEDING PAGE BLANK NOT FILMED

PRECEDING PAGE BLANK NOT FILMED

ILLUSTRATIONS

Figure		Page
1.	Attached Flow Lift Factor K_p of Delta Wings at M = 0	2-45
2.	Definition of Slender Wing Geometry for Strip Load Computation	2-46
3.	Universal Scaling of Delta Wing Lift	2-47
4.	Pressure Distribution on an A = 1 Sharp-Edged Delta Wing at $\alpha = 20.5^\circ$ and M = 0	2-48
5.	Effect of Secondary and Tertiary Flow Separation on Spanwise Pressure Distribution on an A = 1 Delta Wing at $\alpha = 20.5^\circ$ and M = 0	2-49
6.	Lift Distribution Components on an A = 1.147 Delta Wing	2-50
7.	Attached Flow Load Distribution	2-51
8.	Leading Edge Vortex Trajectories on an A = 1 Sharp-Edged Delta Wing (Ref. 19)	2-52
9.	Low Speed Aerodynamic Characteristics of Sharp-Edged Wings with 74° Leading Edge Sweep	2-53
10.	High Speed Aerodynamic Characteristics of Sharp-Edged Wings with 74° Leading Edge Sweep	2-55
11.	Variation of C_m with C_L for Sharp-Edged Slender Delta Wings	2-57
12.	C_m (C_L) Data for a Sharp-Edged A = 2.3 Delta Wing	2-59
13.	Effect of Angle of Attack on the Aerodynamic Center of the Handley-Page-115	2-60
14.	Definition of 6-D Parameters (arrows indicate positive directions of moments, forces, and angles)	2-61
15.	Leading Edge Vortex Position on Sharp-Edged Delta Wings (Ref. 20)	2-62
16.	Roll-Sideslip-Derivatives of Sharp-Edged Wings with 74° Leading Edge Sweep	2-63
17.	Universal Scaling of Roll-Sideslip Derivatives of Sharp-Edged Delta Wings at Low Speeds	2-65

ILLUSTRATIONS (Continued)

Figure		Page
18.	Elastic Vehicle Coordinate System	2-66
19.	Attached Flow Dynamic Stability Derivatives at $\alpha = 0$ and M = 0	2-67
20.	Leading Edge Vortex Formation During Plunge from Zero to Positive Angle of Attack (Ref. 41)	2-68
21.	Transient Vortex Position for the Same α/θ_{LE} (Ref. 41)	2-69
22.	Vortex Paths in Crossflow Plane for 80° Leadinge Edge Sweep (Ref. 41)	2-70
23.	Effect of Stepwise Increase of Angle of Attack (Ref. 41)	2-71
24.	Effect of Stepwise Decrease of Angle of Attack (Ref. 41)	2-73
25.	Suggested Transient Spanwise Lift Distributions (Ref. 41)	2-75
26.	Cyclic Variation of Vortex Height on a Sharp-Edged A = 1 Delta Wing (Ref. 19)	2-76
27.	Effect of Frequency on Cyclic Vortex Height Variation (Ref. 19)	2-78
28.	Karman-Sears Vortex-Wake Lag	2-79
29.	Oscillatory Bending Deformation (Ref. 42)	2-80
30.	Oil Flow Patterns on Undeformed Wing at $\alpha = 5°$ (Ref. 42)	2-81
31.	Spanwise Pressure Distribution for Steady Deformation (Ref. 42)	2-83
32.	Vortices for Cambered Delta Plate with 80° Leading Edge Sweep (Ref. 49)	2-85
33.	Spanwise Distributions of Harmonic Components for Quasi-steady Variation (Ref. 42)	2-86
34.	Polar Diagrams of Amplitude - Phase Angle for Various Spanwise Positions (Ref. 42)	2-87
35.	Deformation Shapes for Vortex Build-up In Steady and Unsteady Case	2-89
36.	Pitch Stability Derivatives for Sharp-Edged Delta Wings at M = 0	2-90
37.	Free Body Vortex Effects on a 12.5° Sharp Cone (Ref. 53)	2-91
38.	Pitch Oscillation Derivatives for Sharp-Edged Delta Wings	2-92
39.	Dynamic Stability Derivatives for Sharp-Edged Delta Wings	2-94

ILLUSTRATIONS (Continued)

Figure		Page
40.	Frequency Effects on Dynamic Derivatives for 1° Pitch Oscillations (Ref. 57)	2-96
41.	Frequency Effects on an A = 0.654 Delta Wing (Ref. 36)	2-98
42.	Effect of Vortex Burst on the Pitch Stability Derivatives of an A = 1.484 Delta Wing	2-99
43.	Effect of Vortex Burst on Static Longitudinal Characteristics of Sharp-Edged Delta Wings (Ref. 60)	2-101
44.	Nonlinear Pitch Stability Characteristics of a Blunt Cylinder-Flare Body at M = 1.05 (Ref. 61)	2-102
45.	Vortex Burst Position on Sharp-Edged Delta Wings (Ref. 66)	2-103
46.	Flight Test Data for C_{ℓ_β} of the Handley Page-115 (Ref. 71)	2-104
47.	Center of Pressure of A = 1 Gothic and Delta Wings (Ref. 7)	2-105
48.	Spanwise Vortex Position at the Trailing Edge of Slender Sharp-Edged Wings (Ref. 72)	2-106
49.	Quasi-Steady Equivalence for a Side-Slipping Delta Wing	2-107
50.	Roll-Induced Vortex Loads on an A = 0.7 Sharp-Edged Delta Wing at α = 0 (Ref. 74)	2-108
51.	Effect of Roll Rate and α_o on the Rolling Moment of an A = 1 Sharp-Edged Delta Wing (Ref. 75)	2-109
52.	Roll Damping of Slender Wings (Ref. 76)	2-110
53.	Slender Aircraft Lateral Stability Characteristics (Ref. 77)	2-111

Section 1
INTRODUCTION

It was clear very early in the space shuttle development that the vehicle design could be critically dependent upon aeroelastic loads (Refs. 1 and 2). NASA Marshall Space Flight Center (MSFC) needed, therefore, to develop analytic methods in time to be applicable to the final space shuttle design. The main problem was that the methods would to a great extent be configuration dependent, and the configuration was changing continually. However, once the large crossrange capability had been decided upon, one design feature has remained fixed. That is, the orbiter will have a delta wing planform of some sort. NASA MSFC concluded, therefore, that analytic or other means would be needed for prediction of unsteady delta wing aerodynamics regardless of future configuration changes.

Based on experience, NASA MSFC asked Lockheed Missiles & Space Company, Inc. (LMSC), to investigate the unsteady aerodynamics of the delta planform space shuttle and try to develop analytic means simple enough to allow inclusion of large delta planform lifting surfaces in the computation of the aeroelastic characteristics of the space shuttle ascent configuration. In order to survive the reentry heating environment, the space shuttle wing will be thick and have large leading edge radius. Before the unsteady aerodynamics of leading edge vortices from the space shuttle wing can be determined, a thorough understanding of sharp-edged delta wing aerodynamics is needed. The present report describes the analysis of sharp-edged delta wings, the results of which are used as a much needed interim step in the development of space shuttle delta wing aerodynamics (Ref. 3).

Section 2
DISCUSSION

The simple flow concept developed by Polhamus, i.e., the "turned-around" leading edge suction, has been remarkably successful in predicting the nonlinear lift generated by the leading edge vortex on slender wings at high angles of attack (Ref. 4). This is true not only for simple delta wings, but also for so-called double-deltas, and the method also predicts experimentally observed Mach number effects (Ref. 5). As the vortex lift is in reality dependent upon upstream flow conditions, and the leading edge suction depends only upon local conditions, the flow concept cannot be applied to the unsteady aerodynamics. However, it is a very useful tool for determination of the static loads and is used as a starting point in the present analysis.

2.1 Static Characteristics

Polhamus' expression for the delta wing lift is as follows (Ref. 4).

$$\begin{aligned} C_L &= C_{L,P} + C_{L,V} \\ C_{L,P} &= K_P \sin\alpha \cos^2\alpha \\ C_{L,V} &= K_V \sin^2\alpha \cos\alpha \end{aligned} \tag{1}$$

K_p and K_v are constants determining the magnitudes of attached flow and vortex lift components, respectively. In incompressible flow K_P is almost linearly dependent upon

aspect ratio (see Fig. 1). The deviation between Jones' slender wing theory (Ref. 6) and Polhamus' results are represented as follows in what is called "Present First Approximation" in Fig. 1.

It is assumed that the area denoted A_{TE} in Fig. 2 carries no load in order to account in a crude manner for the delta wing trailing edge condition at M = 0. The result is that the slender wing lift (and normal force) will be reduced by the factor $\cos^2 \theta_{LE}$. That is

$$\begin{aligned} C_{N_\alpha} &= 2 \sin \alpha \cos \alpha \cos^2 \theta_{LE} \ \pi (c_o \tan \theta_{LE})^2 / S \\ &= 2\pi \sin \alpha \cos \alpha \sin^2 \theta_{LE} / (b/2\, c_o) \end{aligned} \tag{2}$$

For a delta wing $b/2\, c_o = A/4 = \tan \theta_{LE}$ and K_p in Eq. (1) becomes

$$K_p = \pi (A/2) / \left[1 + (A/4)^2 \right]$$

which is the "First Approximation" shown in Fig. 1. At $M \geq 1.0$, it is assumed that the area A_{TE} is fully effective, giving $K_p = \pi A/2$, i.e., in agreement with Jones' theory (Ref. 6).

The strip load normal to the leading edge of the slender wing (half) in Fig. 2, giving the total C_{N_α} of Eq. (2), is

$$1/2 \left(d\, C_{N_\alpha} / d_\xi \right)_\perp = \pi \sin 2\alpha \sin^2 \theta_{LE} / (b/2\, c_o) \tag{3}$$

With $C_{L,P} = C_{N_\alpha} \cos \alpha$ from Eq. (3) and $C_{L,V} = \pi \cos \alpha \sin^2 \alpha$ from Eq. (1), one obtains the following for the total lift.

$$C_L/\left(\frac{A}{4}\right)^2 = 2\pi\cos^3\alpha \left[\cos^2\alpha\,\cos^2\theta_{LE}\left(\frac{\tan\alpha}{\tan\theta_{LE}}\right) + \frac{1}{2}\left(\frac{\tan\alpha}{\tan\theta_{LE}}\right)^2\right] \quad (4)$$

That $\tan\alpha/\tan\theta_{LE} \approx \alpha/\theta_{LE}$ should be a pertinent scaling parameter is to be expected from slender cone and slender wing analyses. However, $C_L/\left(\frac{A}{4}\right)^2$ is not a good scaling parameter, probably because of the term $\cos^2\theta_{LE} = \left[\left(1+\left(\frac{A}{4}\right)^2\right]^{-1}\right.$ Based upon Peckham's results (Ref. 7), Eq. (4) was modified and available experimental data for thin, sharp-edged delta wings (Refs. 7 through 12) were plotted in form of

$$C_L/(b/2c_o)^{3/2} = f(\alpha/\theta_{LE}) \quad (5)$$

The results shown in Fig. 3 indicate that Eq. (5) indeed collapses the experimental data to one (preliminary design) curve. The deviations are most likely data scatter, as no consistent θ_{LE}-trend is discernible. Eq. (5) and Fig. 3 will be used later in the discussion of steady and unsteady aerodynamic loads.

The conical flow assumption inherent in all existing theories does not seem to be substantiated by experimental results (Ref. 13), at least not for thin, sharp-edged delta wings (see Fig. 4). Only close to the apex does the pressure distribution agree reasonably well with the best available theory (Ref. 14). Farther aft the pressure level drops from the (constant) conical flow value although the spanwise distribution remains very similar in shape. The deviation is mainly due to secondary and tertiary flow separations (Fig. 5) that have much more prominent effects in a low Reynolds number wind tunnel test than in actual high Reynolds number flight conditions, as is pointed out by Hummel* (Ref. 13). In the flight case the boundary layer over the center wing will not be laminar but turbulent, and the secondary separation and its effects will be much smaller.

The fall-off from the conical flow level of the aft delta wing pressures (Fig. 4) indicates that far downstream from the apex the feeding sheet from the leading edge is changing, and the vortex strength farther aft is no longer growing linearly with ξ. The measured load distributions on a sharp-edged A = 1.147 delta wing at $\alpha = 10^\circ$, 20°, and 30° (Ref. 16) are shown in Fig. 6. Also shown is the attached flow slender wing load distribution defined by Eq. (3). The measured load distribution is fairly well approximated by using a bilinear approximation to the nonlinear vortex-lift distribution, with the break occurring at $\xi = 0.4$.

The trailing-edge-round-off would be obtained, it appears, if the attached load distribution were represented by a more accurate potential flow lift distribution (Refs. 17 and 18), shown as a short-dash line in Fig. 6. Further comparison in this respect is made in Fig. 7, showing that limiting the attached flow lift growth in Eq. (2) to $C_{N_\xi}/C_N = 1.5$ gives better agreement with the distribution given by vortex-lattice methods (Refs. 17 and 18). It is obvious that the aspect ratio should not be

*The existence of this secondary flow separation was shown first by Örnberg (Ref. 15).

much larger than A = 2 when applying the present modified slender wing distribution. Applying this "ceiling" to the lift growth decreases C_{Na} by 9 percent. This is the "Present Second Approximation" for K_p shown in Fig. 1 which is in better agreement with Polhamus' potential flow value. With this modification, Eq. (3) becomes*:

$$1/2\ (d\ C_{Na}/d\ \xi)_L = \frac{\pi \sin 2\ \alpha\ \sin^2 \theta_{LE}}{(b/2c_o)} \times \begin{cases} \xi & : \xi \leq 0.7 \\ 0.7 & : \xi > 0.7 \end{cases} \tag{6}$$

Integration gives

$$\begin{aligned} C_{Na} &= 0.91\ \pi \sin 2\ \alpha\ \sin^2 \theta_{LE}/(b/2c_o) \\ C_{ma} &= -(c_o/\bar{c})\ C_{Na}\ (\bar{\xi}_a - \xi_{CG}) \\ \bar{\xi}_a &= 0.64\ (1 - \Delta \xi_{aTE}) \\ \Delta \xi_{aTE} &= \eta_a \sin^2 \theta_{LE}\ (\eta_a = 4/3\ \pi\text{: elliptic loading}) \end{aligned} \tag{7}$$

For trailing edge sweep ($\theta_{TE} \neq 0$ in Fig. 2), Eq. (7) is modified as follows

$$\begin{aligned} C_{Na} &= 1.4\ \pi\ \xi_a^*\ (0.35\ \xi_a^* + 0.3) \sin 2\ \alpha\ \sin^2 \theta_{LE}/(b/2c_o) \\ C_{ma} &= -(c_o/\bar{c})\ C_{Na}\ (\bar{\xi}_a - \xi_{CG}) \\ (b/2c_o) &= (\cot \theta_{LE} - \tan \theta_{TE})^{-1} \\ \bar{\xi}_a &= \xi_a^*\ (1 - \Delta \xi_{aTE})\ (0.49\ \xi_a^*/3 + 0.51/2)/(0.35\ \xi_a^* + 0.3) \\ \xi_a^* &= \begin{cases} 1 & : \theta_{TE} \geq -\theta_{LE} \\ 1 - \dfrac{\tan \theta_{TE} - \tan \theta_{LE}}{\cot \theta_{LE} - \tan \theta_{TE}} & : \theta_{TE} < -\theta_{LE} \end{cases} \end{aligned} \tag{8}$$

*Still with the strip normal to the leading edge, as defined in Fig. 2.

There is, of course, every reason to believe that the vortex-induced load distribution should have a trailing-edge-round-off effect similar to that for the attached flow loads. As a matter of fact, flow visualization results show the vortices to bend away into the freestream (some 10%) before the trailing edge (see Fig. 8 and Refs. 19 and 20). As pressure measurements of burst indicate that the wing loads will be affected upstream of the visually determined burst location (Ref. 21), the vortex-induced loads will be affected even farther upstream of the trailing edge. To be consistent, the vortex-induced loads are assumed to have the same type of "triangular round-off" as the attached flow loads. The vortex load distribution is determined using delta wing results in which A_{TE} is used in arriving at the final distribution. As the vortex loads are generated close to the leading edge, they will not be sensitive to the change of trailing edge geometry near the centerline. The delta wing results can, therefore, be used to determine the vortex-induced lift distribution also for a swept trailing edge by considering the effective chordwise planform extent at the vortex location, approximately 75% local span ($\bar{\eta}_V \approx 0.75$). Thus, the vortex-induced lift distribution is approximated as shown in the following sketch and Eq. (9)*.

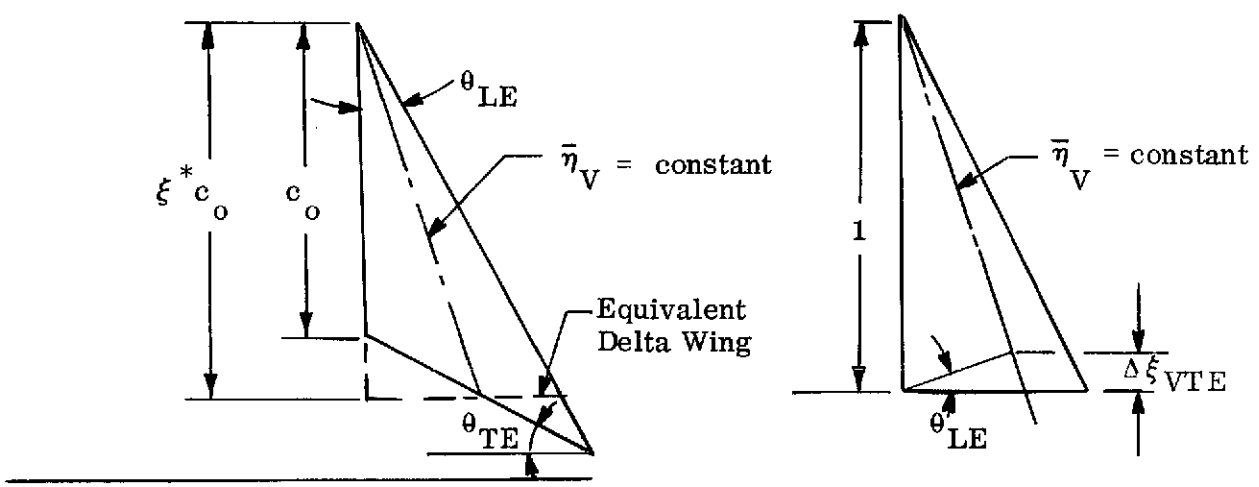

*Also with the strip normal to the leading edge, as shown in Fig. 2.

$$\frac{1}{2}\frac{dC_{NV}}{d\xi} = \begin{cases} 1.72\,\pi\,\xi\,\sin^2\alpha & : \xi \le 0.4 \\ 0.685\,\pi\sin^2\alpha & : 0.4 < \xi \le 0.86\ \xi_V^* \\ 4.92\,\pi\left(1 - \xi / \xi_V^*\right)\sin^2\alpha & : 0.86\ \xi_V^* < \xi \le \xi_V^* \end{cases} \qquad (9)$$

$$\xi_V^* = \left|\cot\theta_{LE} - (1 - \bar{\eta}_V)\tan\theta_{TE}\right| \Big/ \left(\cot\theta_{LE} - \tan\theta_{TE}\right)$$

The integrated total vortex load for a delta wing $\left(\xi_V^* = 1\right)$ is that given by by Polhamus, Eq. (1), with $K_V = \pi$ (Refs. 4 and 5). The capability of Polhamus' leading edge suction analogy to predict the measured vortex-induced lift has been demonstrated very convincingly (Refs. 4 and 5). Eq. (9) only redistributes the lift to fit the experimentally observed lift distribution. After integration, Eq. (9) gives the following loads:

$$C_{NV} = 1.37\,\pi\left(0.93\ \xi_V^* - 0.2\right)\sin^2\alpha$$

$$C_{mV} = -\frac{c_o}{\bar{c}}\,C_{NV}\left(\bar{\xi}_V - \xi_{CG}\right)$$

$$\bar{\xi}_V = \left(1 - \Delta\xi_{VTE}\right)\left(0.435\ \xi_V^{*2} - \frac{0.16}{6}\right) \Big/ \left(0.93\ \xi_V^* - 0.2\right) \qquad (10)$$

$$\Delta\xi_{VTE} = \bar{\eta}_V\,\sin^2\theta_{LE} \qquad (\bar{\eta}_V \approx 0.75)$$

2.1.1 Comparison with Experiments. Extensive experiments have been performed on thin, sharp-edged slender wings with 74° leading edge sweep, in which the trailing edge was swept forward and aft from the delta wing position (Ref. 22). Fig. 9 shows that the present approximation does not worsen the good C_L-prediction

already obtained through Polhaums' theory (Fig. 9a) and that it provides a marked improvement of the C_m-prediction (Fig. 9b). It is worth noting that the present predictions are good regardless of trailing edge sweep, in sharp contrast to the predictions through the leading-edge-suction analogy with its attached-flow-like longitudinal distribution of the vortex-induced loads (Refs. 4, 5, 18, and 19). The experiments reported in Ref. 22 covered the Mach number range $0.2 \leq M \leq 0.8$. The $M = 0.2$ results shown in Fig. 9 can, of course, be compared with the present $M = 0$ predictions. The $M = 0.8$ data could be compared with predictions made for $M \geq 1$ by direct application of Jones' theory (Ref. 6). As only those parts of the wing having increasing cross sectional area will produce lift, only the delta planform is efficient, and sweeping the trailing edge forward or back is detrimental to the same degree. The attached flow results are

$$C_{Na} = \begin{cases} \pi \sin 2\alpha / (\cot \theta_{LE} - \tan \theta_{TE}) & : \theta_{TE} \leq 0 \\ \pi \sin 2\alpha \tan^2 \theta_{LE} (\cot \theta_{LE} - \tan \theta_{TE}) & : \theta_{TE} > 0 \end{cases}$$

$$C_{ma} = \begin{cases} -\left(c_o/\bar{c}\right) C_{Na} \left[\left(2/3\right) \cot \theta_{LE} / (\cot \theta_{LE} - \tan \theta_{TE}) - \xi_{CG} \right] & : \theta_{TE} \leq 0 \\ -\left(c_o/\bar{c}\right) C_{Na} \left[\left(2/3\right) - \xi_{CG} \right] & : \theta_{TE} > 0 \end{cases} \quad (11)$$

The vortex-induced loads increase (by 9% for $\theta_{LE} = 16^\circ$) as the tail-round-off is not present at $M = 1.0$, consistent with the attached flow loads defined by Eq. (11). The moment increases more than the lift as $\Delta \xi_{TE} = 0$. One obtains the following definition of vortex-induced characteristics at $M \geq 1$:

$$
\begin{aligned}
C_{NV} &= 1.37\,\pi\left(\xi_V^* - 0.2\right)\,\sin^2\alpha \\
C_{mV} &= -\frac{c_o}{c}\,C_{NV}\left(\bar{\xi}_V - \xi_{CG}\right) \\
\bar{\xi}_V &= \left(\xi_V^{*2} - \frac{0.16}{3}\right)\Big/ 2\left(\xi_V^* - 0.2\right) \\
\xi_V^* &= \frac{\cot\theta_{LE} - (1-\bar{\eta}_V)\tan\theta_{TE}}{\cot\theta_{LE} - \tan\theta_{TE}}
\end{aligned}
\tag{12}
$$

Figure 10 shows that the M = 1 predictions compare fairly well with the M = 0.8 experimental results (Ref. 22), but not quite as well as the earlier M = 0 predictions compared with the M = 0.2 data (Fig. 9). The reason may well be that M = 0.8 is still subsonic and should have trailing-edge-round-off effects. This is consistent with the overprediction of the lift for the delta wing at M = 0.8 and the good predictions for the diamond wing with its small A_{TE}. Note that the effect of Mach number is large. The pitching moment of the delta wing is increased in magnitude by 75% when the Mach number is increased from M = 0.2 to M = 0.8 and the corresponding value for the arrowhead wing is close to 400%.

The experimental data were obtained using a sting-mounted model, and one has to be somewhat concerned about sting interference, especially in regard to the effects of trailing edge sweep. It appears, however, that the sting used in the test (Ref. 22) was small enough that sting interference should be negligible (Ref. 23). This is at least true for the static results just discussed. In the case of dynamic tests, sting interference is much more difficult to avoid (Ref. 24).

The main difference between the present analysis and available theories is the assumption that the vortex lift distribution deviates substantially from the attached flow load distribution. This has an especially large effect on the $C_m(C_L)$-characteristics and these will now be examined in more detail.

From Eqs. (8) and (10) is obtained:

$$C_m/C_N = (c_o/c)\left[\xi_{CG} - \bar{\xi}_a + (\bar{\xi}_a - \xi_V)(C_{NV}/C_{Na})/(1 + C_{NV}/C_{Na})\right]$$

$$C_{NV}/C_{Na} = \left[0.49\,(0.93\,\xi_V^* - 0.2)\tan\alpha/\xi_a^*\,(0.35\,\xi_a^* + 0.3)\right] \Big/ \sin^2\theta_{LE}\,(\cot\theta_{LE} - \tan\theta_{TE}) \qquad (13)$$

For very slender delta wings, where $\theta_{TE} = 0$ and $\cos\theta_{LE} \approx 1$, C_{NV}/C_{Na} becomes

$$C_{NV}/C_{Na} = 0.55\tan\alpha/\tan\theta_{LE} \approx 0.55\,(\alpha/\theta_{LE}) \qquad (14)$$

When the vortex lift first starts to affect the stability, C_{NV}/C_{Na} is small (compared to unity) and Eq. (13) can be approximated as follows:

$$\frac{C_m}{C_N} = \frac{c_o}{\bar{c}}\left[\xi_{C_G} - \bar{\xi}_a + \left(\bar{\xi}_a - \bar{\xi}_V\right)\,0.55\,\left(\frac{\alpha}{\theta_{LE}}\right)\right] \qquad (15)$$

That is, the vortex lift decreases the pitch stability at a rate that increases linearly with angle of attack. This effect has been observed in a series of dynamic tests, the results of which are discussed in detail later.

With $C_m/C_L = (C_m/C_N)/\cos\alpha$, Eq. (13) gives predictions that compare well with experimental data (Refs. 7, 16, and 22) (see Fig. 11). The present approximation is a decided improvement over the results obtained by strict application of the leading-edge-suction analogy (Refs. 4 and 18). Even for the somewhat large aspect ratio A = 2.3 (see Fig. 7), the predictions agree rather well with experimental trends (Ref. 25) (see Fig. 12). The main disagreement is caused by vortex breakdown for $C_L > 0.6$ ($\alpha > 14^\circ$). The vortex burst moves fast forward of midchord (Refs. 25 and 26), giving the increasing stability trend of the experimental data, in contrast to the predicted decreasing stability.

For very slender delta wings, such as the 75.3° swept wing on the Handley Page HP 115 (Ref. 27), the aerodynamic center shows a definite forward movement at higher angles of attack (see Fig. 13). Eq. (15) gives

$$\frac{d\bar{\xi}}{d\alpha} = -0.55\left(\bar{\xi}_a - \bar{\xi}_V\right)/\theta_{LE} \qquad (16)$$

For $\theta_{LE} = 15^\circ$, Eqs (7) and (10) give $\bar{\xi}_a = 0.62$ and $\bar{\xi}_V = 0.58$, i.e., $d\xi/d\alpha = -0.183$. This prediction is in very good agreement with the α trend for high angles of attack, where the effects of the fuselage have reached their saturation point (Fig. 13).

2.1.2 Sideslip Effects

At an angle of sideslip β (See Fig. 14 for definitions) the effective apex angle of the windward leading edge is increased by

$$\Delta\theta_{LE} = \tan^{-1}(\tan\beta/\cos\alpha)$$

The "false" half wing loading is increased by the factor

$$\left[\tan(\theta_{LE} + \Delta\theta_{LE})/\tan\theta_{LE}\right]^2$$

and the "true" half wing by the factor

$$\left[\tan(\theta_{LE} + \Delta\theta_{LE})/\tan\theta_{LE}\right]$$

Thus, Eq. (6) takes the following form for small sideslip angles (β).

$$\frac{1}{2}\left(\frac{dC_{Na}}{d\xi}\right)_{\perp} = \frac{\pi \sin 2\alpha \sin^2\theta_{LE}}{(b/2c_o)}\left(1 + \frac{\tan\beta}{\tan\theta_{LE}\cos\alpha}\right) x \begin{cases} \xi & : \xi \le 0.7\,\xi_a^* \\ 0.7 & : 0.7\,\xi_a^* < \xi < \xi_a^* \end{cases} \quad (18)$$

The corresponding "running" rolling moment loading is (See Fig. 14)

$$-\frac{1}{2}\frac{dC_{\ell a}}{d\xi} = \frac{1}{2}\left(\frac{dC_{Na}}{d\xi}\right)_{\perp}\frac{\bar{\eta}_a \sin\theta_{LE}\cos\theta_{LE}}{2\,(b/2c_o)} \quad (19)$$

Integration gives

$$-\frac{1}{2}C_{\ell a} = 0.7\,\pi\,\bar{\eta}_a\,\xi_a^{*2}\left(\frac{0.49\,\xi_a^*}{3} + \frac{0.51}{2}\right)\sin^3\theta_{LE} \cos\theta_{LE}(\cot\theta_{LE} - \tan\theta_{TE})^2 \sin\alpha\cos\alpha\left(1 + \frac{\tan\beta}{\tan\theta_{LE}\cos\alpha}\right) \quad (20)$$

Combining Eqs. (8) and (20) gives the following β-derivative at $\beta = 0$.

$$-(C_{\ell\beta})_a = \frac{\bar{\eta}_a\,\bar{\xi}_a\,C_{Na}}{1 - \Delta\xi_{aTE}}\,\frac{\cos\theta_{LE}(\cot\theta_{LE} - \tan\theta_{TE})}{2\cos\alpha} \quad (21)$$

In regard to the vortex-induced loads, the sideslip effects can be derived using the now well-established fact that the vortex lift is independent of aspect ratio* (Ref. 4 and 5). Thus, from Eq. (10) and definitions

$$C_{NV} = 1.37\,\pi\,(0.93\,\xi_V^* - 0.2)\,\sin^2\alpha$$

$$\frac{N_V}{(\rho_\infty U_\infty^2/2)} = C_{NV}\,\frac{bc_o}{2} = \frac{C_{NV}\,c_o^2}{\cot\theta_{LE} - \tan\theta_{TE}} \tag{22}$$

Lambourne (Ref. 28) has shown that the sideslip effect on vortex burst is well represented by including α in the effective sweep for the wing leading edge. Similarly, β can be included in the effective apex angle. θ_{LE} in Eq. (22) can be substituted by

$$\theta_{eff.} = \theta_{LE} + \tan^{-1}\,(\tan\beta/\cos\alpha)$$

and Eq. (22) gives

$$\frac{1}{2}\,\frac{N_V}{\left(\rho_\infty U_\infty^2/2\right)} = \frac{1}{2}\,\frac{1.37\pi\;c_o^2\left(0.93\xi_V^* - 0.2\right)\sin^2\alpha}{\left[\dfrac{1 - \tan\theta_{LE}\,(\tan\beta/\cos\alpha)}{\tan\theta_{LE} + \tan\beta/\cos\alpha} - \tan\theta_{TE}\right]} \tag{23}$$

The β-derivative of Eq. (23) for $\beta = 0$ is

$$\frac{1}{2}\,\frac{\partial}{\partial\beta}\left[\frac{N_V}{\rho_\infty U_\infty^2/2}\right]_{\beta=0} = \frac{1}{2}\,\frac{1.37\pi\;c_o^2\;(0.93\xi_V^* - 0.2)\;\sin^2\alpha}{\cos\alpha\,(1 - \tan\theta_{TE}\,\tan\theta_{LE})^2\,\cos^2\theta_{LE}} \tag{24}$$

*Which means physically that the vortex loads depend only on leading edge conditions and are insensitive to conditions at the inner wing surface (near the wing centerline).

When referred to the reference area $bc_o/2$ (of the real wing with θ_{LE} instead of θ_{eff} as its apex angle), Eq. (24) gives

$$\frac{1}{2}\left(\frac{dC_{NV}}{d\beta}\right)_{\beta=0} = \frac{C_{NV}}{2} \cot^2\theta_{LE}/\left(\cot\theta_{LE} - \tan\theta_{TE}\right) \cos^2\theta_{LE} \cos\alpha \quad (25)$$

Elle (Ref. 20) and others have shown that the spanwise location of the vortex is insensitive to aspect ratio as long as the wing is not very narrow or half model testing is not used (see Fig. 15). In the latter case the splitter plate boundary layer growth restricts the inwards vortex motion (e.g., the 76° swept wing in Fig. 15b). When α/θ_{LE} becomes very large (high sweep or high angle of attack) asymmetric vortex shedding starts occurring (Ref. 29).

Before this mutual vortex interference occurs, the vortex will move inboard on the windward (sideslipping) wing to a new position y_V, which is simply

$$y_V = \xi\, c_o \left(\bar{\eta}_V \tan\theta_{eff} - \tan\beta/\cos\alpha\right) \quad (26)$$

Thus, the lever arm in roll for the strip-load at moderate sideslip $\left(\beta < 10^\circ\right)$ is

$$\frac{y_V}{b} = \frac{\xi}{2\left(b/2c_o\right)}\left[\bar{\eta}_V \tan\theta_{LE} - \left(1 - \bar{\eta}_V\right)\beta/\cos\alpha\right] \quad (27)$$

As $\bar{\eta}_V$ usually is a constant independent of ξ (Refs. 7, 13, and 20), the rolling moment from one wing (half) is

$$-\frac{1}{2} C_{\ell V} = \frac{1}{2} C_{NV} \frac{\bar{y}_V}{b} \quad (28)$$

where $\bar{y}_V/b$ is given by Eq. (27) with $\xi = \bar{\xi}_V$. The β - derivative of Eq. (28) at $\beta = 0$ is

$$-\frac{1}{2}\left(\frac{dC_{\ell V}}{d\beta}\right)_{\beta=0} = \frac{1}{2}\left(\frac{dC_{NV}}{d\beta}\right)_{\beta=0} \quad \frac{\bar{\xi}_V \ \bar{\eta}_V \ \tan\theta_{LE}}{2\left(b/2c_o\right)}$$

$$-\frac{1}{2} C_{NV} \quad \frac{\bar{\xi}_V \ \left(1 - \bar{\eta}_V\right)}{2\left(b/2c_o\right)\cos\alpha} \tag{29}$$

$\left(C_{\ell_\beta}\right)_V$ for small β becomes, by use of Eqs. (25) through (29)

$$-\left(C_{\ell_\beta}\right)_V = \frac{C_{NV}}{\cos\alpha} \ \frac{\bar{\eta}_V \ \bar{\xi}_V}{2} \ \cot\theta_{LE} \left[1 + \tan^2\theta_{LE}\right.$$

$$\left. - \ \frac{1 - \bar{\eta}_V}{\bar{\eta}_V} \left(1 - \tan\theta_{TE} \ \tan\theta_{LE}\right)\right] \tag{30}$$

For extremely narrow wings, i.e., θ_{LE} is very small, the second term in the bracket is zero, and $-(C_{\ell\beta})_V$ is maximum. If $\eta_V \rightarrow 0.5$, the rolling derivative would become zero for a delta wing. This never really happens because asymmetric vortex shedding or other anomalies, such as vortex burst, occur long before this condition is reached.

In Fig. 16 the sideslip derivatives measured on 74° sharp-edged swept wings (Ref. 22) are compared with the predictions obtained from Eqs. (21) and (30) together with Eqs. (8) and (10). As before for the longitudinal characteristics (Figs. 9 and 10), the $M = 0$ predictions compare much better with the $M = 0.2$ test data than the $M = 1.0$ estimates do with the $M = 0.8$ experimental results. The reason is probably the same; i.e., at $M = 0.8$ there still are subsonic effects which are not accounted for in the $M = 1.0$ predictions, as is indicated by the consistently good prediction for $\theta_{TE} = 37°$, where the subsonic trailing edge effects are small. Again, the present approximation consistently provides a better prediction than the pure application of the leading-edge-suction analogy (Refs. 4 and 22).

The dependence of C_{ℓ_β} on $C_L = C_N \cos\alpha$ and θ_{LE}, together with the $C_L\ (\alpha/\theta_{LE})$-correlation shown earlier (Fig. 3), strongly suggests that it should be possible to develop a scaling law similar to Eq. (5) for C_{ℓ_β}. From Eqs. (21) and (30) the relationships for a delta wing ($\theta_{TE} = 0$) can be written as follows:

$$-\frac{\left(C_{\ell_\beta}\right)_a}{C_{N_a}/\tan\theta_{LE}} = \frac{\bar{\eta}_a\,\bar{\xi}_a}{1-\Delta\xi_{a_{TE}}}\cos\theta_{LE}/\cos\alpha$$

$$-\frac{\left(C_{\ell_\beta}\right)_V}{C_{NV}/\tan\theta_{LE}} = \frac{\bar{\eta}_V\,\bar{\xi}_V}{2\cos\alpha}\left[1-\frac{1-\bar{\eta}_V}{\bar{\eta}_V}\right] \qquad (31)$$

That is, one would expect that for slender wings (θ_{LE} small) at moderate angles of attack the following would hold:

$$-\frac{C_{\ell_\beta}}{C_L/\frac{A}{4}} = \text{CONSTANT} \qquad (32)$$

From earlier discussion (Eq. (5) and Fig. 3), one has

$$C_L/\left(\frac{A}{4}\right)^{3/2} = f(\alpha/\theta_{LE})$$

Thus, the sideslip derivative C_{ℓ_β} should scale as follows:

$$C_{\ell_\beta}/\left(\frac{A}{4}\right)^{1/2} = f\left(\alpha/\theta_{LE}\right) \qquad (33)$$

Figure 17 indicates that Eq. (33) is valid for the aspect-ratio-range $0.7 \le A \le 2.3$, and that present predictions agree well with experimental data (Refs. 22, 30, and 31). The "fall-off" at high α/θ_{LE} is caused by (cos α)-effects (see $C_L\ (\alpha/\theta_{LE})$-correlation, Eq. (4)). For $\theta_{LE} = 7.1^\circ$ the data point for $\alpha/\theta_{LE} = 1.5$ in Fig. 17 is "in line" as cos $\alpha \approx 1$, whereas the data point for $\theta_{LE} = 30^\circ$ falls off already at $\alpha/\theta_{LE} = 1.0$ because cos $\alpha = 0.866$.

This completes the discussion of static characteristics of sharp-edged delta wings. As long as subsonic leading edge conditions exist, i.e., the bow shock is detached, the above analysis is applicable. How the Mach number effects for $M > 1$ can be accounted for has been described by Polhamus (Ref. 5).

2.2 Unsteady Aerodynamic Characteristics

The nonlinear aerodynamic characteristics of slender delta wings will be analyzed using the method of local linearization, e.g., by considering small perturbations from a mean static angle of attack α_o (see Fig. 18). The total unsteady aerodynamic derivatives are then obtained by superposition of attached and separated flow components.

2.2.1 Attached Flow. The attached flow unsteady aerodynamics for $M \geq 1$ are obtained in the present analysis by a straightforward application of first-order momentum theory. It is assumed that the perturbation induces negligible changes in the axial velocity from the freestream value $U_\infty \cos \alpha_o$. The normal force per unit length of the vehicle is then the reaction to the substantial rate of change of momentum of the virtual mass per unit length (Refs. 32 and 33). With the coordinate system of Fig. 18 the normal force can be expressed as follows for a slender delta wing performing bending oscillations. In the "locally linearized case" in Fig. 18 the effective gust velocity component is $Wg \cos \alpha_o$.

$$\frac{dN}{dX} = -\frac{d}{dt}\left(\frac{dJ}{dX}\right) = -\left(U_\infty \cos \alpha_o \frac{\partial}{\partial X} + \frac{\partial}{\partial t}\right)\left(\frac{dJ}{dX}\right) \tag{34}$$

The momentum per unit length is

$$\frac{dJ}{dX} = \rho_\infty A(X) W = \rho_\infty A(X)\left(\frac{dZ}{dt} + W_g \cos \alpha_o\right)$$

$$= \rho_\infty A(X)\left[U_\infty \cos \alpha_o \frac{\partial Z}{\partial X} + \frac{\partial Z}{\partial t} + W_g \cos \alpha_o\right] \tag{35}$$

Thus

$$\frac{dN}{dX} = -\left(U_\infty \cos \alpha_o \frac{\partial}{\partial X} + \frac{\partial}{\partial t}\right)\left[\rho_\infty A(X)\right.$$
$$\left.\left(U_\infty \cos \alpha_o \frac{\partial Z}{\partial X} + \frac{\partial Z}{\partial t} + W_g \cos \alpha_o\right)\right] \tag{36}$$

With the gust stationary in space, $dWg/dt = 0$ and Eq. (36) can be written as follows: (Ref. 34)

$$\frac{dN}{dX} = -\left(U_\infty \cos \alpha_o + \frac{\partial}{\partial t}\right)\left[\rho_\infty A(X)\left(U_\infty \cos \alpha_o \frac{\partial Z}{\partial X} + \frac{\partial Z}{\partial t}\right)\right]$$
$$-\left\{\left(U_\infty \cos \alpha_o \frac{\partial}{\partial X} + \frac{\partial}{\partial t}\right)\left[\rho_\infty A(X)\right]\right\} W_g \cos \alpha_o \tag{37}$$

For a short time interval, during which ρ_∞ and U_∞ remain constant, Eq. (37) can be written in coefficient form as follows:

$$\frac{1}{\cos^2 \alpha_o}\frac{dC_N}{dX} = -\left(\frac{\partial}{\partial X} + \frac{1}{U_\infty \cos \alpha_o}\frac{\partial}{\partial t}\right)\left[\frac{2\,A(X)}{S}\left(\frac{\partial Z}{\partial X}\right.\right.$$
$$\left.\left. + \frac{1}{U_\infty \cos \alpha_o}\frac{\partial Z}{\partial t}\right)\right] - \left[\left(\frac{\partial}{\partial X} + \frac{1}{U_\infty \cos \alpha_o}\frac{\partial}{\partial t}\right)\frac{2\,A(X)}{S}\right]\frac{W_g}{U_\infty} \tag{38}$$

The equation of motion for single-degree-of-freedom bending oscillations can be written in the following form using standard notations:

$$\tilde{m}\left[\ddot{q}(t) + 2\,\zeta\,\omega\,\dot{q}(t) + \omega^2\,q(t)\right] = P(t) \tag{39}$$

where

$\tilde{m}$ = generalized mass

ζ = structural damping (as a fraction of critical damping)

ω = natural free-free bending frequency

q = normalized coordinate (dots denoting time derivatives in the usual way)

P(t) = generalized force.

The generalized force P(t) is given by the virtual work cone by the aerodynamic forces on the vehicle*

$$P(t) = \int \frac{dN}{dx} \phi(x)\, dx \tag{40}$$

There are three different types of generalized force

$$P(t) = P_a(t) + P_s(t) + P_b(t) \tag{41}$$

$P_a(t)$ = generalized force component due to attached flow

$P_s(t)$ = generalized force component due to separated flow

$P_b(t)$ = generalized force component independent of vehicle motion, e.g., due to buffeting or buzz.

The attached flow component, $P_a(t)$, is given by Eqs. (37) or (38) and (40). For single-degree-of-freedom bending oscillations, one has (see Fig. 18)

$$Z = -\phi(x)\, q(t) \text{ and } \partial/\partial X = -\partial/\partial x$$

*If W is the work done, $P = \partial W/\partial q$. As the vehicle is slender, axial force changes are assumed to be negligible compared with normal force changes.

Thus

$$P_a(t) \Big/ \left(\rho_\infty \; U_\infty{}^2 \Big/ 2\right) S \cos^2 \alpha_o = \frac{1}{\cos^2 \alpha_o} \int_{x_{TE}}^{x_A} \frac{dC_N}{dx} \phi(x) \, dx$$

$$= - \int_{x_{TE}}^{x_A} \frac{2A(x)}{S} \phi(x) \left[\phi'(x) \, q(t) - \phi(x) \, \frac{\dot{q}(t)}{U_\infty \cos \alpha_o} \right]$$

$$+ \int_{x_{TE}}^{x_A} \frac{2A(x)}{S} \left\{ \left[\phi'(x)\right]^2 q(t) - \left[\phi(x)\right]^2 \frac{\ddot{q}(t)}{U_\infty{}^2 \cos^2 \alpha_o} \right\} dx \qquad (42)$$

$$- \int_{x_{TE}}^{x_A} \frac{2A'(x)}{S} \phi(x) \, \frac{W_g \left(X_{CG} - x\right)}{U_\infty} \, dx$$

For a slender pointed wing (or body)

$$A(x_A) = 0 \, , \; A(x_{TE}) = \pi b^2 \Big/ 4 \, , \; A(x) = \pi \left| y(x) \right|^2$$

and Eq. (42) becomes

$$P_a(t) \Big/ \left(\rho_\infty \, U_\infty{}^2 \Big/ 2\right) S \cos^2 \alpha_o = \frac{\pi b^2}{2S} \left\{ \phi\left(x_{TE}\right) \, \phi'\left(x_{TE}\right) q(t) - \left[\phi\left(x_{TE}\right)\right]^2 \frac{\dot{q}(t)}{U_\infty \cos \alpha_o} \right\}$$

$$+ \frac{2\pi}{S} \int_{x_{TE}}^{x_A} \left[y(x) \right]^2 \left\{ \left[\phi'(x)\right]^2 g(t) - \left[\phi(x)\right]^2 \frac{\ddot{q}(t)}{U_\infty{}^2 \cos^2 \alpha_o} \right. \qquad (43)$$

$$\left. y(x) \; \phi(x) \; \frac{W_g \left(X_{CG} - x\right)}{U_\infty} dx \right. - \frac{4\pi}{S} \int_{x_{TE}}^{x_A}$$

Eq. (43) can conveniently be expressed as follows, with time measured from time of gust entry (Refs. 34 and 35)

$$P_a(t) = \left(\rho_\infty U_\infty{}^2 / 2\right) S \left\{ K_a\, q(t) + D_a \frac{\dot{q}(t)}{U_\infty} + I_a \frac{c\,\ddot{q}(t)}{U_\infty{}^2} + G_a(t) \right\}$$

$$K_a = \frac{\pi}{2S} \cos^2 \alpha_o \left\{ b^2\, \phi\left(x_{TE}\right)\, \phi'\left(x_{TE}\right) + 4 \int_{x_{TE}}^{x_A} \left[y(x)\right]^2 \left[\phi'(x)\right]^2 \, dx \right\}$$

$$D_a = -\frac{\pi b^2}{2S} \cos \alpha_o \left[\phi\left(x_{TE}\right)\right]^2 \qquad (44)$$

$$I_a = -\frac{2\pi}{c_o S} \int_{x_{TE}}^{x_A} \left[y(x)\right]^2 \left[\phi(x)\right]^2 \, dx$$

$$G_a(t) = -\frac{4\pi}{S} \cos^2 \alpha_o \int_{x_{TE}}^{x_A} y(x)\, \phi(x)\, \frac{W_g\left(U_\infty\, t - \left|x_A - x\right|\right)}{U_\infty} \, dx$$

K_a, D_a, and I_a are coefficients determining the aerodynamic spring, damping, and inertia, respectively. $G_a(t)$ represents the gust penetration load in coefficient form.

For the special case of rigid body oscillations around x_{CG}, the deflection $\delta(x, t)$ in Fig. 18 takes the following form:

$$\delta(x,t) = \phi(x)\, q(t) = \left(\frac{x - x_{CG}}{c_o}\right) \left[c_o\, \theta(t)\right]$$

or with $x = x_A - c_o \xi$, where $x_A - x_{TE} = c_o$

$$\phi(x) = -\left(\xi - \xi_{CG}\right)$$

$$\phi'(x) = 1/c_o \qquad (45)$$

$$q(t) = c_o \theta(t)$$

Eq. (44) can then be written as follows for rigid body oscillations in uniform flow ($W_g = 0$):

$$P_a(t) = \left(\rho_\infty U_\infty^2/2\right) S \left[k_a \theta(t) + d_a \frac{c_o \dot{\theta}(t)}{U_\infty} + i_a \frac{c_o^2 \ddot{\theta}(t)}{U_\infty^2}\right.$$

$$k_a = -\frac{\pi b^2}{2S} \cos^2 \alpha_o \left[1 - \xi_{CG} + \int_1^0 \left[\frac{y(\xi)}{b/2}\right]^2 d\xi\right]$$

$$d_a = -\frac{\pi b^2}{2S} \cos \alpha_o \left(1 - \xi_{CG}\right)^2 \qquad (46)$$

$$i_a = \frac{\pi b^2}{2S} \int_1^0 \left[\frac{y(\xi)}{b/2}\right]^2 \left(\xi - \xi_{CG}\right)^2 d\xi$$

With c_o as the reference length, the coefficients k_a, d_a, and i_a in Eq. (46) are simply C_{m_θ}, $C_{m_{\dot{\theta}}}$, and $C_{m_{\ddot{\theta}}}$. With $\bar{c}$ as the reference length, one obtains*

*One may have to go back to Eq. (46) in some cases, e.g., if different reference lengths are used for the reduced frequency and the pitching moment, as $\bar{c}$ varies according to individual taste. For delta wings, both $\bar{c} = 2c_o/3$ and $\bar{c} = c_o/2$ are used (Refs. 22 and 36, respectively).

$$C_{m_{\theta_a}} = -\frac{c_o}{\bar{c}} C_{N_{\alpha_o}} \cos^2 \alpha_o \left(\bar{\xi}_a - \xi_{CG}\right)$$

$$C_{m_{\dot{\theta}_a}} = -\left(\frac{c_o}{\bar{c}}\right)^2 C_{N_{\alpha_o}} \cos \alpha_o \left(1 - \xi_{CG}\right)^2$$

$$C_{m_{\ddot{\theta}_a}} = -\left(\frac{c_o}{\bar{c}}\right)^3 C_{N_{\alpha_o}} \int_1^o \left[\frac{y(\xi)}{b/2}\right]^2 \left(\xi - \xi_{CG}\right)^2 d\xi \qquad (47)$$

$$C_{N_{\alpha_o}} = 2\pi \, (b/2)^2 \Big/ S = \pi A/2$$

$$\bar{\xi}_a = 1 + \int_1^o \left[\frac{y(\xi)}{b/2}\right]^2 d\xi \quad \left(= \frac{2}{3} \text{ for delta wings}\right)$$

$C_{N_{\alpha_o}}$ is the standard slender body derivative, and $C_{m_{\ddot{\theta}}}$ is usually negligible.

When $M < 1$, the subsonic A_{TE}-effect shown in Fig. 2 is approximated by an equivalent wing with straight trailing edge and the above attached flow formulas are applied to this "equivalent" shortened wing. The effective span of this equivalent subsonic wing is determined by equating the normal force determined by Eq. (2) for the original wing and by slender body theory for the equivalent wing. Eqs. (7) and (47) give the following relationships for a delta wing:

$$C_{N_{\theta_a}} = \frac{d\, C_{N_a}}{d\theta} = 1.82\pi \cos 2\alpha_o \sin^2 \theta_{LE} \Big/ \left(b/2\, c_o\right)$$

$$C_{N_{\theta_a}} = C_{N_{\alpha_o}} \cos^2 \alpha_o = 2\pi \cos^2 \alpha_o \left(\frac{b_{eff}}{2}\right)^2 \Big/ \left(b\, c_o/2\right) \qquad (48)$$

That is

$$\frac{b_{eff}}{b} = \frac{c_{eff}}{c_o} = 0.955 \cos \theta_{LE} \left[2 - \cos^{-2} \alpha_o\right]^{1/2} \tag{49}$$

and Eq. (47) takes the following form for a delta wing at $M = 0$ (with $C_{m_{\ddot{\theta}_a}} \approx 0$).

$$C_{m_{\theta_a}} = -\frac{c_o}{\bar{c}} \left(C_{N_\alpha}\right)_{eff.} \cos^2 \alpha_o \left[\frac{2}{3} \frac{c_{eff}}{c_o} - \xi_{CG}\right]$$

$$C_{m_{\dot{\theta}_a}} = -\left(\frac{c_o}{\bar{c}}\right)^2 \left(C_{N_\alpha}\right)_{eff.} \cos \alpha_o \left[\frac{c_{eff.}}{c_o} - \xi_{CG}\right]^2 \tag{50}$$

$$\left(C_{N_\alpha}\right)_{eff} = \frac{\pi A}{2} \left(\frac{b_{eff}}{b}\right)^2$$

Fig. 19 shows that Eq. (50) predicts the measured dynamic derivatives (Refs. 36 through 38) at $\alpha = 0$, $M = 0$, with satisfactory accuracy. At higher aspect ratios, $A > 2$, the deviations probably become unacceptable and a more sophisticated theory has to be used (see Ref. 39).

2.2.2 Separated Flow. The transient leading edge separation characteristics on sharp-edged delta wings have been investigated extensively by the British. Most noteworthy are the contributions made by Lambourne and his colleagues (Refs. 40 through 42) using a combined experimental-analytical approach. The results obtained in a water tunnel for a plunging delta wing established a very simple picture of the unsteady leading edge separation and the formation of the leading edge vortex (see Fig. 20). The steady-state vortex position is established after a time increment $\Delta t = c_0 \xi/U_\infty$. That is the vortex is convected downstream from apex with free-stream speed. In the time interval before the steady-state position is reached, the transient vortex is parallel to the leading edge, as the local shedding takes place at the same rate along the leading edge. It is, of course, not surprising to find that the unsteady vortex position, like the steady (Ref. 20 and Fig. 15), is dependent only upon α/θ_{LE} (see Fig. 21). The vortex apparently reaches its steady state height position somewhat before $t = c_0 \xi/U_\infty$, when the steady-state spanwise position is reached. This faster vertical movement is best illustrated by the vortex paths in the crossflow-plane (Fig. 22).

A stepwise increase of α from a nonzero value presents a picture consistent with the convection downstream of the new vortex system (Fig. 23). When the angle of attack is decreased, the pattern becomes somewhat more complicated (Fig. 24). Initially, there is an appreciable delay before the vortex height is changed, but there is no such delay in the inboard vortex movement (Fig. 24a). The flow visualization results show that attachment at the leading edge does not occur instantly when α is reduced, but the separation persists for some time, probably because of the induced velocity associated with the continuing downstream presence of the "old vortex system," as is suggested by the authors (Ref. 41). Owing to the continuous weakening (diffusion) of the vortex, it cannot be traced for late times, e.g., for $\Delta t/(c_0/U_\infty) > 0.6$. When the angle of attack is decreased to a nonzero value, the initial behavior is qualitatively the same as for a decreas to $\alpha = 0$, but there seems to be little spanwise movement of the vortex (Fig. 24b). An initial outboard movement is followed by an inboard movement back to the initial position. That is, it is mainly the vortex height that is changed.

The transient lift distributions shown in Fig. 25 are suggested by the authors, based upon their flow visualization results. The effect of secondary separation is omitted for sake of clarity. When the angle of attack is increased, the vortex loading increases initially with its aerodynamic center near the leading edge before the inboard vortex movement catches up and the steady state distribution is approached (see Fig. 25a). The flow visualization results clearly indicate that when the angle of attack is decreased the same transient flow changes do not simply occur in the reverse direction (compare Figs. 25a and 25b). That is, the pressure change (due to vortex-induced loads) at any given position on the upper wing is not necessarily reversible with respect to increasing and decreasing incidence. This irreversibility may play a part in the observed differences in the effects of positive and negative sharp-edged gusts (Ref. 43). Another noteworthy difference between increasing and decreasing angles of attack is the difference in aerodynamic center. During the transient condition after an α -increase, the aerodynamic center (AC) will be ahead of its static position. By contrast, the transitory AC for an α -decrease is aft of its steady-state position.

This difference between "downstroke" and "upstroke" vortex position has been observed on a delta wing oscillating in heave (Ref. 19 and Fig. 26). Only close to the apex is there a symmetric displacement from the steady-state position. Farther aft, the vortex never gets down to the steady-state position. This amplitude modulation is the likely result of "flow memory," consistent with the irreversibility between increasing and decreasing α -effects observed by Lambourne et al. (Ref. 41 and Fig. 25). When plotted directly against the reduced frequency, based upon distance from apex, without consideration to vortex location on the wing, the phase lag does not seem to agree with the findings by Lambourne et al. (see Fig. 27a). The low and high reduced frequency data (actually high and low freestream speed data*) fall on both sides of Randall's theory (Ref. 44). However, when plotted against reduced frequency, the various chordwise positions seem to have a cyclic lag variation which approaches the Lambourne-value at low reduced frequencies. The saturation of phase lag for high frequencies is very similar to that observed for the two-dimensional Karman-Sears vortex wake effect (see Refs. 45 through 48, and Fig. 28). Thus, one would expect the "Lambourne-lag," or constant-timelag concept, to be valid only for low reduced frequencies.

In their most recent investigation of unsteady leading edge vortices Lambourne et al. studied the effect of oscillatory bending deformation of the forward half of a sharp-edged delta wing by measuring the pressure fluctuations over the rigid aft half (Ref. 42 and Fig. 29). Distributed roughness was used over the forward 14 percent chord to ensure turbulent flow over the whole upper inner surface. In the thorough "calibration" of the test setup it was discovered that the pressure transducer housing, protruding slightly from the bottom surface, could cause a severe disturbance of the leeside vortex flow if placed near the leading edge (see Fig. 30). The result is similar to that obtained on delta wings by placement of miniscule flow fences or, rather, vortex generators on the underside of the leading edge, when the large continuous leading edge vortex is broken down into smaller ones. If one examines the oil flow pattern in Fig. 30b closely, one finds evidence of a new reattachment line close to the leading edge, starting at ξ_1, thus indicating that a new vortex has started at station ξ_1, at the same time as the "old one" starts "bending-off" towards the freestream direction. The practical consequence for Lambourne et al. was that they had to remove the outer transducer at station ξ_1, when making measurements at ξ_2. The practical consequence for the space shuttle designer could be much more far reaching.

The steady-state spanwise pressure distributions at maximum upward and downward deflections are compared with the undeflected wing data in Fig. 31. As expected the windward side pressures are unaffected by the wing deformation. On the leeward side the inboard pressure change caused by the deformation is explained by regular attached flow camber effects and is roughly predicted by lifting surface theory. The outboard vortex-induced loads are affected by the deformation in a manner that is somewhat more intricate. The spanwise position of the suction peak is affected by the wing deformation in a manner consistent with the higher "average" α / θ_{LE} for the forward delta wing in the case of upward deflection, causing an inboard movement of the vortex (and conversely an outboard movement for the downward deflection).

*For a sharp leading edge the associated differences in Reynolds number would only affect the secondary separation and have little influence on the position of theprimary vortex.

Less obvious are the reasons for the changes of the suction peak magnitude in Fig. 3la. Lambourne et al. suggests that the vortex movement up and away from the surface dominates over the effect of increased vortex strength for the bent-up wing, causing a loss in aft wing suction peak magntiude. An alternative or possibly complementary explanation is provided by the present analysis, i.e., the shedding sheet from the leading edge weakens earlier for the upward deflection. The reason is that α/θ_{LE} decreases along the chord, thus decelerating the vortex shedding process, whereas the opposite is true for the downward deflection. Thus, the breakdown of the vortex growth rate is reacting to longitudinal camber in the same was as Lambourne et al. have shown vortex burst to be affected (Ref. 49 and Fig. 32). A similar α/θ_{LE}-effect is obtained by changing θ_{LE} along the chord. Thus, a Gothic wing corresponds to the positive camber (bent down apex) and one can expect similar vortex-growth trends. This is confirmed by experimental data that is discussed in detail later in conjunction with unsteady lateral characteristics.

For the low Reynolds number (Fig. 3lb), the vortex does not start at the apex for the bent down case. The angle of attack at apex is then only 0.5°, and the vortex starts downstream of 10% chord according to visual observations, whereas at the higher Reynolds number it is believed to start upstream of 10% chord. Fig. 31 shows that second separation has significant effects on the pressure distribution also for a turbulent center-wing boundary layer.* The effects are, however, much less than in the case of laminar flow (compare Fig. 31 with Figs. 4 and 5).

*It is, of course, also possible that the apex roughness was not entirely successful in establishing turbulent flow over the entire upper surface.

Referring to Figs. 18 and 29, the bending deformation can be written

$$-\delta(x, t) = \phi(x)\, q(t)$$
$$q(t) = \Delta z \cos \omega t \qquad (51)$$

The quasi-steady deflection is obtained with $\Phi = \omega t$, where the phase angle Φ varies from 0 to 2π. Fig. 33 shows the effect of this quasi-steady deflection on the spanwise lift distribution. Apparently, the vortex load is not only moving in spanwise direction but is also undergoing some spanwise redistribution (or deformation). The first harmonic would be very important for a structural deformation such as wing bending (more or less parallel to the leading edge). Even the higher harmonics have some potential in this respect. This force-couple-type of harmonic can indeed make the higher wing deformation modes (with nodal lines parallel, almost, with the leading edge) critical from the standpoint of wing buffet (Refs. 50 and 51), as is also pointed out by Lambourne et al. (Ref. 42). In comparing Figs. 31 and 33, one notes that the spanwise pressure distribution for the basic harmonic (n = 0) has the same mean peak value as the static pressure distribution, but the width of the peak is greater than the static suction peak. This growth in width is, of course, related to the spanwise movement of the suction peak with apex deflection (Fig. 31).

In the oscillatory case the distributions are very similar to those shown in Fig. 33 for the quasi-steady deformation. The spanwise variation of phase lag is displayed by plotting amplitude and associated phase angle, as is done in Fig. 34. The data points for the first three harmonic components cluster about straight lines passing through the origin, indicating that the pressure variations across the span are in phase with one another. This tendency is strongest for the first harmonic. The slope of the line through the origin is a measure of the mean value of the phase angle. The phase angles seem to increase proportionately to the order of the harmonic. That is,

$$\Delta\Phi = K_1 n, \quad \text{where } K_1 = \text{constant.}$$

By comparing Figs. 34a and 34b, one finds, in addition, that the phase angle is proportional to ξ, which has also been observed on a delta wing describing plunging

oscillations (Ref. 52) and is, of course, in agreement with expectations based on the earlier work by Lambourne et al. (Refs. 40 and 41). That is, the phase lag is determined by a constant timelag Δt.

$$\Delta\phi = n\,\omega\Delta t$$
$$\Delta t = K_2\, c_o \quad \xi/U_\infty \tag{52}$$

The results in Fig. 35 give $K_2 = 1.00 \pm 0.01$, in excellent agreement with the earlier sudden-plunge results (Refs. 40 and 41). That the time lag would be the same for a plunging and a bending wing, i.e., independent of the chordwise (α/θ_{LE}) -distribution, was demonstrated by Lambourne et al. in the following elegant manner (Ref. 42). The strength $\Gamma(\xi)$ of the vortex at any position ξ can be regarded as the integral result of the vorticity shed from all positions upstream of ξ. For conical flow $d\Gamma/dx$ is constant,* and for small perturbations can be assumed to vary linearly with the change of local angle of attack. That is

$$\Delta\left(\frac{d\Gamma}{d\xi}\right) = k_1 \Delta\alpha \tag{53}$$

The perturbation of the vortex strength at any station downstream of the deforming part. That is,

$$\tilde{\Gamma}(\xi) = \Gamma(\xi, \tilde{\alpha}) - \Gamma(\xi, \alpha_o) = \int_D \frac{d\Gamma}{d\xi}\, d\xi = k_1 \int_D \tilde{\theta}(\xi) d\xi \tag{54}$$

In the case of static deformation $\tilde{\theta}(\xi) = \frac{\partial z}{\partial \xi}$ and Eq. (51) gives

$$\Gamma(\xi) = -k_1 z_o \tag{55}$$

*According to the discussion earlier in connection with Figs. 4 through 6 this is strictly valid only for the region close to apex, $\xi \leq 0.4$.

That is, the vortex-strength-perturbation is proportional to the deflection at the apex independent of the shape of the deformation. In the unsteady case the local, effective perturbation angle is

$$\tilde{\theta}(\xi) = \partial \mathfrak{z}/\partial \xi + c_o/U_\infty \, \partial \mathfrak{z}/\partial t \tag{56}$$

The vortex strength at a point convecting with the flow is determined by $\tilde{\theta}(\xi)$.

$$\frac{d\tilde{\Gamma}(\xi)}{d\xi} = k_1 \tilde{\theta}(\xi) \tag{57}$$

At station ξ_1, at time t_1, the vortex strength would be the sum of the vorticity shed from each position ξ upstream of ξ_1 at the earlier time $t_1 - c_o(\xi_1 - \xi)/U_\infty$. For a certain deflection $\mathfrak{z}(0, t - c_o \xi_1/U_\infty)$ equal to the deflection $\mathfrak{z}(0) = \mathfrak{z}_o$ in the static case, the equivalent deformation shape in the unsteady case will deviate from the static deformation shape (see Fig. 35a). However, because the final vortex strength $\tilde{\Gamma}(\xi)$ is independent of the deformation shape, i.e., it is insensitive to the manner $(d\Gamma/d\xi)$ in which the vorticity was added upstream of ξ_1 to reach the final value, the vortex strength at ξ_1 in the unsteady case is simply

$$\tilde{\Gamma}(\xi_1, t_1) = -k_1 \mathfrak{z}(0, t_1 - c_o \xi_1/U_\infty) \tag{58}$$

or with $\mathfrak{z} = \mathfrak{z}_o \cos \omega t$

$$\tilde{\Gamma}(\xi, t) = -k_1 \mathfrak{z}_o \cos(\omega t_1 - \bar{\omega} \xi_1) \tag{59}$$

Thus, the vortex strength locally at ξ_1 and ξ_2 are dependent upon the apex deflection in the manner observed for the fluctuating pressures in the experiment. Lambourne et al. conclude that although the pressure variations are very dependent upon the height- and span-wise movements of the vortex, these movements are probably themselves dependent upon the changes in vortex strength, and Eq. (59) would apply also for the

pressure variations. Thus, the pressure variations are in the unsteady case simply determined by phase lagging the quasi-steady pressure variations. That is, the pressure amplitude is not modulated by the frequency.

This constant-time-lag, constant-amplitude solution is exactly what the present authors have used as the low frequency approximation of the Karman-Sears vortex-wake effects in two-dimensional airfoil flow (Refs. 47 and 48).

In regard to the cautionary remarks by Lambourne et al. that their derivation considers only convection of disturbances that are upstream of the observation point, (and neglects pressure changes due to disturbances downstream of the observation point), the following observation can be made. The local vortex strength will determine the local pressures as long as the reduced frequency is low because then the "neighborhood" vortex-strength-deviations from this local value, upstream and downstream from the observation point, are negligibly small. That is, the derived results for the pressure variation are valid only for low frequencies. When the frequency is high, this "lumped-timelag" approximation is no longer good. For instance, in the case of the plunging data discussed earlier (Ref. 19 and Fig. 27) $\bar{\omega} = 3.4$ means that half the wavelength of the vortex perturbation is equal to the chordwise extent (c_o) of the delta wing. In this case the "neighborhood-deviation" of the vortex strength is no longer negligible, and the constant timelag approximation is not applicable. In the case of Karman-Sears two-dimensional vortex-wake effects a constant-phase-lag/frequency-modulated-amplitude approximation could be found for high reduced frequencies (Refs. 47 and 48). The plunging data discussed earlier (Ref. 19 and Fig. 27) indicate that a similar phase-lag-saturation effect exists for the unsteady leading edge vortex shedding. One can also expect that the amplitude will be affected by the frequency, as is discussed later.

The sketches in Fig. 35 illustrate why plunging and bending oscillations have the same timelag. A series of quasi-steady rigid wings make up the forward vortex-shedding body in the case of plunging oscillations, but the equivalent deformation concept still holds, as long as the vortex follows the local wing flow, which is already implied in the conic-flow-assumption. For the same reason, the effect of the forward wing deformation on downstream vortex-induced pressures will be the same

regardless of whether or not the aft wing is rigid or is also describing some sort of unsteady deformation.* That is, the present authors believe the results obtained by Lambourne et al. to have a wider application than they have assumed. Mathematically the vortex-induced load component has the same form as the force induced by a flow separation spike (the spike tip corresponding to the apex, Refs. 33 through 35). For a slender delta wing the generalized force $P_s(t)$ in separated flow can be written as follows for one-degree-of-freedom bending oscillations (modifying Eq. 5 of Ref. 35; see Fig. 18 for definitions).

$$P_s(t)/\left(\rho_\infty \; U_\infty^2/2\right) S = \int_{x_{TE}}^{x_A} d/dx \left(d\Delta^i C_{Ns}/dz\right) \phi(x) \left[\phi(x_A)\, q(t - \Delta t) - \phi(x)\, q(t)\right] dx \tag{60}$$

$$+ \int_{x_{TE}}^{x_A} d/dx \left(d\Delta^i C_{Ns}/dz\right) (x_A - x)\, \phi(x) \left[W_g(X - x)/U_\infty\right] dx$$

It is assumed that the gust-induced flow inclination is small enough to satisfy the small perturbation assumption. The derivative $d\Delta^i C_{Ns}/dz$ is obtained from static characteristics, observing that for a rigid wing

$$-\left|z(x_A) - z(x)\right| = (x_A - x) \tan\alpha \approx (x_A - x)\,\alpha$$

That is,

$$\frac{d}{dx}\left(\frac{d\Delta^i C_{Ns}}{dz}\right) = -\frac{d}{dx}\left(\frac{d\Delta^i C_{Ns}}{d\alpha}\right) \Big/ (x_A - x) \tag{61}$$

*The $\xi \leq 0.4$ restriction for the conic flow assumption imposes the same error in both cases.

For low reduced frequencies, $\bar{\omega} < 1$, which are of practical interest for the transonic and supersonic speed regimes of the space shuttle ascent, $q(t - \Delta t)$ can be approximated by a Taylor-expansion

$$q(t - \Delta t) = q(t) - \Delta t\, q(t) + 1/2\, (\Delta t)^2\, \ddot{q}(t) \ldots \tag{62}$$

With time $t = 0$ at time of gust entry (Refs. 34 and 35), Eqs. (60) through (64) give

$$P_s(t) = (\rho_\infty U_\infty^2/2)\, S \left[K_s\, q(t) + D_s\, \dot{q}(t)/U_\infty + I_s\, c_o\, \ddot{q}(t)/U_\infty^2 + G_s(t) \right]$$

$$K_s = -\int_{x_{TE}}^{x_A} \left[d(\Delta^i C_{N_{\alpha_s}})/dx \right] \left[\phi(x_A) - \phi(x) \right] / (x_A - x)\ \phi(x)\, dx$$

$$D_s = -(U_\infty/\bar{U}) \int_{x_{TE}}^{x_A} \left[d(\Delta^i C_{N_{\alpha_s}})/dx \right] \phi(x_A)\ \phi(x)\, dx \tag{63}$$

$$I_s = -(1/2)(U_\infty/\bar{U})^2 \int_{x_{TE}}^{x_A} \left[d(\Delta^i C_{N_{\alpha_s}})/dx \right] \phi(x_A)\ \phi(x)\ (x_A - x)/c_o\, dx$$

$$G_s(t) = -\int_{x_{TE}}^{x_A} \left[d(\Delta^i C_{N_{\alpha_s}}/dx) \right] \phi(x)\ (x_A - x) \left\{ W_g \left(U_\infty t - \left[U_\infty/\bar{U} \right] \left[x_A - x \right] \right) / U_\infty \right\} dx$$

Combining Eqs. (45) and (63) gives the following separation-induced generalized force on a rigid wing, describing oscillations in pitch around its center of gravity (in uniform flow, $W_g = 0$).

$$
\left.
\begin{aligned}
P_s(t) &= \left(\rho_\infty U_\infty^2/2\right)\ S\ c_o \left[k_s\ \theta(t) + d_s \frac{c_o\ \dot{\theta}(t)}{U_\infty} + i_s \frac{c_o^2\ \ddot{\theta}(t)}{U_\infty^2}\right] \\
k_s &= -\int_0^1 \frac{d\left(\Delta^i C_{N\alpha_s}\right)}{d\xi}\left(\xi - \xi_{CG}\right) d\xi \\
d_s &= \xi_{CG}\ \frac{U_\infty}{\bar{U}} \int_0^1 \frac{d\left(\Delta^i C_{N_{\alpha_s}}\right)}{d\xi}\left(\xi - \xi_{CG}\right) d\xi \\
i_s &= \frac{\xi_{CG}}{2}\left(\frac{U_\infty}{\bar{U}}\right)^2 \int_0^1 \frac{d\left(\Delta^i C_{N_{\alpha_s}}\right)}{d\xi}\left(\xi - \xi_{CG}\right)\ \xi\, d\xi
\end{aligned}
\right\} \quad (64)
$$

With c_o as the reference length, the coefficients k_s, d_s, and i_s in Eq. (64) are simply the contributions from the leading edge separation to the stability derivatives C_{m_θ}, $C_{m_{\dot{\theta}}}$, and $C_{m_{\ddot{\theta}}}$, respectively. With $\bar{c}$ $(\neq c_o)$ as the reference length (for both moment and reduced frequency), the C_m- derivatives are

$$
\left.
\begin{aligned}
C_{m_{\theta_s}} &= -\frac{c_o}{\bar{c}}\ \Delta^i C_{N_{\alpha_s}}\left(\bar{\xi}_s - \xi_{CG}\right) \\
C_{m_{\dot{\theta}_s}} &= \left(\frac{c_o}{\bar{c}}\right)^2\ \xi_{CG}\ \frac{U_\infty}{\bar{U}}\ \Delta^i C_{N_{\alpha_s}}\left(\bar{\xi}_s - \xi_{CG}\right) \\
C_{m_{\ddot{\theta}_s}} &= -\left(\frac{c_o}{\bar{c}}\right)^3\ \frac{\xi_{CG}}{2}\left(\frac{U_\infty}{\bar{U}}\right)^2 \int_0^1 \frac{d\left(\Delta^i C_{N_{\alpha_s}}\right)}{d\xi}\left(\xi - \xi_{CG}\right)\xi\, d\xi
\end{aligned}
\right\} \quad (65)
$$

Notice that the separation-induced timelagged component has opposite effects on static and dynamic stability, similar to that observed for separated flow effects on launch vehicles (Refs. 33 through 35). $\Delta^i C_{N_{\alpha_S}} = d C_{NV}/d\alpha$ and $\bar{\xi}_S = \bar{\xi}_V$ are obtained from Eq. (10) for M = 0 and from Eq. (11) for M≥1. Eq. (65) then gives (neglecting $C_{m_{\ddot{\theta}_S}}$)

$$C_{m_{\dot{\theta}_S}} = - \frac{c_o}{\bar{c}} \xi_{CG} \frac{U_\infty}{\bar{U}} C_{m_{\theta_S}} \tag{66}$$

Where $C_{m_{\dot{\theta}_S}} = C_{m_{\alpha_V}}$ from Eq. (10), and $U_\infty/\bar{U} = 1$ (Ref. 42)

2.2.3 Comparison with Experimental Data

The predictions obtained by use of Eqs. (50) and (66) are compared with experimental data (Refs. 36 and 37) in Fig. 36. Obviously, all the vortex-induced loads are not dependent only upon flow conditions at the apex, as is assumed in Eq. (66). The character of the deviations suggests that a substantial part of the vortex-induced load has mathematically attached flow character. It has been shown by Rainbird (Refs. 53 through 55) that free body vortices on a sharp cone not only generate suction peaks underneath them (Fig. 37a), but the vortices also entrain freestream air, causing higher surface flow shear on the leeward side than is measured at $\alpha = 0$ (Fig. 37b). Thus, instead of decreasing the "body steering effects", as for instance flare-induced separation does on a launch vehicle (Refs. 33 through 35), the leading edge separation increases the effective apparent mass. Assuming that a fraction ϵ of the vortex-induced loading is caused by this increase of the attached flow-type loading, Eq. (66) is modified as follows:

$$C_{m_{\theta_s}} = C_{m_{\theta_{s_1}}} + C_{m_{\theta_{s_2}}}$$

$$C_{m_{\dot{\theta}_s}} = C_{m_{\dot{\theta}_{s_1}}} + C_{m_{\dot{\theta}_{s_2}}}$$

$$C_{m_{\theta_{s_1}}} = -\frac{c_o}{\bar{c}} \epsilon \, C_{N_{\alpha_V}} \left(\bar{\xi}_a - \xi_{CG}\right)$$

$$C_{m_{\theta_{s_2}}} = -\frac{c_o}{\bar{c}} (1 - \epsilon) \, C_{N_{\alpha_V}} \left(\bar{\xi}_V - \xi_{CG}\right) \tag{67}$$

$$C_{m_{\dot{\theta}_{s_1}}} = -\left(\frac{c_o}{\bar{c}}\right)^2 \epsilon \, C_{N_{\alpha_V}} \sec \alpha_o \left[\frac{c_{eff}}{c_o} - \xi_{CG}\right]^2$$

$$C_{m_{\dot{\theta}_{s_2}}} = -\left(\frac{c_o}{\bar{c}}\right) \xi_{CG} \frac{U_\infty}{\bar{U}} C_{m_{\theta_{s_2}}}$$

where ξ_a for M = 0 is obtained from Eq. (7), c_{eff}/c_o from Eq. (49), $C_{N_{\alpha_V}}$ and $\bar{\xi}_V$ from Eq. (10).

Fig. 38 shows that if half the vortex-induced lift is caused by increased leeside "body-steering" effects, Eq. (67), together with Eq. (50), can indeed predict the measured dynamic derivatives. However, such a large change of "body steering" effects seems unreasonable.

In the plunging test performed by Lambourne et al. (Ref. 41), it was observed that the leading edge vortex reached its steady-state height position before it reached the steady-state spanwise position (see Fig. 21). Thus, it is suggested by the vortex-height data that a value of $U_\infty/\bar{U} = 0.75$ should be used when computing the pitch damping. In the case of the vortex-induced rolling moment, $U_\infty/\bar{U} = 1.00$ is, of course, the representative value. The fact that the pressure oscillations for the deforming wing (Ref. 42) gave $U_\infty/\bar{U} = 1.00$ does not contradict the above conclusion. As the

pressure measurements gave meaningful phase lag results only in the region of the vortex-induced suction peak (over the center region of the wing the harmonic response amplitudes were insignificant), where the pressure changes registered by a fixed pressure transducer will be very sensitive to the spanwise vortex movement,* the pressure data should give $U_\infty/\bar{U} = 1.00$. Finally, the fact that $\bar{U} > U_\infty$ is completely in accord with measured velocities in the vortex core (Ref. 56). Fig. 39 shows that theoretical predictions based upon the more realistic assumption $\epsilon = 0.30$, $U_\infty/\bar{U} = 0.75$ agree at least as well with experimental data as the earlier prediction based upon $\epsilon = 0.50$, $U_\infty/\bar{U} = 1.00$ (compare Figs. 38 and 39).** These values for ϵ and $\bar{U}/U_\infty$, determined by semi-empirical means from rigid body dynamic data, can be used in an elastic vehicle analysis to determine the aero-elastic stability of the space shuttle lift-off configuration including the effects of delta wing leading edge separation.

Experimental results for the sharp-edged $A = 1.484$ delta wing (Ref. 57) seem to indicate that the constant-timelag, constant-amplitude assumption used to obtain the theoretical predictions shown in Figs. 38 and 39 would have limited application (see Fig. 40). One can see how nonlinear amplitude effects will couple with frequency effects when both perturbation amplitude and frequencies are high, but the small amplitude, $\Delta\theta = 1^\circ$, used to obtain the data shown in Fig. 40 should preclude any such frequency effects. A rough assessment can be made in the following manner.

The local perturbation magnitude is

$$|\tilde{\alpha} - \alpha_o| = |\tilde{\theta}| = \left| \theta + (\xi - \xi_{CG}) \frac{c_o \dot{\theta}}{U_\infty} \right|.$$

That is,

$$|\tilde{\theta}| = \Delta\theta \left[1 + \bar{\omega}^2 \left(\xi - \xi_{CG} \right)^2 \right]^{1/2}$$

$$\approx \Delta\theta \left[1 + \frac{1}{2} \bar{\omega}^2 \left(\xi - \xi_{CG} \right)^2 \cdots \right] \qquad (68)$$

*As has been pointed out by Hummel (Ref. 51).

**The corresponding reduction of the destabilizing C_{L_V}-trend in Figs. 10 and 11 will improve rather than worsen the agreement with experimental results.

It was discussed earlier how the deforming wing results (Ref. 42 and Fig. 31) could be explained by the effect of longitudinal camber on the vortex growth rate. One can get an estimate of the pitch-rate-induced camber-effect by integrating Eq. (68) to obtain

$$\left|\mathcal{Z}(\xi)\right| = \int_0^{\xi} \left|\bar{\theta}\right| \, d\xi \approx \Delta\theta \left[\xi + \frac{\bar{\omega}^2}{6}\right]\left(\xi^3 - 3\xi^2 \xi_{CG} - 3\xi\xi_{CG}\right)$$

$$\left|\mathcal{Z}_o\right| = \left|\mathcal{Z}(0)\right| = \Delta\theta \, \xi_{CG}\left[1 + \frac{\bar{\omega}^2 \, \xi_{CG}^2}{6}\right] \tag{69}$$

If one assumes that the differences in actual deflection shape has an insignificant effect, which is consistent with Lambourne's results discussed earlier, one can use the experimental data in Fig. 31 to define the pitch-rate-induced camber-effect on the vortex induced loads.

$$\frac{\Delta C_{N_V}}{C_{N_V}} = \frac{\Delta\left(-C_p\right)_{max}}{\left(-C_p\right)_{max}} = \frac{1}{\left(-C_p\right)_{max}} \frac{\partial\left(-C_p\right)_{max}}{\partial \mathcal{Z}_o} \left|\mathcal{Z}_o\right| \tag{70}$$

where $\mathcal{Z}_o$ is given by Eq. (69).

The frequency effect on the vortex-induced contributions to the stability derivatives is

$$k_{\bar{\omega}} = \frac{1}{C_{m_{\theta_s}}} \frac{\partial C_{m_{\theta_s}}}{\partial \bar{\omega}} = \frac{1}{C_{m_{\dot{\theta}_s}}} \frac{\partial C_{m_{\dot{\theta}_s}}}{\partial \bar{\omega}} = \frac{1}{C_{N_{\alpha_V}}} \frac{\partial C_{N_{\alpha_V}}}{\partial \bar{\omega}} \tag{71}$$

Combining Eqs. (69) through (71) gives

$$k_{\bar{\omega}} = \frac{1}{\left(-C_p\right)_{max}} \frac{\partial\left(-C_p\right)_{max}}{\partial \gamma_o} \xi_{CG}^2 \frac{\Lambda\theta\,\bar{\omega}}{3} \tag{72}$$

Fig. 31 gives

$$\frac{1}{\left(-C_p\right)_{max}} \frac{\partial\left(-C_p\right)_{max}}{\partial \gamma_o} = 6.4$$

and $k_{\bar{\omega}}$ becomes

$$k_{\bar{\omega}} = 0.037 \left(\Lambda\theta^o\right) \xi_{CG}^2 \bar{\omega}$$

For $(\Lambda\theta^o) = 1$ and $\bar{\omega} \leq 0.5$, $k_{\bar{\omega}} \leq 0.019\, \xi_{CG}^2$. That is, $k_{\bar{\omega}} < 1\%$ for $\xi_{CG} < 75\%$. Thus, the effect is completely negligible and cannot explain the results in Fig. 40.

If one compares Fig. 40 with the corresponding results for an A = 0.654 delta wing (Ref. 36), one finds that the frequency effects are very inconsistent (see Fig. 41). If one also notices that the frequency effect over the range $0 \leq \bar{\omega} \leq 0.5$ is no larger than the Reynolds number effect at any one frequency, one starts to suspect that the frequency effect is tied to some other flow phenomenon, not to the leading edge separation. Reynolds number cannot affect the leading edge separation on sharp-edged delta wings. It will, however, affect the secondary separation. If one assumes that the frequency-effects in Fig. 40 are tied to the secondary flow separation, the results make more sense.* It was observed at the tests (Ref. 37) that there was a "kink" in the secondary separation line on the A = 1.484 delta wing. As the secondary flow separation can have appreciable effects on the vortex-induced loads (see Figs. 4 and 5, for example), it would seem reasonable to assume that the large effects of Reynolds number and frequency on the stability data in Fig. 40 are both connected to the secondary flow separation.** That is, the results in Fig. 40 have no bearing on the validity of Eqs. (66) and (67),

*This is also consistent with the observed large effects of spanwise tripwires on the frequency dependence (Ref. 37).

**The opposite effect of increasing frequency on static and dynamic stability is completely in agreement with the usual effects of convective timelag and accelerated flow on "regular" separation (Refs. 33 and 58).

as these equations only concern the effects of the (primary) leading edge separation. For the high Reynolds numbers and roughened surfaces of interest in regard to the space shuttle flight characteristics, the secondary separation is very unlikely to cause any such anomalous results as those displayed in Fig. 40.

The vortex-burst-effects measured in Ref. 57 are of more practical interest (see Fig. 42). At a first glance, the data in Fig. 42 seem to indicate that vortex burst will not cause any of the devastating effects that the present authors have postulated (Refs. 25 and 59). However, the data are difficult to interpret and make sense only after a rather thorough study. Hummel (Refs. 30, 31, and 60) has shown that the vortex burst is the three-dimensional equivalent to two-dimensional airfoil stall, causing a loss of lift and a statically destablizing pitching moment (see Fig. 43). The C_L-loss is rather gradual, but the moment changes in a discontinuous fashion. If one were to take C_{m_α}-slopes over a 2° interval at every 5° mean angle (α_0), corresponding to the 1° amplitude C_{m_θ}-data in Fig. 42, one could easily miss the main effect of vortex burst, i.e., the discontinous change of aerodynamic characteristics. The situation is very similar to that for "sudden-separation" effects on blunt cylinder-flare bodies at transonic speeds (see Refs. 61 through 64 and Fig. 44). The 1° amplitude oscillations do not reveal any dramatic effects of the sudden separation (Fig. 44b) in spite of the large moment discontinuity (fig. 44a). The reason is very simple. The 1° amplitude oscillations never "caught" the C_m-discontinuity. Even when trying to oscillate across the discontinuity, the large "kick" in the aerodynamic spring often prevents (regular) oscillations to be performed unless the amplitude is comparatively large (several degrees in case of the C_m (α)-data shown in Fig. 44a). When one performs large amplitude oscillations, e.g., around $\alpha_0 = 0$ (Fig. 44c), the stability data look reassuring until the amplitude is large enough to catch the C_m-discontinuity. Then a large increase of aerodynamic stiffness, and an even larger decrease of aerodynamic damping result. In the case shown in Fig. 44c, pitch oscillations will damp down to $\Delta\theta = 0$ for $\theta_{initial} < \alpha_d$, but for $\Delta\theta > \alpha_d$ the oscillations will diverge (or converge for large $\Delta\theta_{initial}$) to a limit-cycle- amplitude of 10° or more. Fig. 44 illustrates that one has to be very cautious when using experimental methods that are intended primarily

for linear, or at least continuous, aerodynamic characteristics to investigate highly nonlinear aerodynamic phenomena. Comparing Figs. 43 and 44, one can see that vortex burst will not cause the loss of damping experienced by the reentry body at large amplitudes. Instead, the result will be a loss of aerodynamic stiffness which can cause violent pitch-up (Ref. 65). The effect on lateral characteristics can be even more disconerting as is discussed later.

Returning to Fig. 42, one finds that the burst-induced reduction of the statically stabilizing $C_m(\alpha)$-slope (see Fig. 43) seems to be registered only by the experimental data for $\xi_{CG} = 0.5$ (not for $\xi_{CG} = 0.75$), with the $C_{m_{\dot{\theta}}}$-data showing the corresponding (expected) damping increase. The reason for the lack of similar changes for $\xi_{CG} = 0.75$ is probably that the vortex burst does not move up from the downstream "wake" to the delta wing surface in a smooth, continuous manner. Instead, the vortex burst more or less jumps past the 75% chord (see Refs. 66 and 67, and Fig. 45). Thus vortex burst jumps all the way forward past CG for $\xi_{CG} = 0.75$ and causes therefore statically stabilizing and dynamically undamping effects, opposite to what was observed for $\xi_{CG} = 0.50$.

Tobak et al. (Ref. 68) have investigated the effects of free body vortices on the aerodynamics of slender bodies in coning motion. It was expected that the vortex-pair would be skewed from the symmetry plane owing to the motion-induced side wash, but it was somewhat of a surprise to find this "tilt-angle" to remain constant along the body length. (Later measurements showed this to be true also for stations downstream of the rotation-center, where the local induced sidewash changes sign.) It was found that the "tilt-angle" was simply the effective side wash angle at apex, induced by the coning motion. From static measurements in pitch, the vortex-induced contribution to the pitching moment was obtained by subtracting the theoretical predictions for attached flow. Taking the projected side moment component of this pitching moment due to the tilting of the vortex pair gave a fairly good estimate of the measured side moment. Similar results have been found for pointed cones (Ref. 69) although a good part of the observed side moment characteristics can in that case be generated by nonlinear inviscid flow effects (Ref. 70). These results make more sense now when viewed against the delta wing results obtained by Lambourne et al. (Refs. 40 through 42).

2.2.4 Lateral Stability Characteristics. When presenting the data shown in Fig. 46, Bisgood (Ref. 71) suggested that the difference between the two sets of flight results could mean that the effect on $C_{\ell_{\dot{\beta}}}$ of the rate of change of sideslip ($\dot{\beta}$) was not negligible, as one usually assumes. It will be shown here that vortex-induced effects give Bisgood good reasons for this speculation. Peckham in his extensive experiments (Ref. 7) investigated the effects of Gothic (and ogee) planform-variations from the basic sharp-edged delta wing. Fig. 47 shows how the vortex-induced lift causes an aft AC-movement on a Gothic wing in sharp contrast to the forward AC-movement observed on the delta wing. This implies, of course, that the center of pressure of the vortex-induced lift is aft of the attached flow loading for the Gothic wing. Following our earlier reasoning in regard to how the vortex-growth rate depends on $\alpha/\theta_{LE} = f(\xi)$, one can anticipate that the Gothic wing will have its vortex-induced loads growing much farther downstream than the delta wing. This would result in a more aft AC of the vortex lift and also in a larger $\bar{\eta}_V$; i.e., the vortex with its suction peak will be closer to the leading edge, as has been shown by Werlé, for instance (see Ref. 79 and Fig. 48).

Applying these static planform-results to the sideslipping wing, assuming, as Lambourne has been doing for the delta wing (Ref. 42) and we have for elastic launch vehicles (Ref. 73), that the unsteady loading is made up of the static load-components from one or more of a series of suitably deformed configurations,* the results sketched in Fig. 49 are obtained. It is obvious that the vortex-induced lift will cause a "right-wing-down" C_ℓ contribution acting against the "right-wing-up" stabilizing roll-derivative ($-C_{\ell_\beta}$) (see Fig. 14 for definitions).

On a rolling wing at nonzero angle of attack, $\alpha_0 > 0$, or high roll rate, or both, a similar favorable increasing(α/θ_{LE})-trend along the length of the leading edge is generated, as the roll-rate-induced contribution to α_N (and α) is proportional to ξ. Thus, one can expect the vortex-induced loads to continue growing downstream of $\xi = 0.4$, resulting in increasing vortex induced loads toward the trailing edge, as had been measured by Harvey (see Ref. 74 and Fig. 50). The spanwise pressure distributions in Fig. 50 are noticeable also in another respect. There are no signs

*This equivalence for quasi-steady deformation does not always hold. See Ref. 46, for example. It should hold here, however, for sharp-edged delta wings.

of a secondary separation. The centrifugal "thinning" effect on the boundary layer may be one reason; but the tightly connected vortex close to the surface, due to the $\left(\alpha/\theta_{LE}\right)$- variation, is probably also a contributing factor.

When angle of attack is increased from $\alpha = 0$ to values where a vortex exists already for zero roll rate, the roll damping is initially increasing linearly with α_o, as the vortex strength is proportional to α_o (See Ref. 75 and Fig. 51.) However, as α_o is increased above a critical value ($\alpha_o = 6^\circ$ in Fig. 51), the feeding sheet starts "loosening up" and vortex suction is lost over the aft wing, resulting in decreased roll-rate effects (decreased roll damping). When $\alpha_o > 12^\circ$, the roll damping goes below the $\alpha_o = 0$ value. Similar trends are exhibited by the results in Ref. 76 (see Fig. 52). The deviation from the tighter wrapping vortex-sheet predictions for the conic flow assumption (Ref. 4) are very similar to those seen earlier for the $C_m(C_L)$ - characteristics (see Fig. 10).

That vortex burst may be of concern for lateral characteristics is shown in Fig. 53 for the BAC 221 Aircraft.

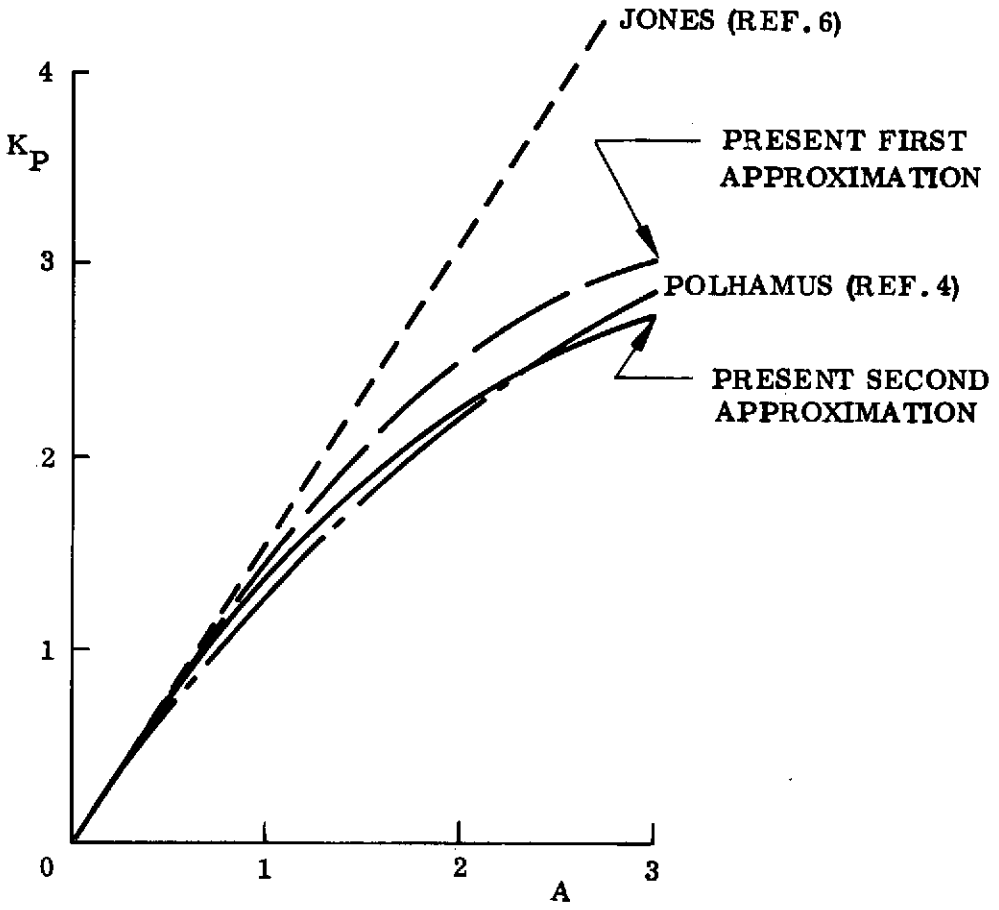

Figure 1. Attached Flow Lift Factor K_p of Delta Wings at M = 0

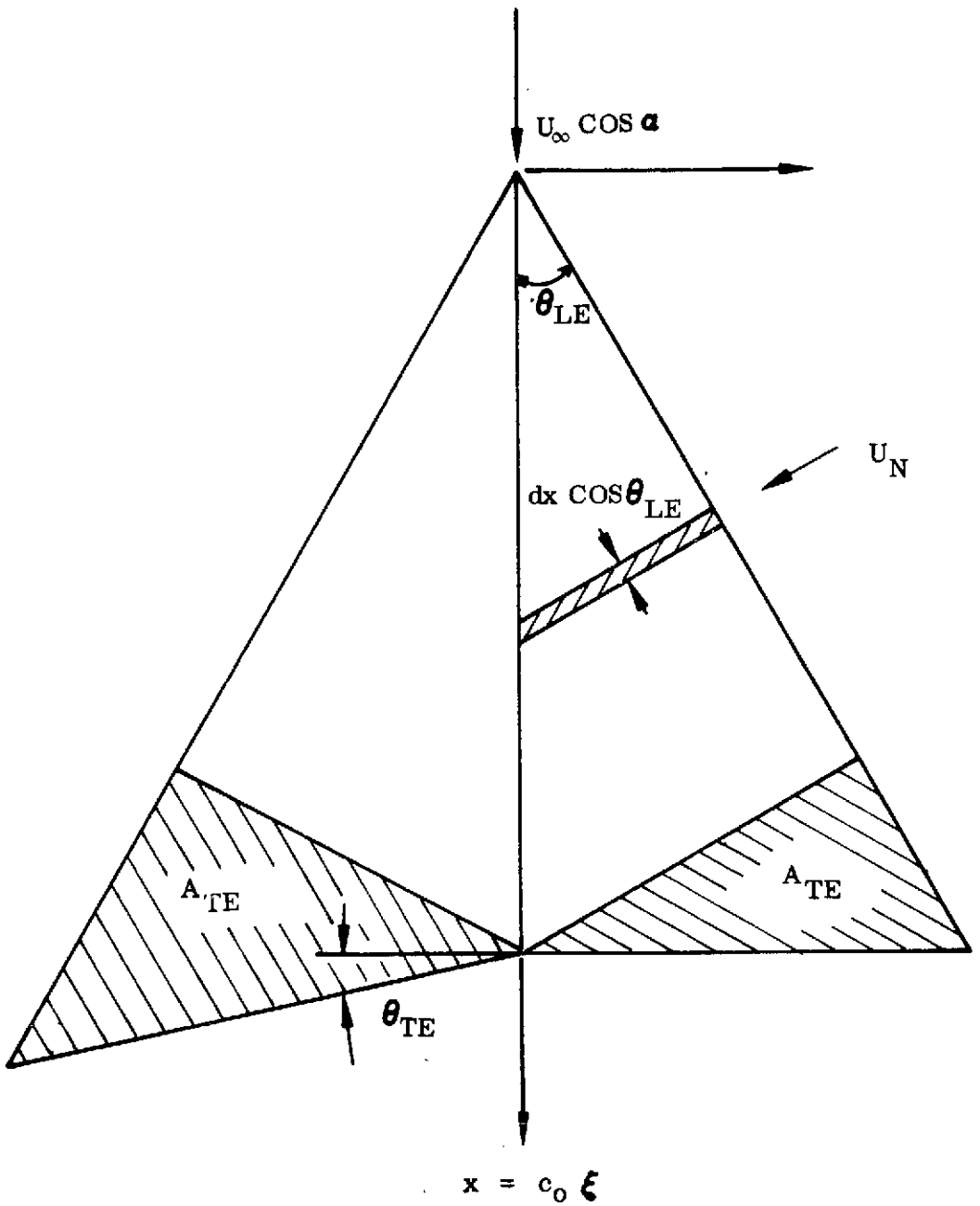

Figure 2. Definition of Slender Wing Geometry for Strip Load Computation

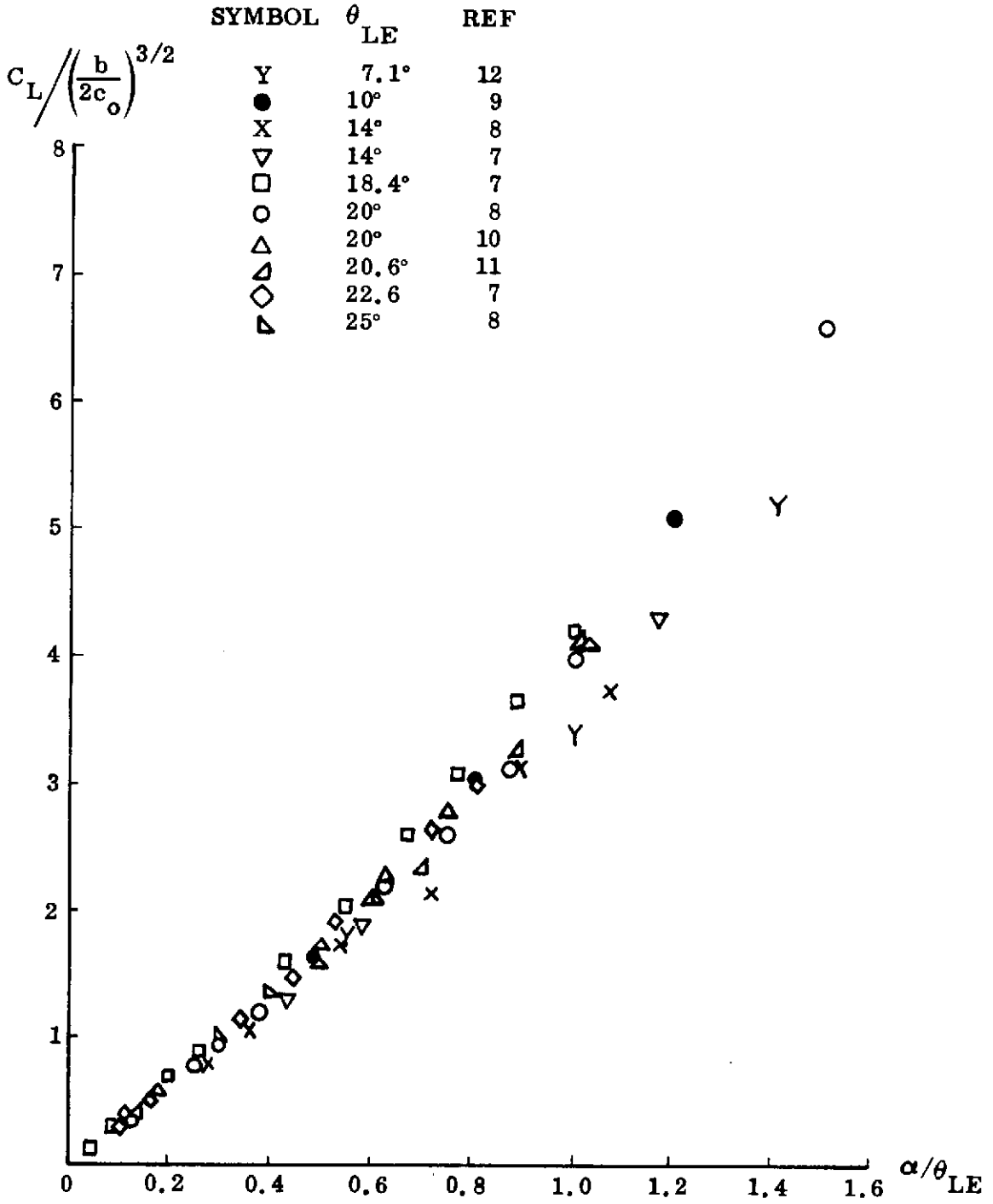

Figure 3. Universal Scaling of Delta Wing Lift

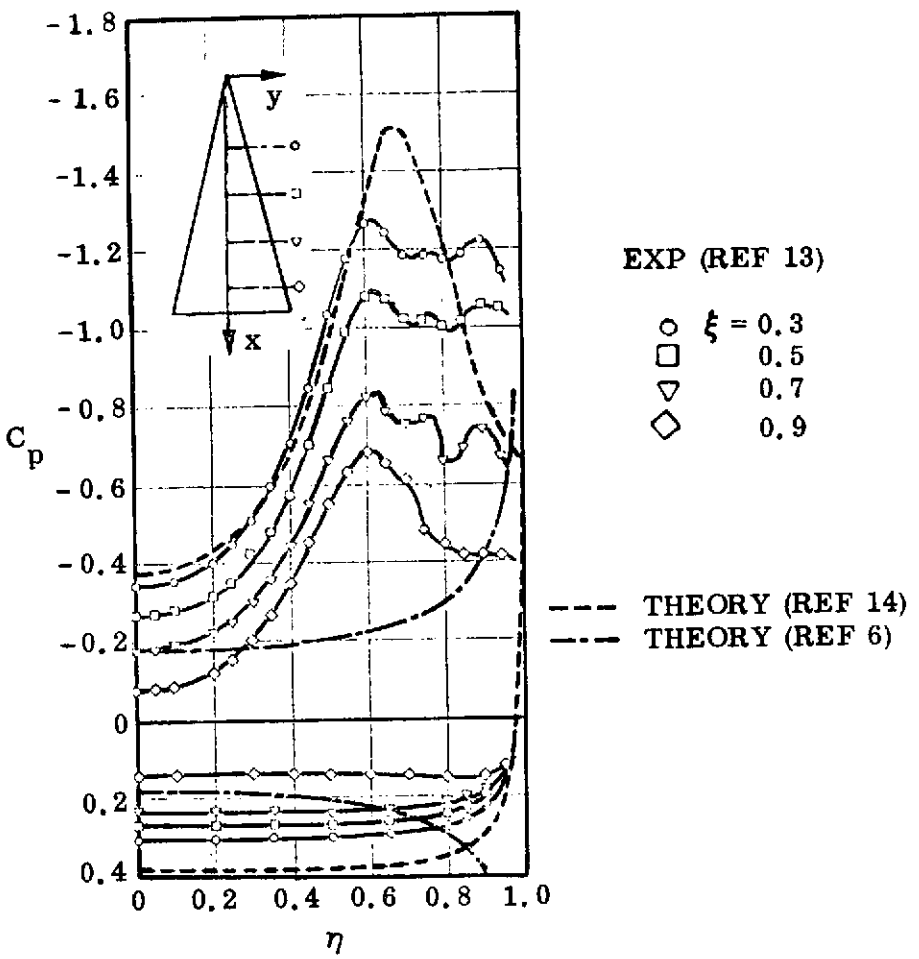

Figure 4. Pressure Distribution on an A=1 Sharp-Edged Delta Wing at $\alpha = 20.5^\circ$ and M = 0

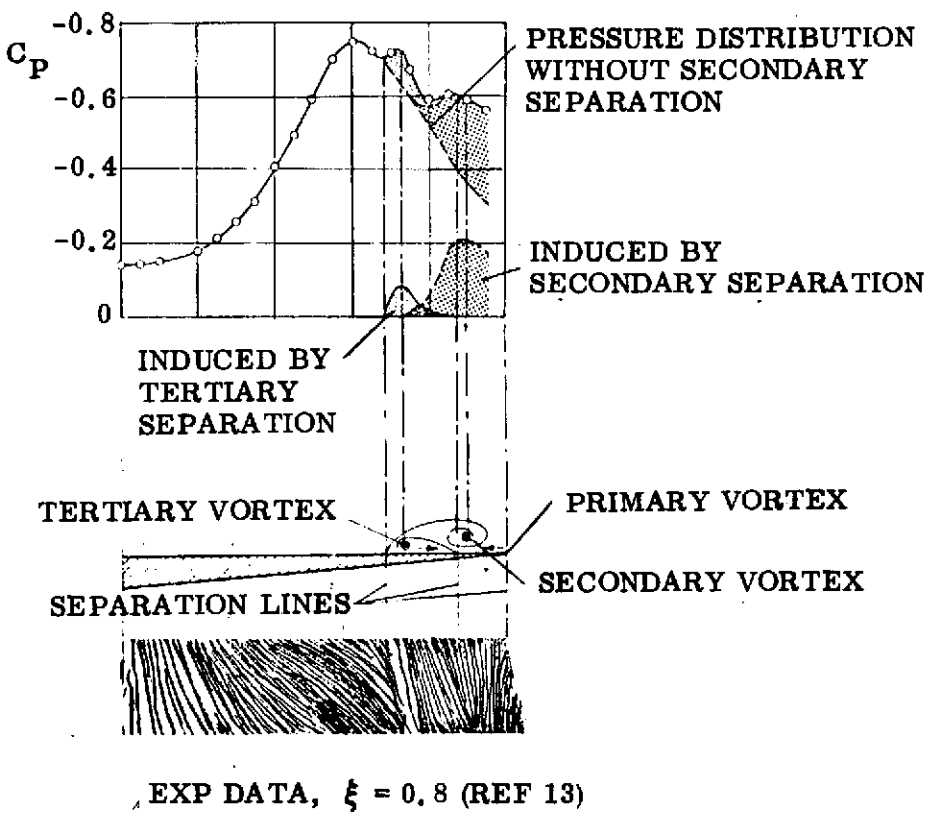

Figure 5. Effect of Secondary and Tertiary Flow Separation on Spanwise Pressure Distribution on an A = 1 Delta Wing at $\alpha = 20.5^\circ$ and M = 0

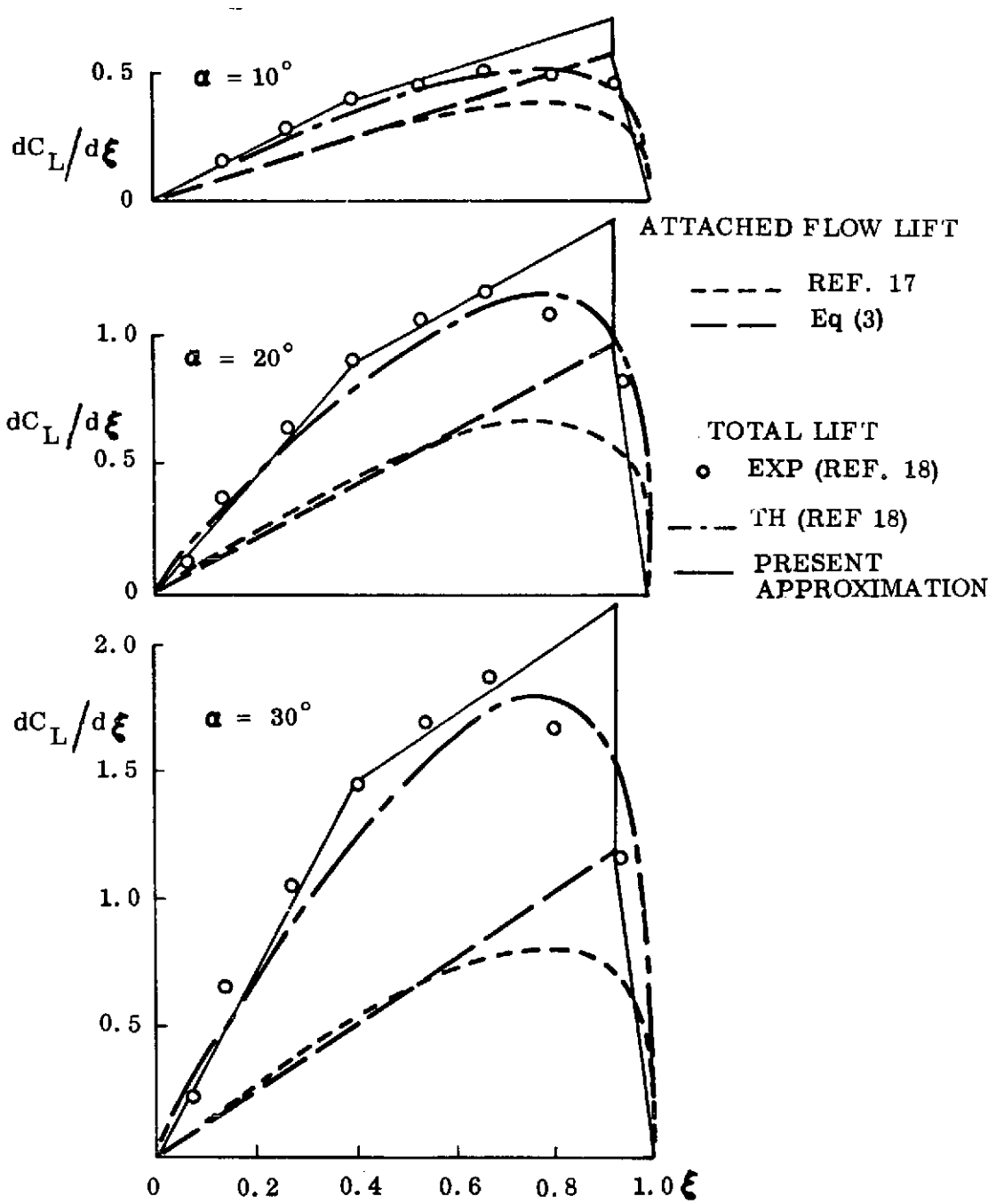

Figure 6. Lift Distribution Components on an A = 1.147 Delta Wing

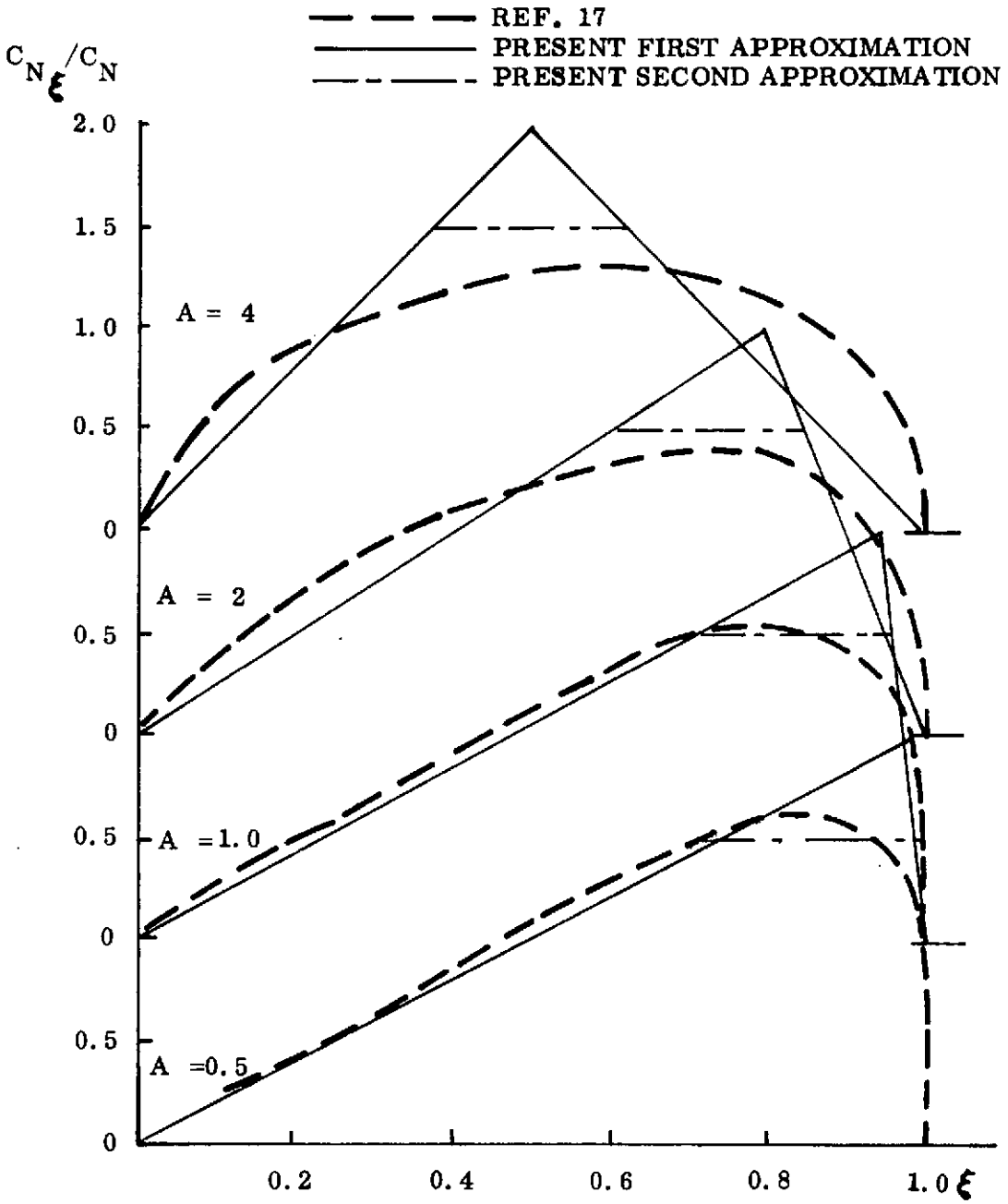

Figure 7. Attached Flow Load Distribution

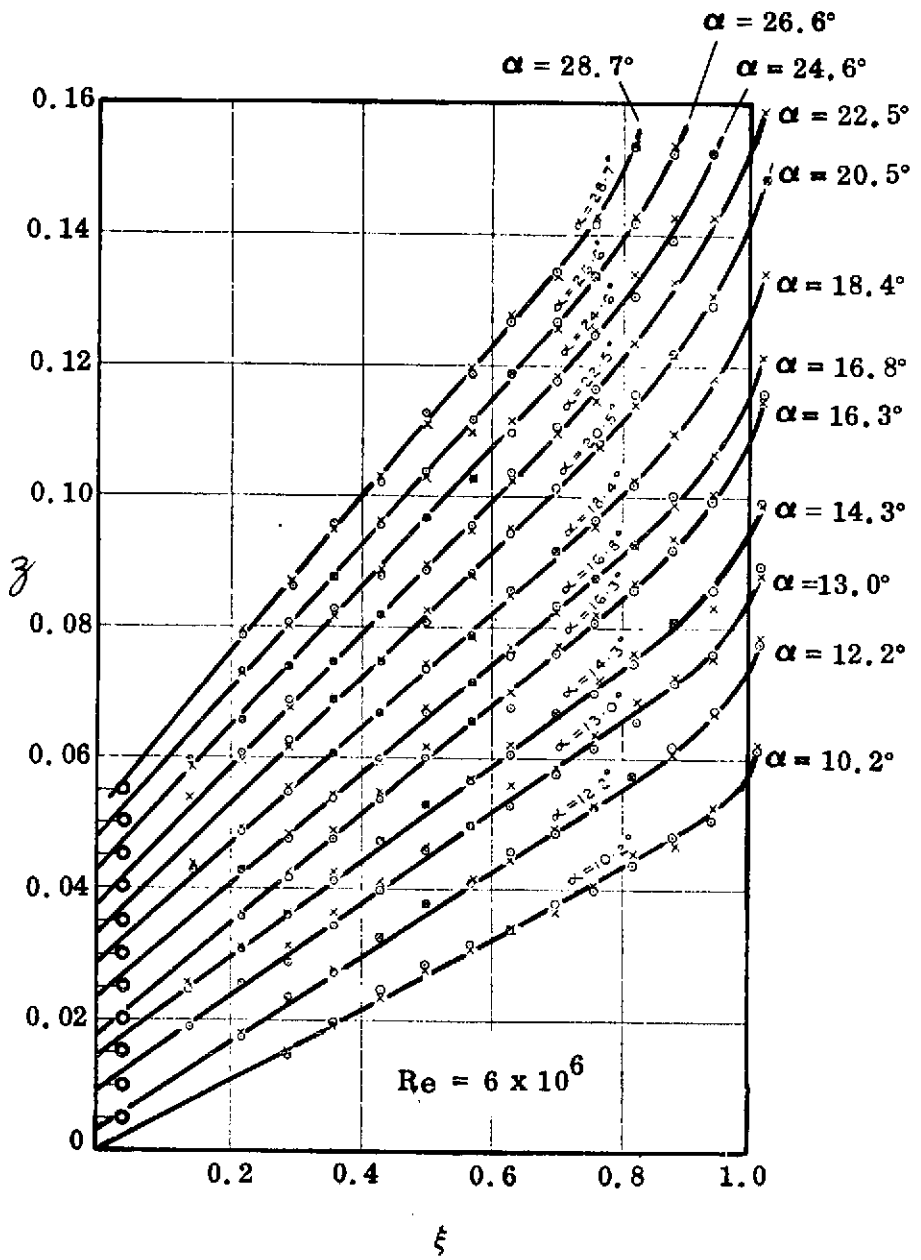

Figure 8. Leading Edge Vortex Trajectories on an A = 1 Sharp-Edged Delta Wing (Ref. 19)

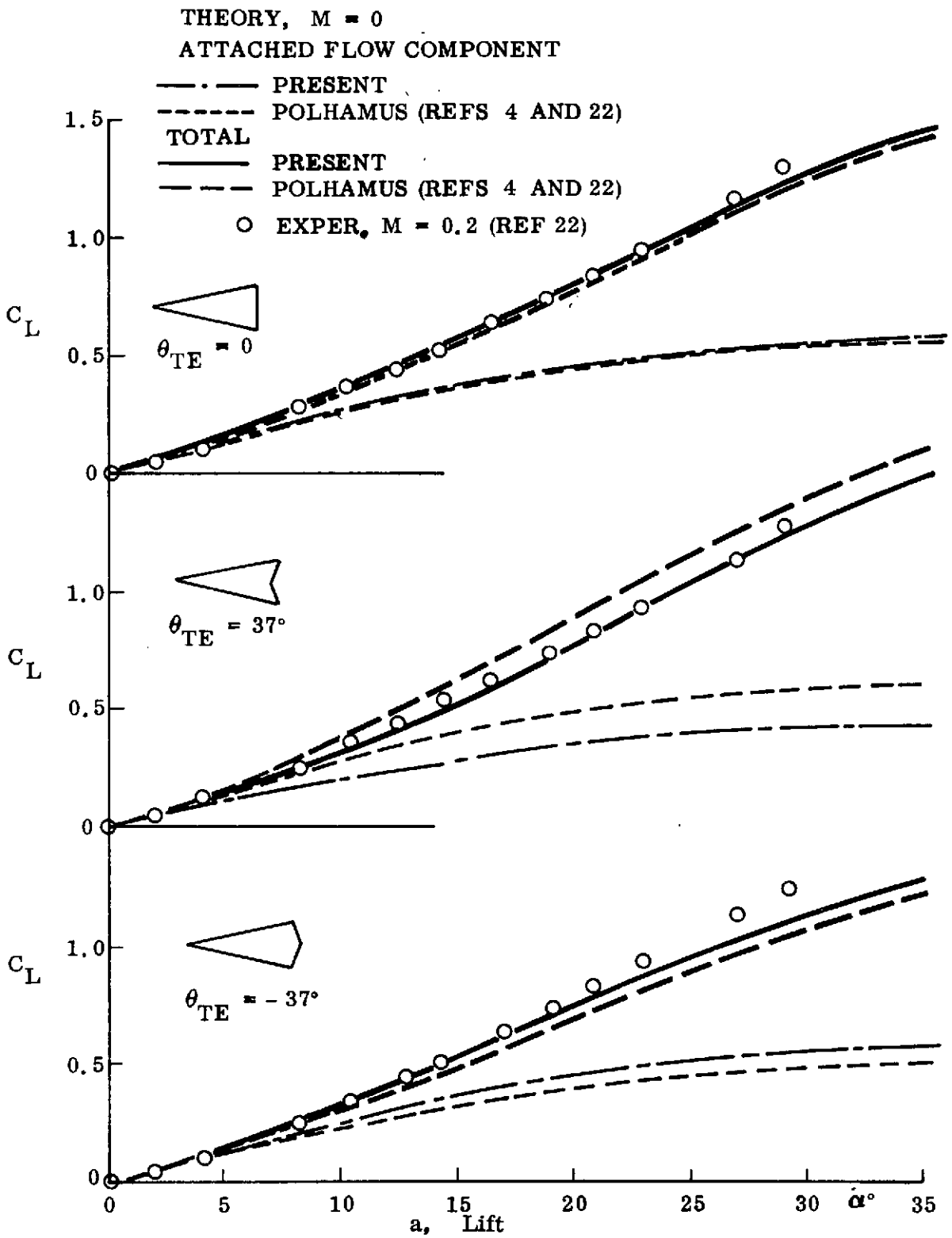

Figure 9. Low Speed Aerodynamic Characteristics of Sharp-Edged Wings with 74° Leading Edge Sweep (Sheet 1 of 2)

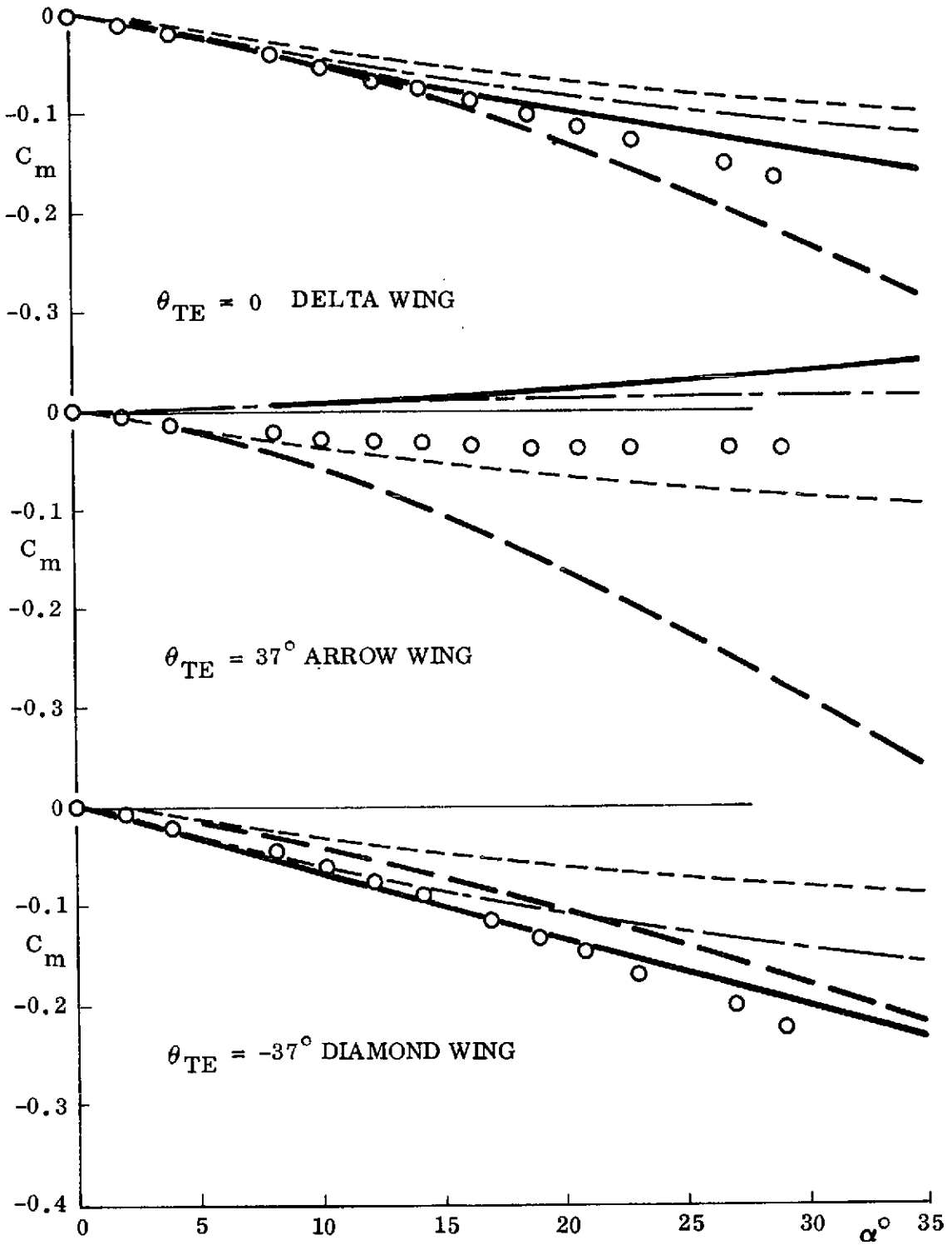

b. Pitching Moment

Figure 9. Low Speed Aerodynamic Characteristics of Sharp-Edged Wings with 74° Leading Edge Sweep (Sheet 2 of 2)

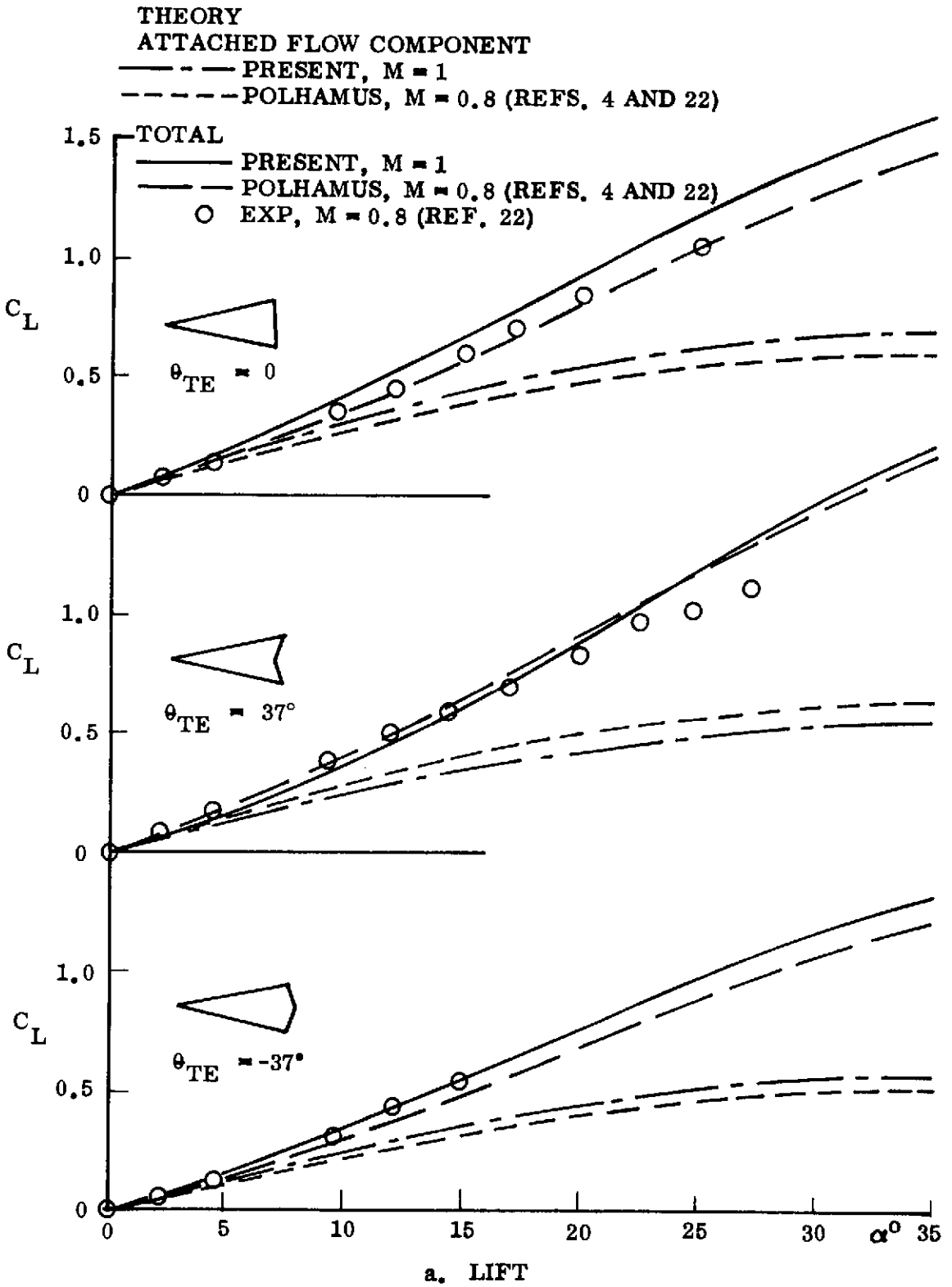

a. LIFT

Figure 10. High Speed Aerodynamic Characteristics of Sharp-Edged Wings with 74° Leading Edge Sweep (Sheet 1 of 2)

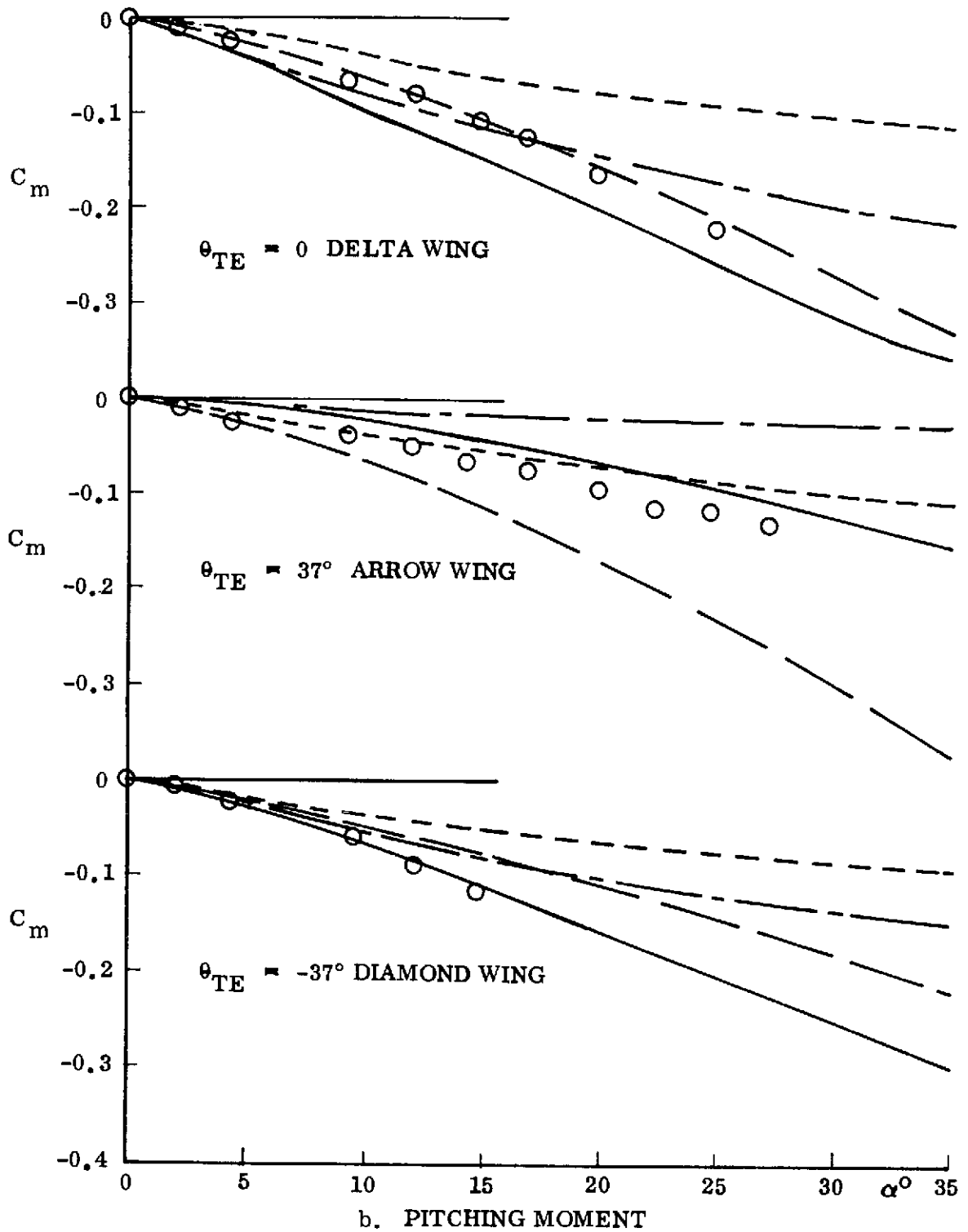

b. PITCHING MOMENT

Figure 10. High Speed Aerodynamic Characteristics of Sharp-Edged Wings with 74° Leading Edge Sweep (Sheet 2 of 2)

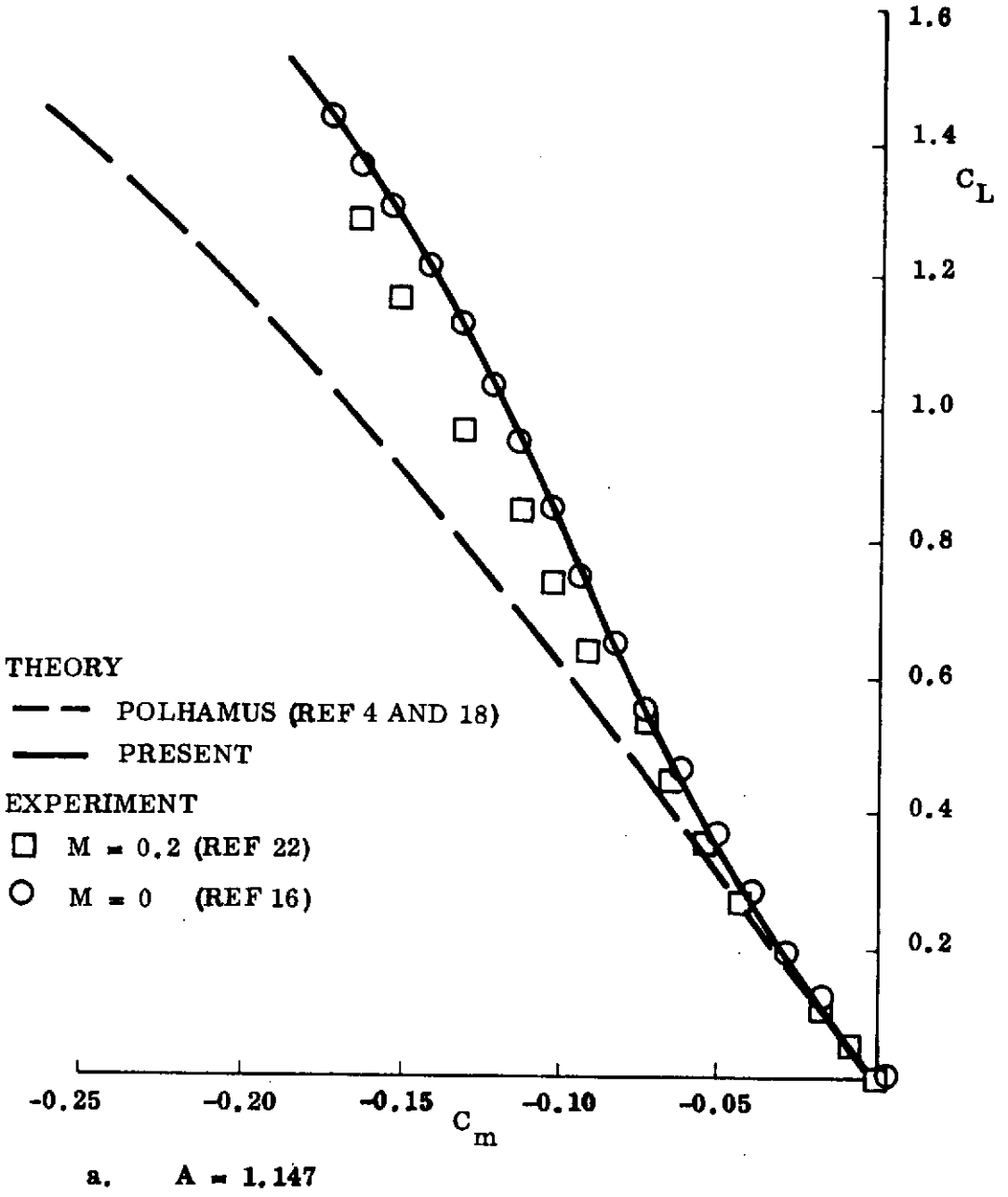

Figure 11. Variation of C_m with C_L for Sharp-Edged Slender Delta Wings (Sheet 1 of 2)

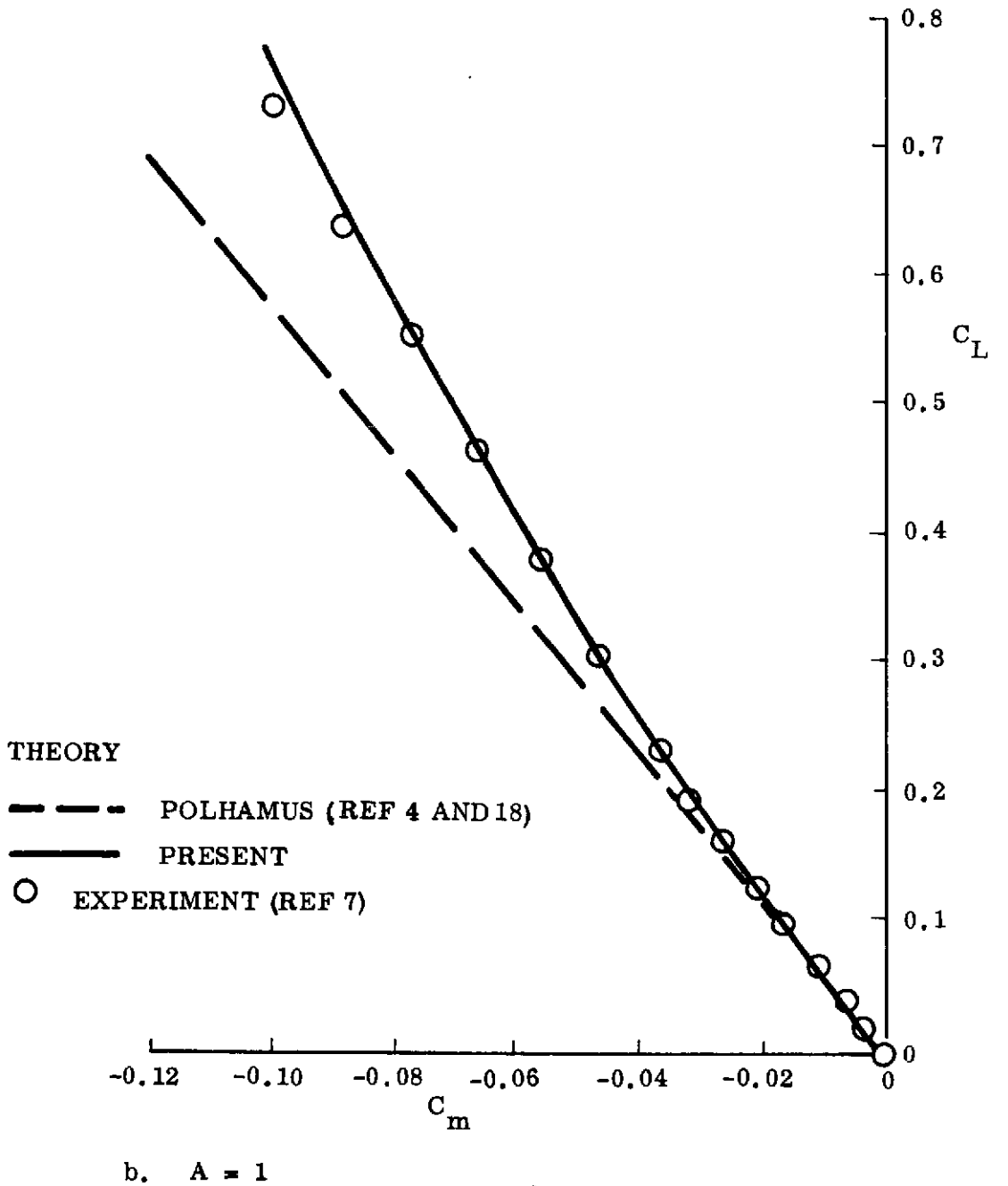

b. A = 1

Figure 11. Variation of C_m with C_L for Sharp-Edged Slender Delta Wings (Sheet 2 of 2)

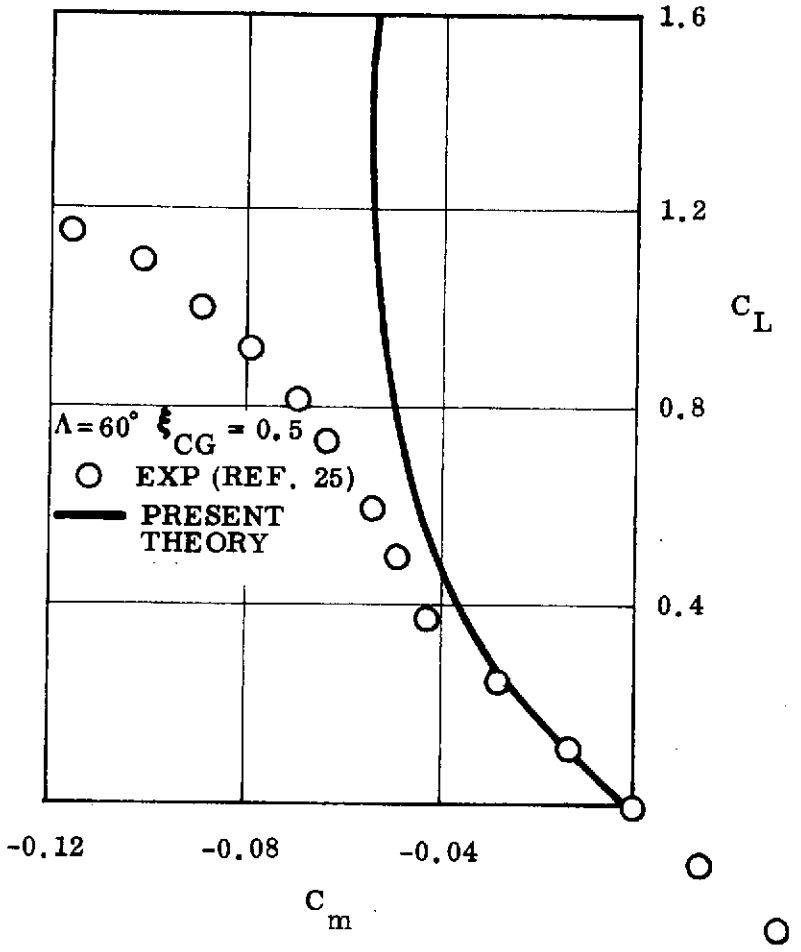

Figure 12. C_m (C_L) Data for a Sharp-Edged A = 2.3 Delta Wing

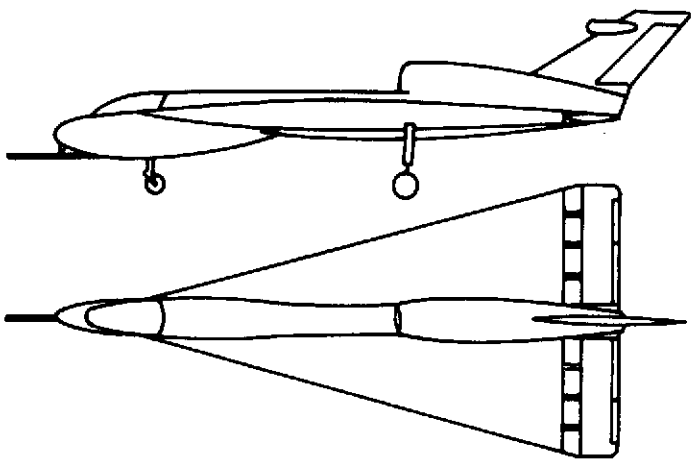

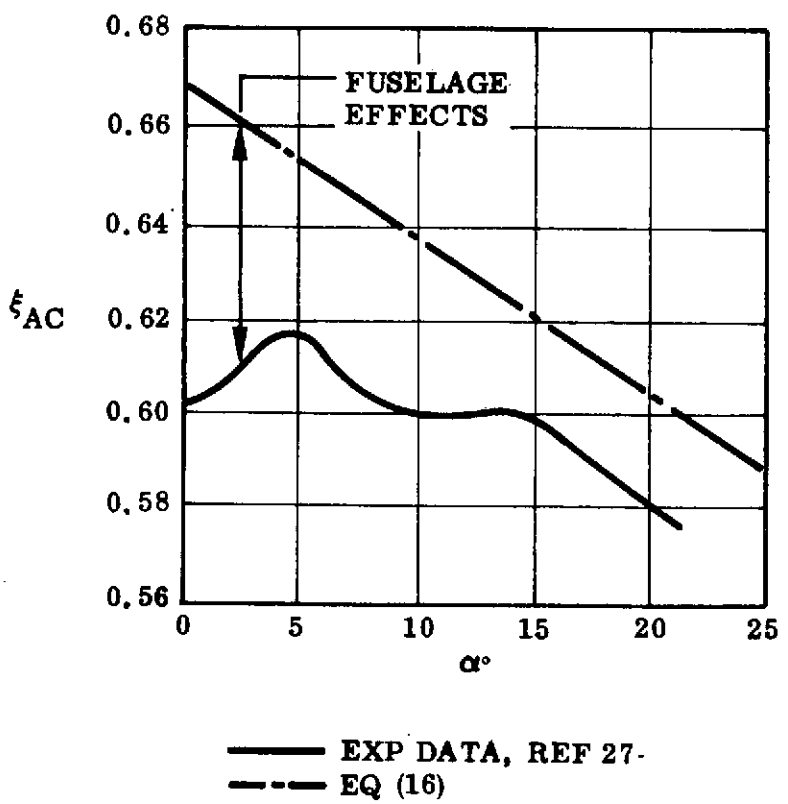

Figure 13. Effect of Angle of Attack on the Aerodynamic Center of the Handley-Page-115

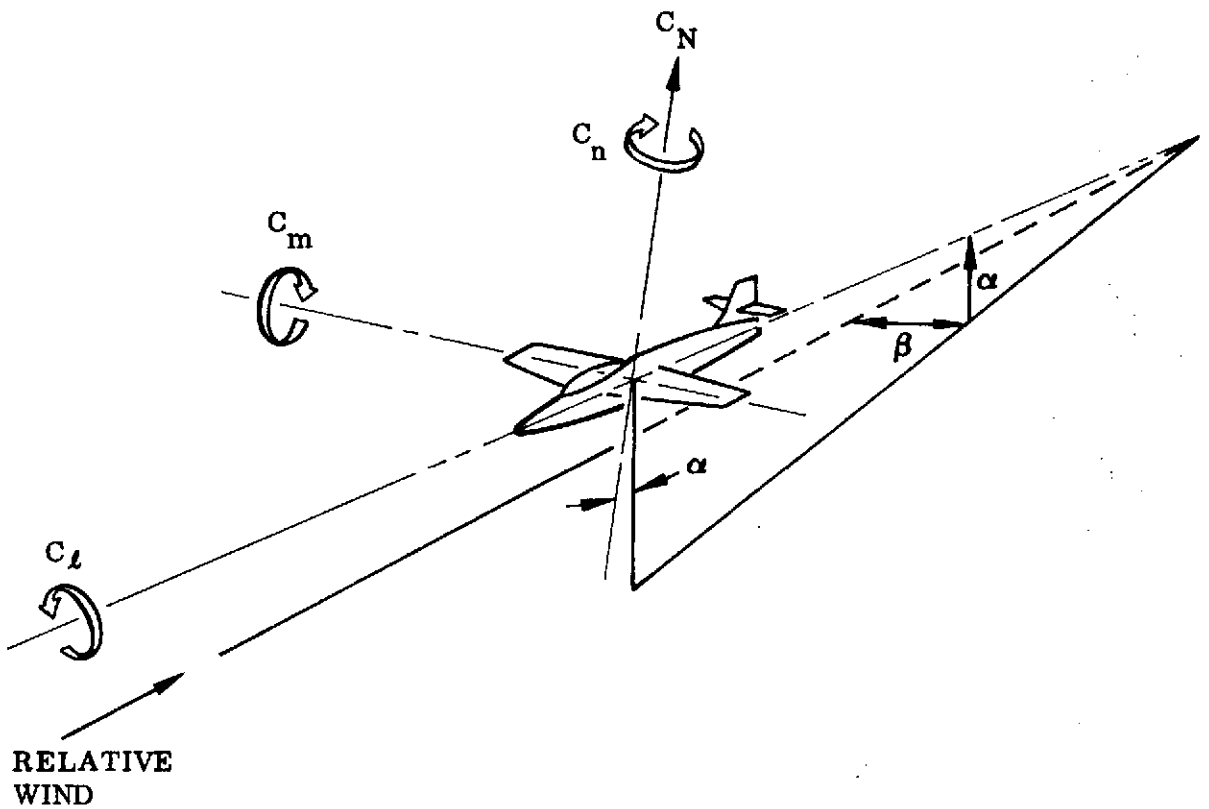

Figure 14. Definition of 6-D Parameters (arrows indicate positive directions of moments, forces, and angles)

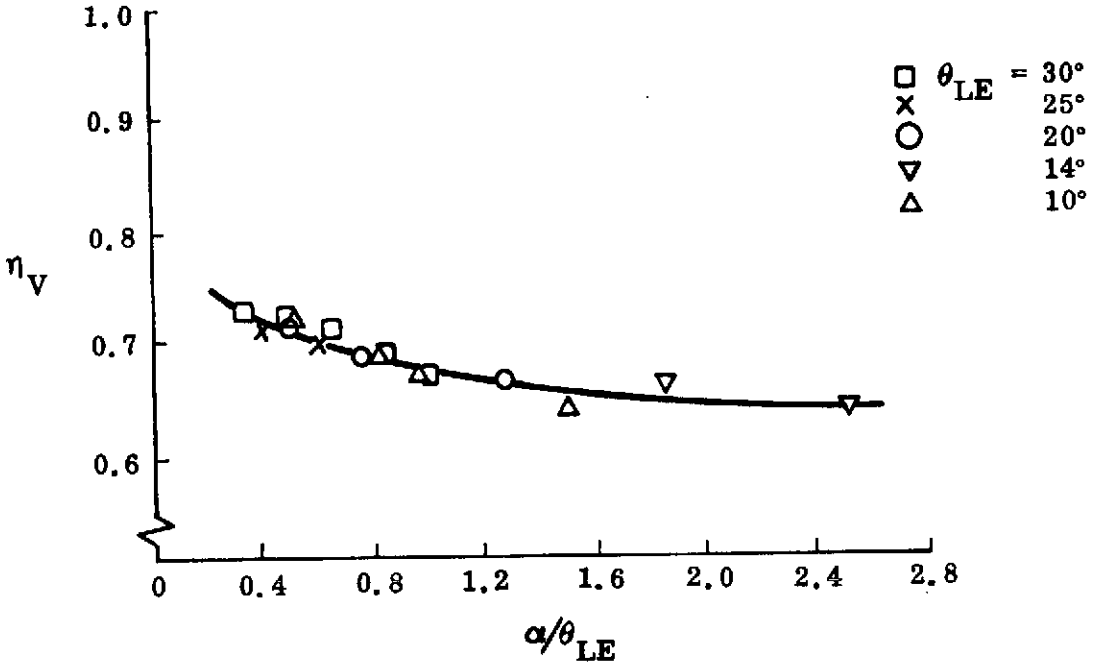

a. EFFECT OF LEADING EDGE SWEEP

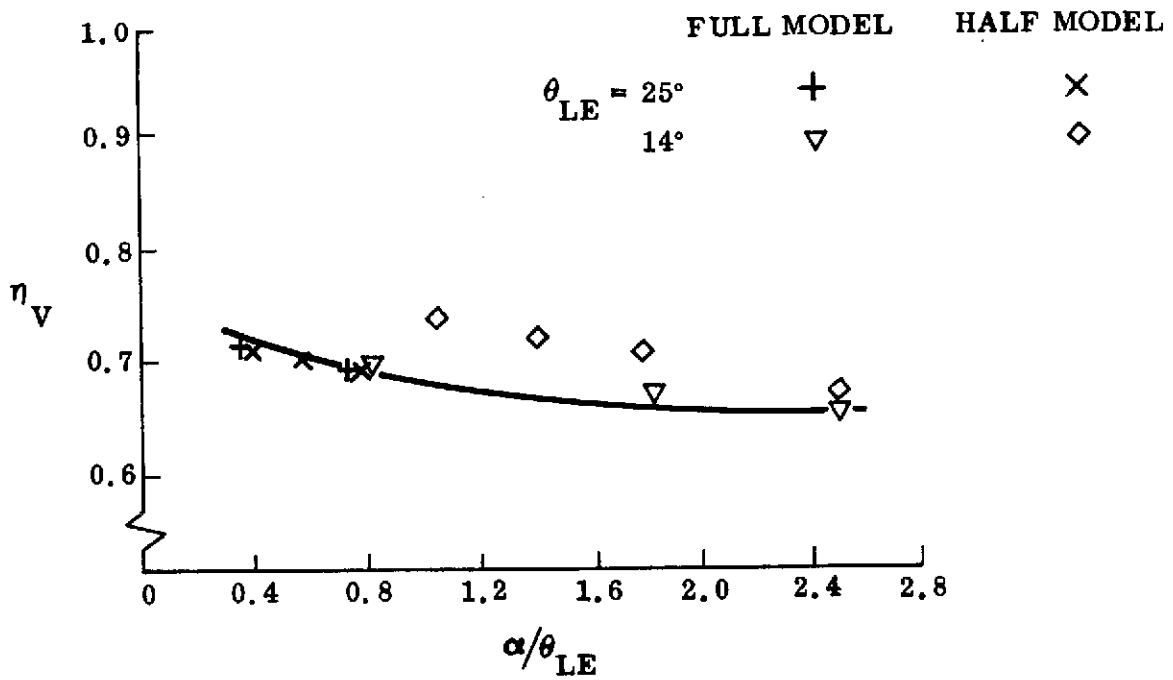

b. EFFECT OF SPLITTER PLATE

Figure 15. Leading Edge Vortex Position on Sharp-Edged Delta Wings (Ref. 20)

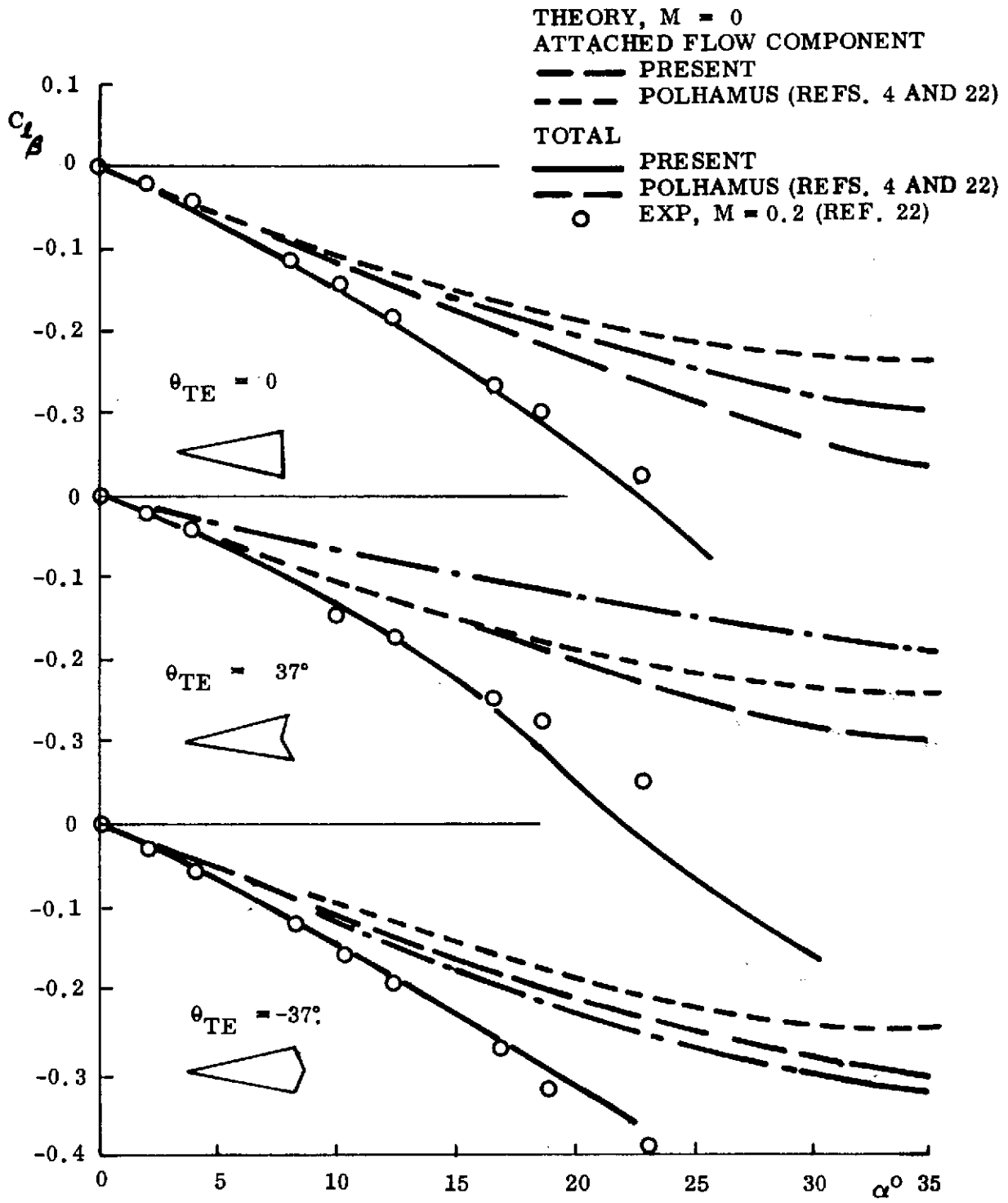

a. LOW SPEED CHARACTERISTICS

Figure 16. Roll-Sideslip-Derivatives of Sharp-Edged Wings with 74° Leading Edge Sweep (Sheet 1 of 2)

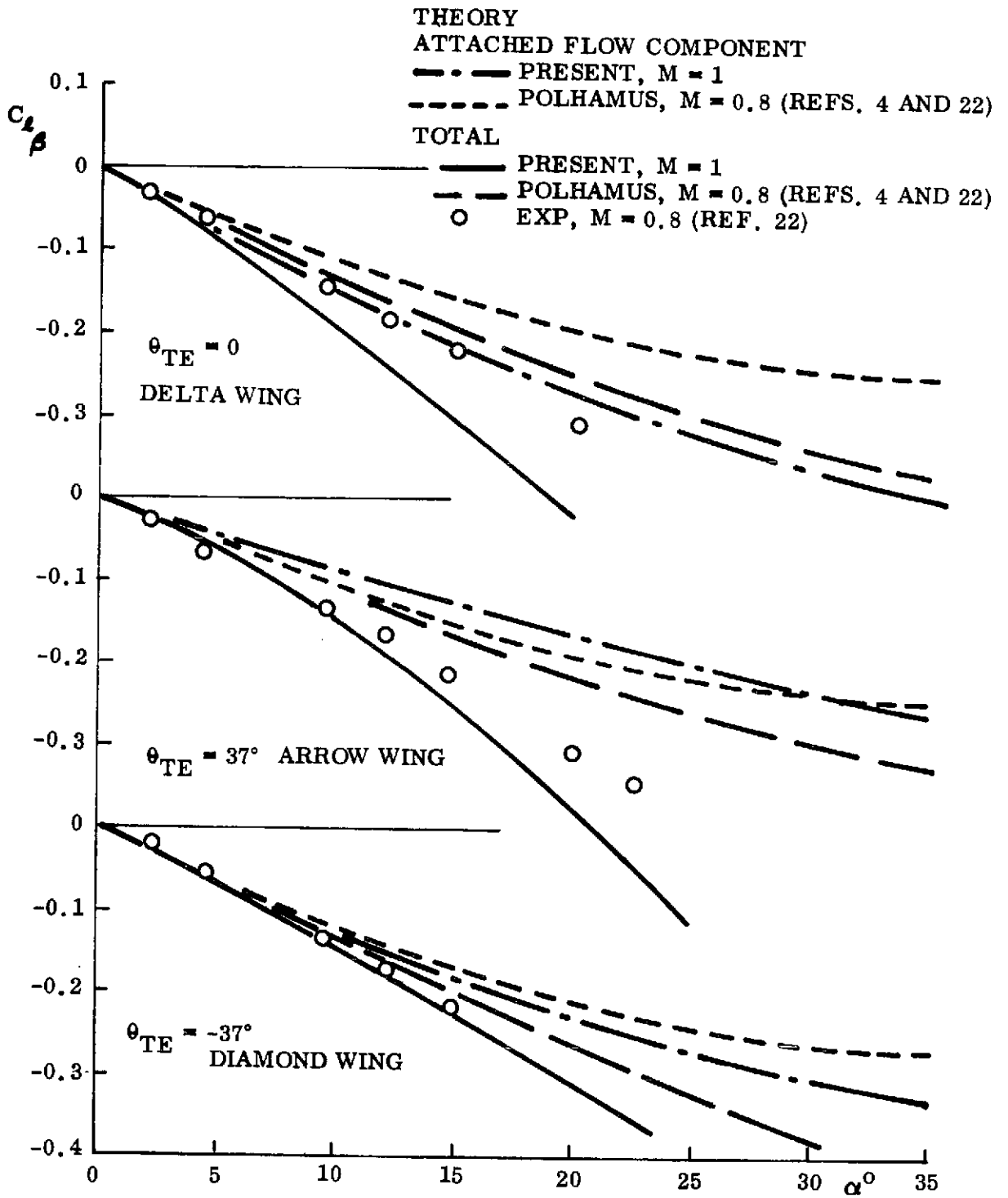

b. HIGH SPEED CHARACTERISTICS

Figure 16. Roll-Sideslip-Derivatives of Sharp-Edged Wings with 74° Leading Edge Sweep (Sheet 2 of 2)

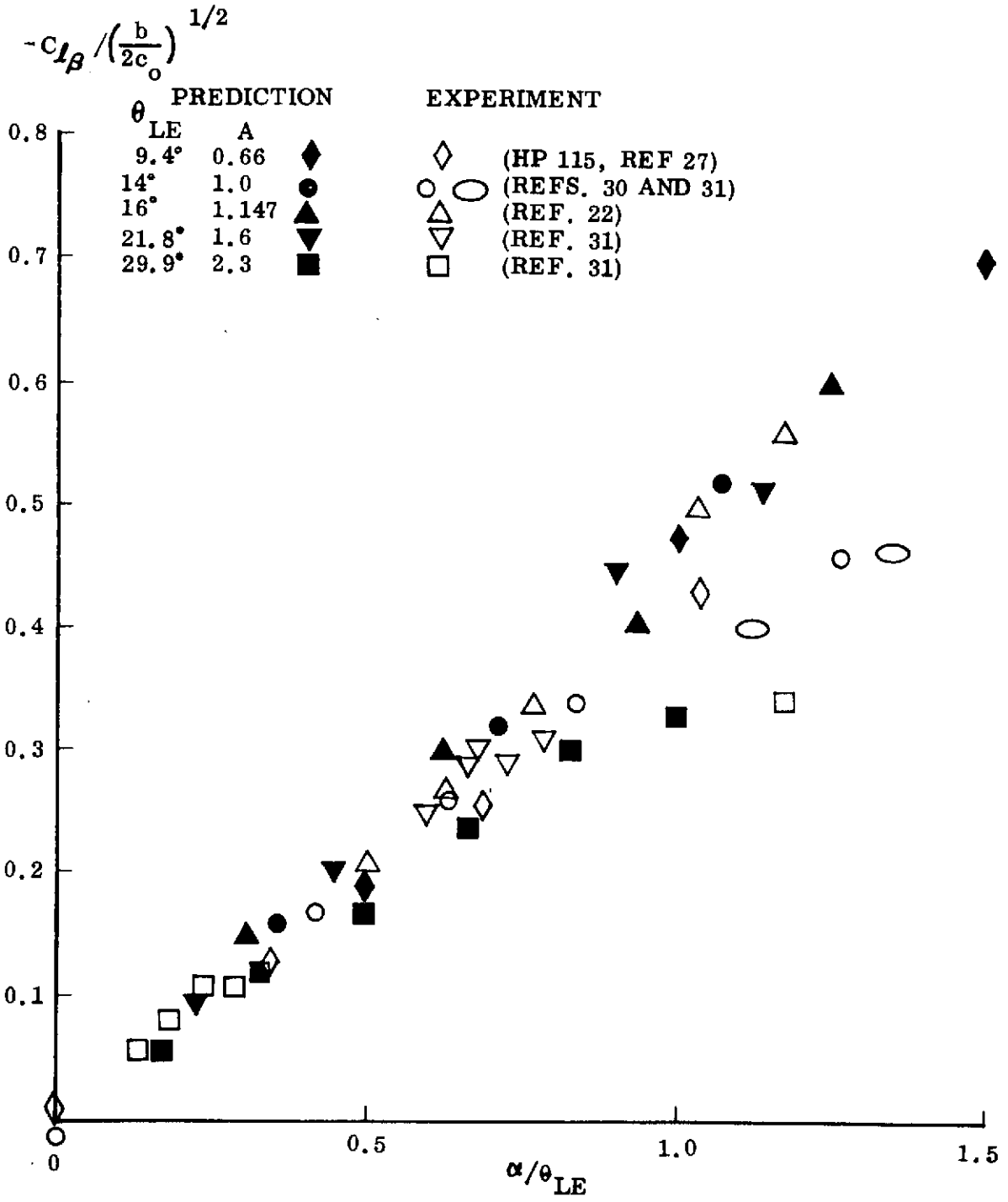

Figure 17. Universal Scaling of Roll-Sideslip Derivatives of Sharp-Edged Delta Wings at Low Speeds

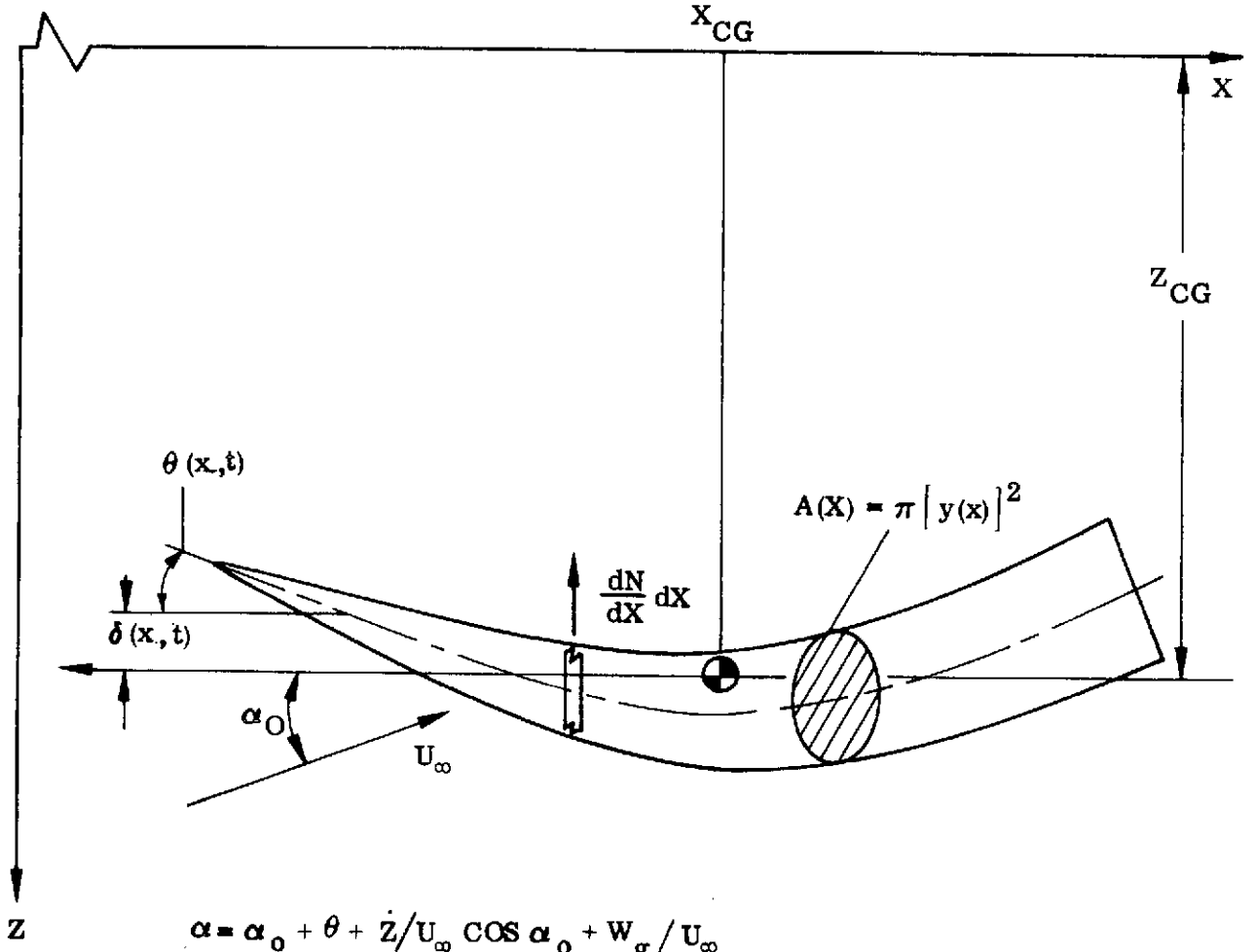

$$\alpha = \alpha_o + \theta + \dot{Z}/U_\infty \cos \alpha_o + W_g/U_\infty$$

$$Z = Z_{CG} - \delta(x,t)$$

$$X = X_{CG} - (x - x_{CG})$$

$$\delta(x,t) = \phi(x)\, q(t)$$

$$\theta(x,t) = \phi'(x)\, q(t)$$

Figure 18. Elastic Vehicle Coordinate System

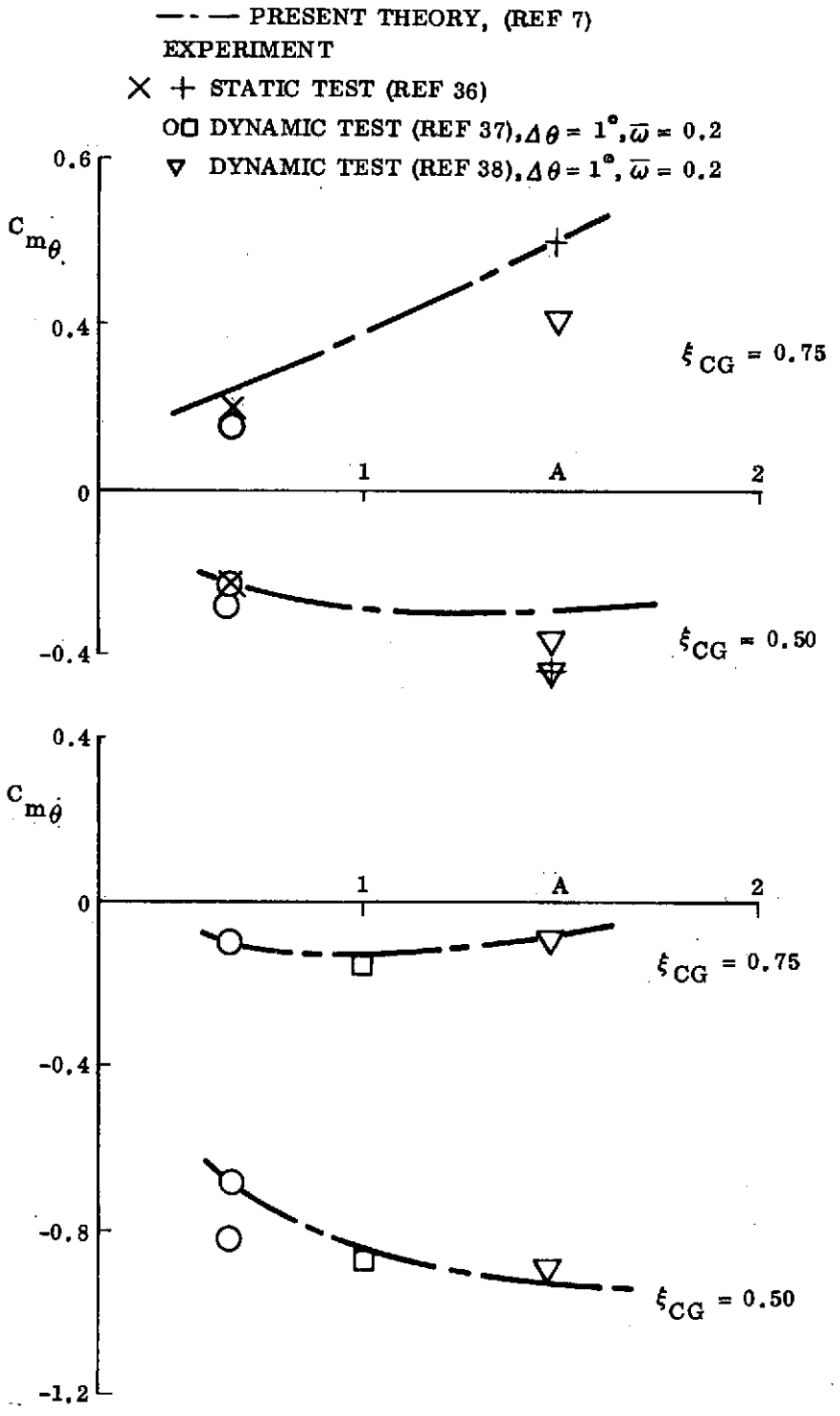

Figure 19. Attached Flow Dynamic Stability Derivatives at α = 0 and M = 0

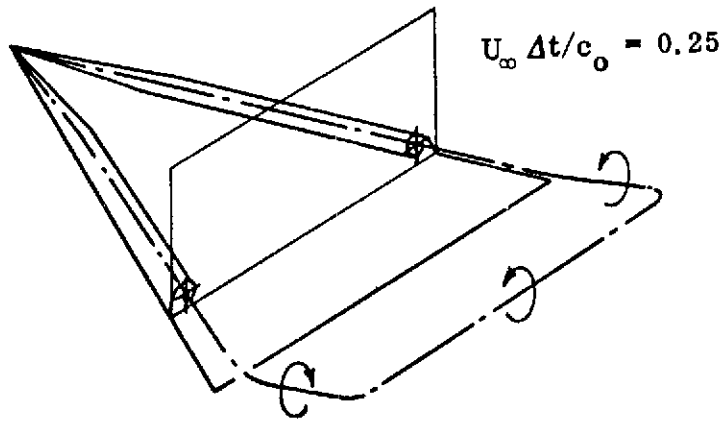

VORTEX AXIS

VORTEX CENTRE

PREVIOUS PATH OF VORTEX CENTRE

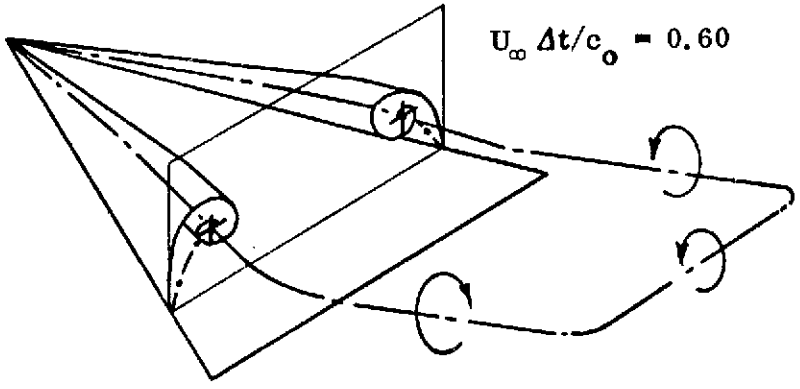

SCHEMATIC REPRESENTATION OF FLOW DURING PLUNGE FROM ZERO TO POSITIVE INCIDENCE

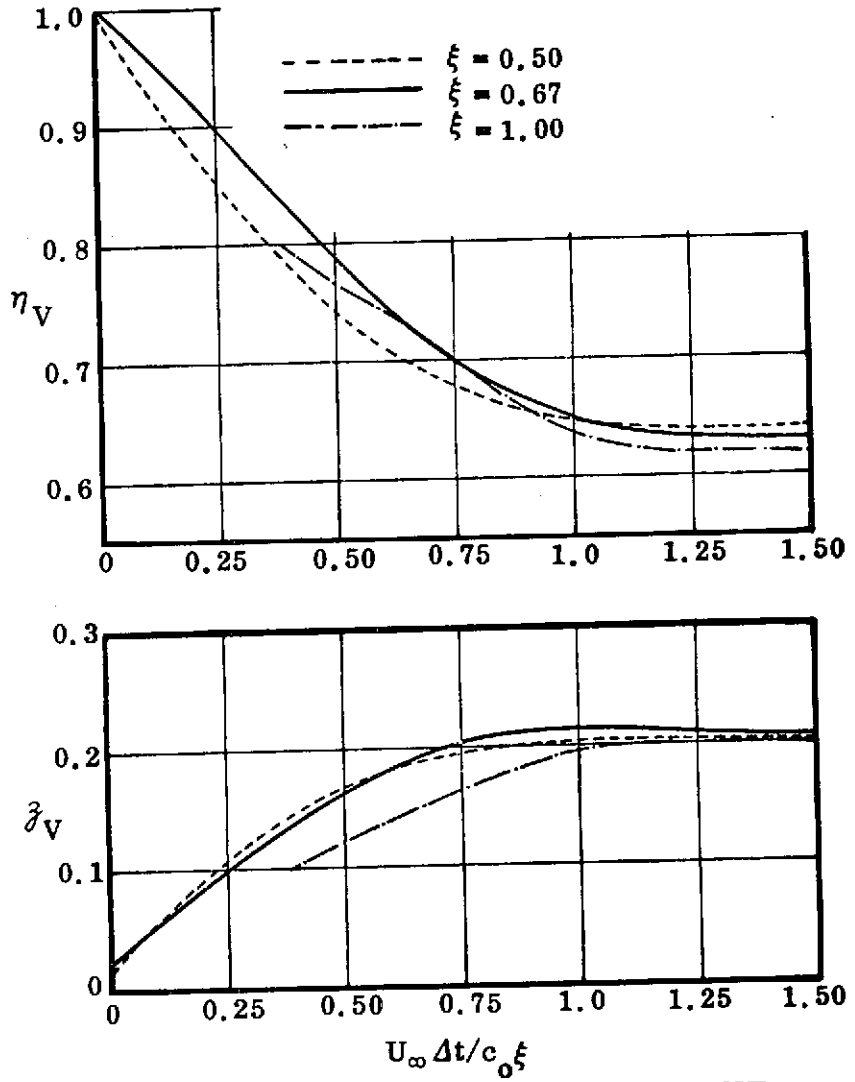

COMPARISON OF η_v, γ_v FOR DIFFERENT CHORDWISE POSITION. $\theta_{LE} = 20°$, $\alpha = 12.4°$

Figure 20. Leading Edge Vortex Formation During Plunge from Zero to Positive Angle of Attack (Ref. 41)

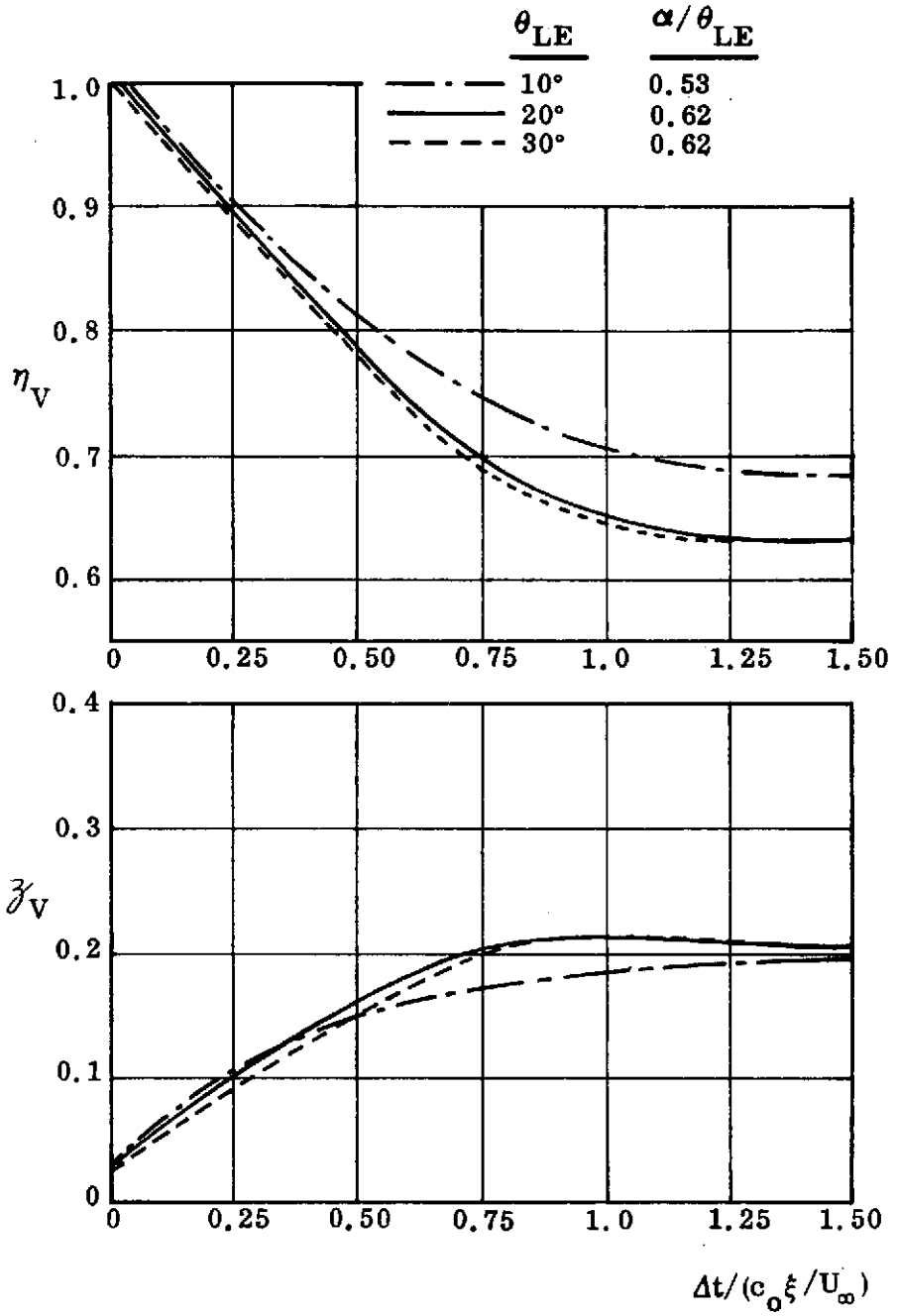

Figure 21. Transient Vortex Position for the Same α/θ_{LE} (Ref. 41)

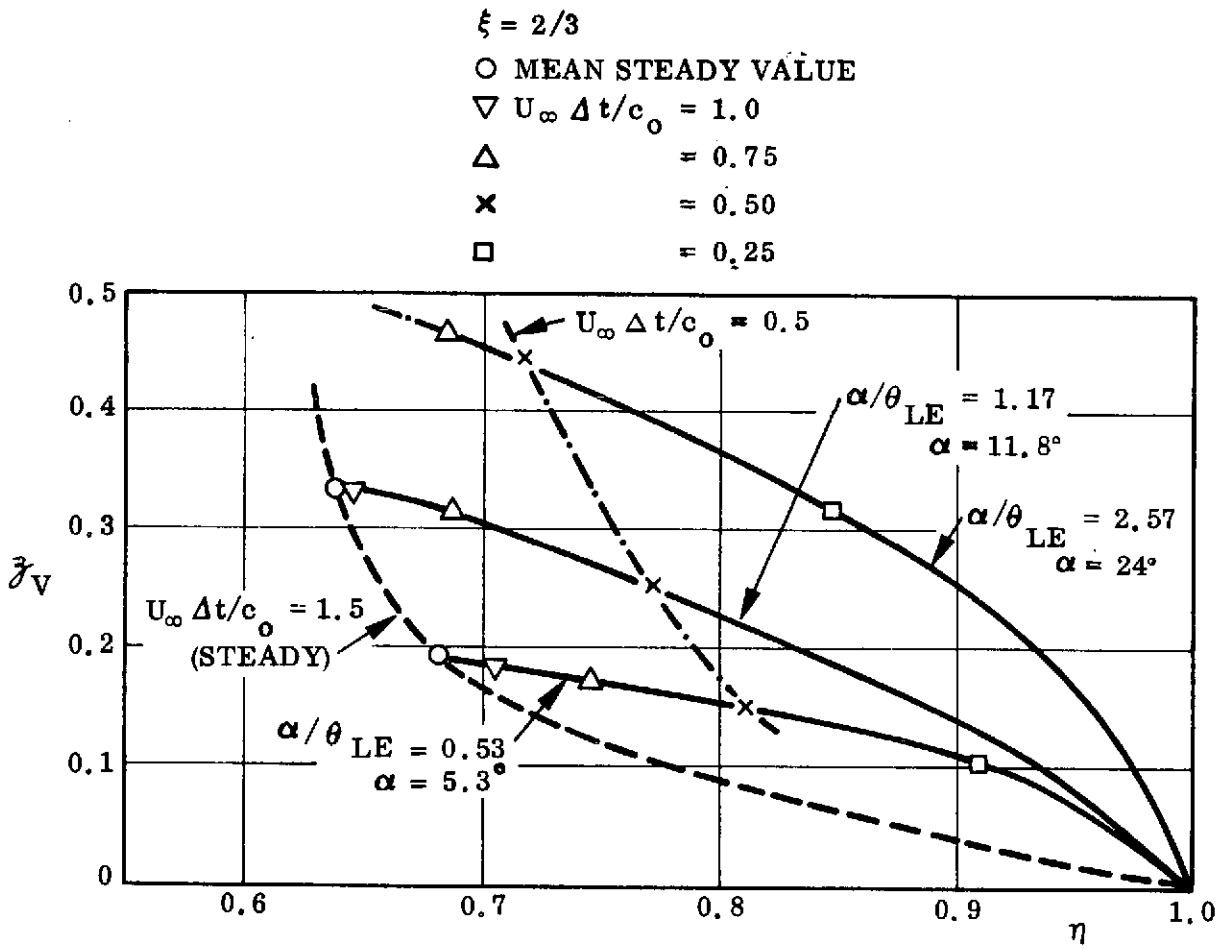

Figure 22. Vortex Paths in Crossflow Plane for 80° Leading Edge Sweep (Ref. 41)

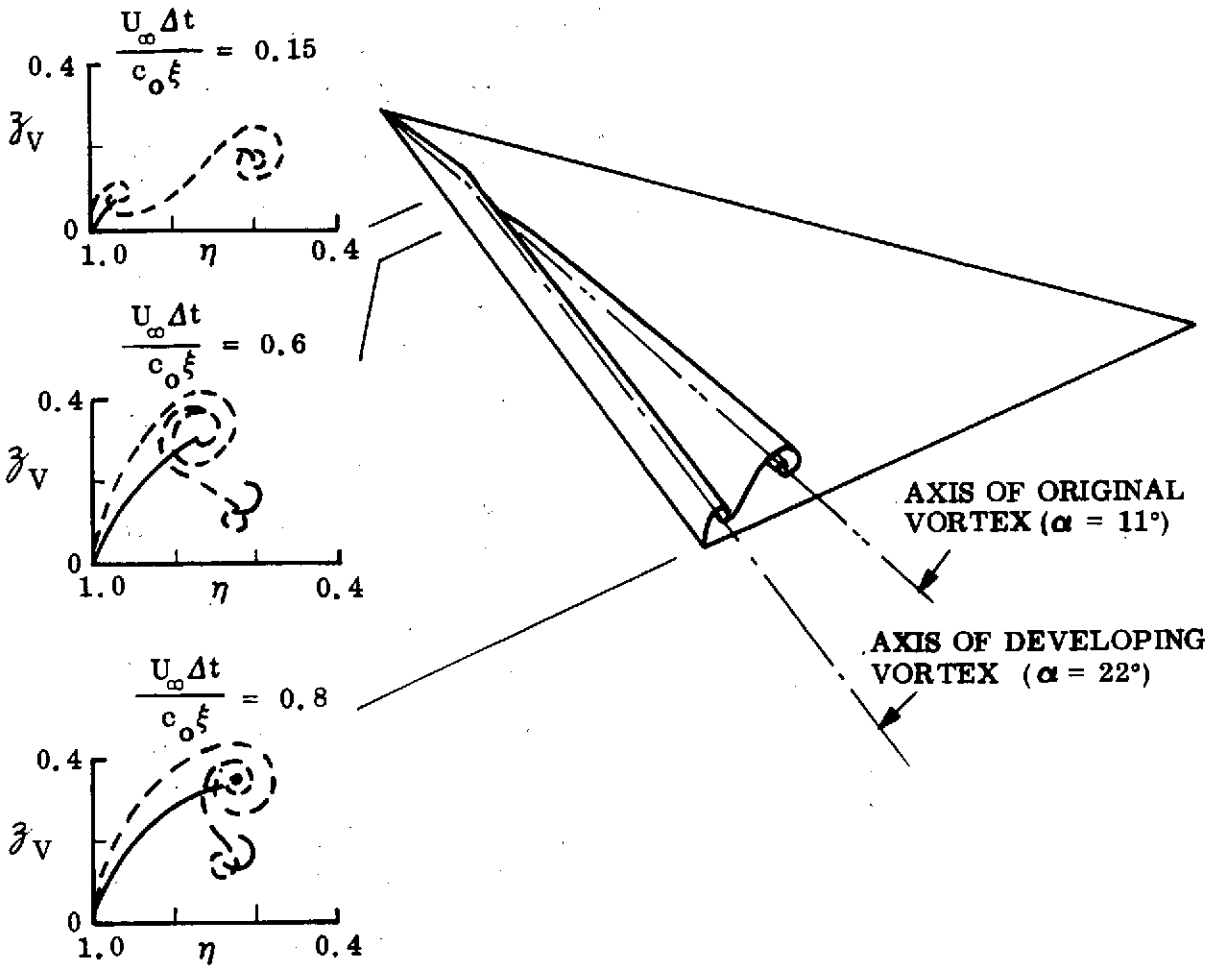

(a) SKETCHES OF TRANSIENT VORTEX FLOW FOLLOWING A CHANGE FROM α = 11° TO α = 22°

Figure 23. Effect of Stepwise Increase of Angle of Attack (Ref. 41)
(Sheet 1 of 2)

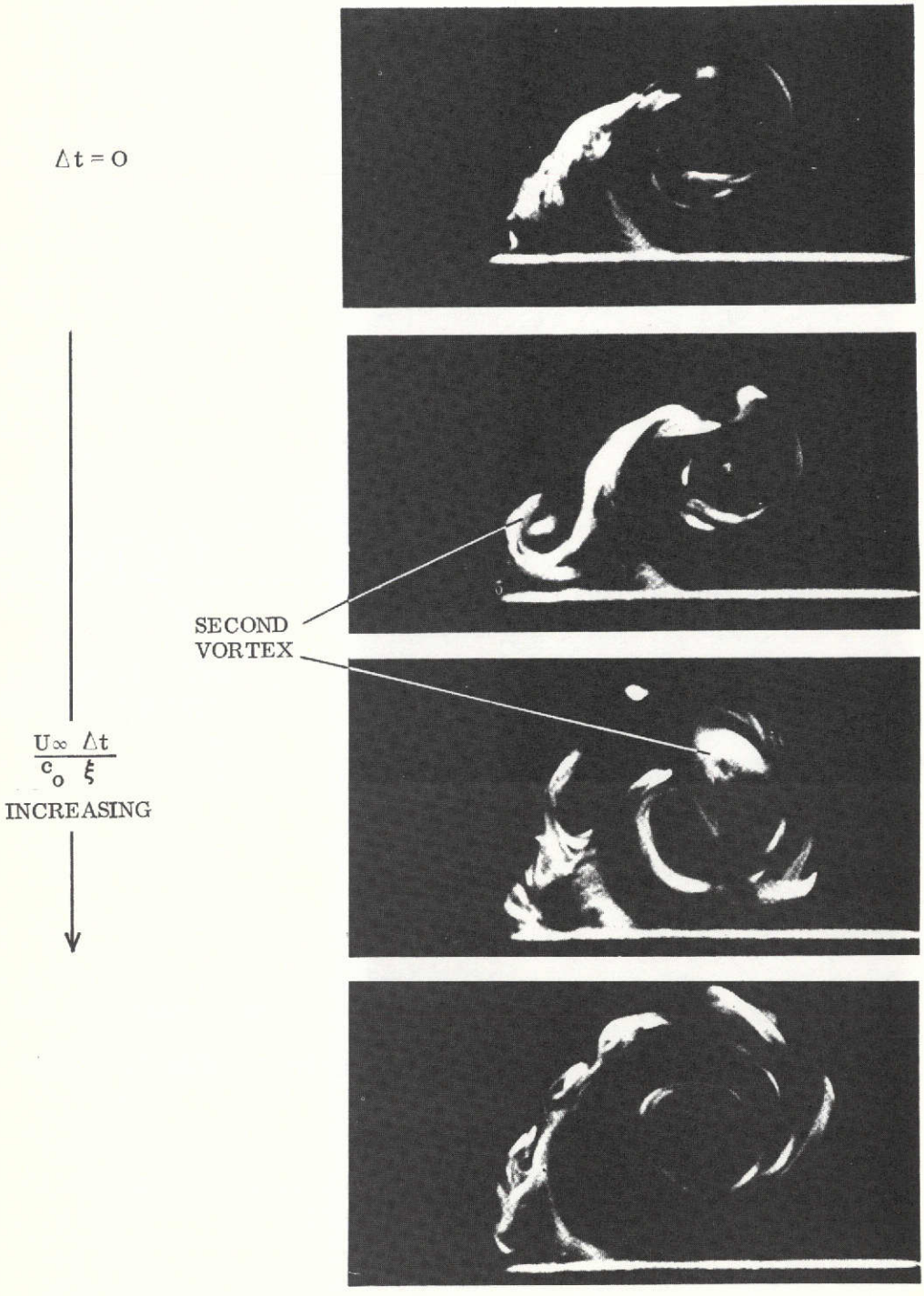

b. FLOW PHOTOGRAPHS OF TRANSIENT VORTEX FLOW FOLLOWING A CHANGE FROM $\alpha = 11^\circ$ TO $\alpha = 18^\circ$

Figure 23. Effect of Stepwise Increase of Angle of Attack (Ref. 41) (Sheet 2 of 2)

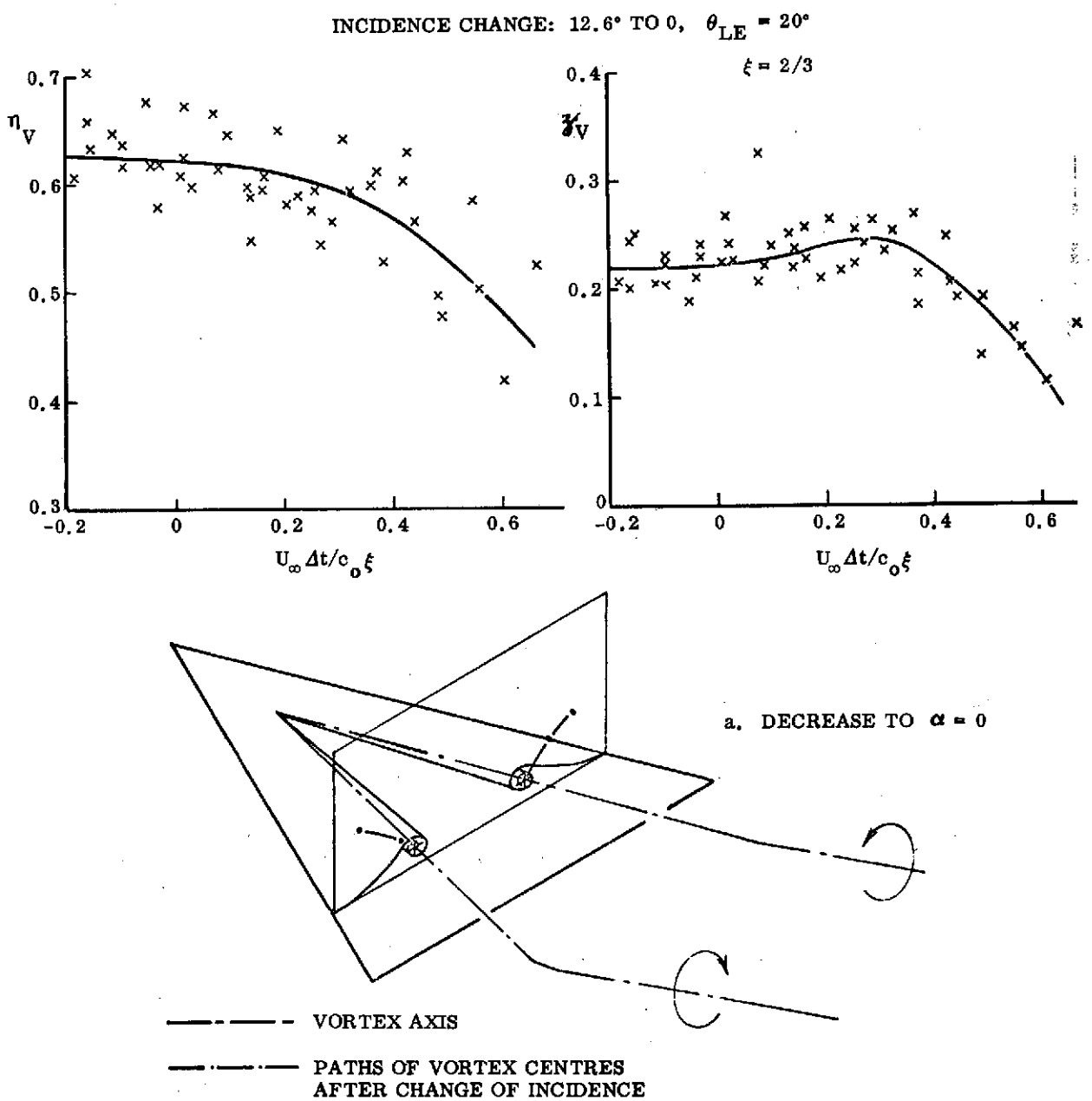

Figure 24. Effect of Stepwise Decrease of Angle of Attack (Ref. 41)
(Sheet 1 of 2)

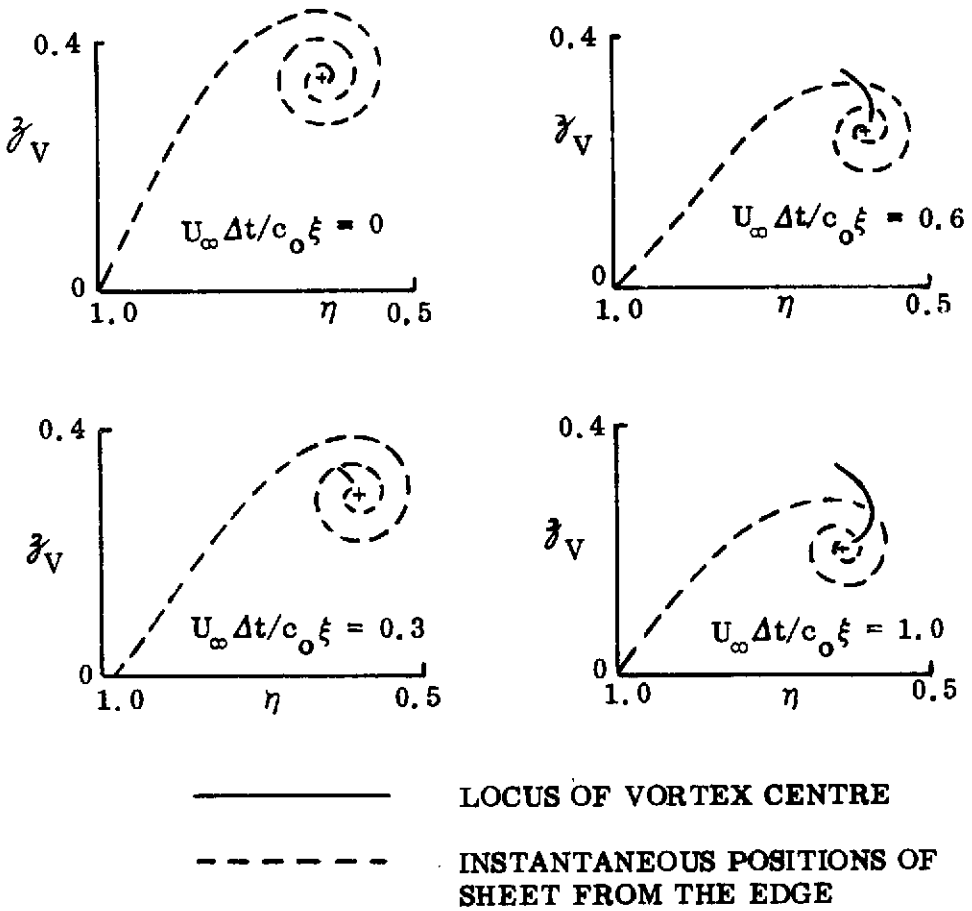

b. DECREASE FROM $\alpha = 22°$ TO $\alpha = 11°$

Figure 24. Effect of Stepwise Decrease of Angle of Attack (Ref. 41) (Sheet 2 of 2)

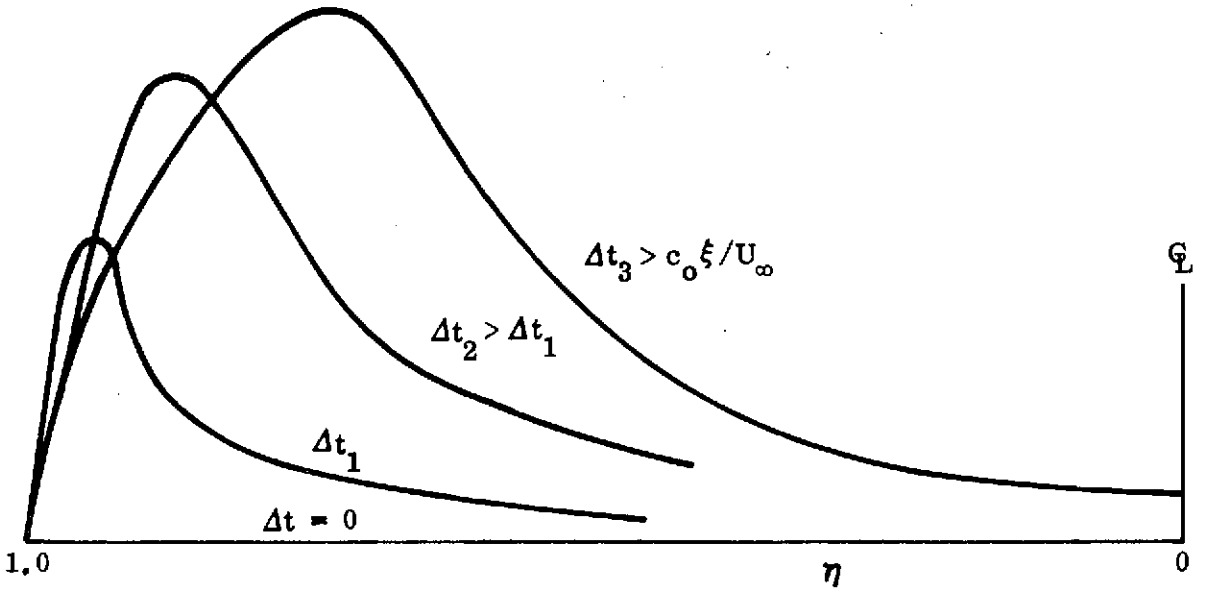

a. INCREASING α

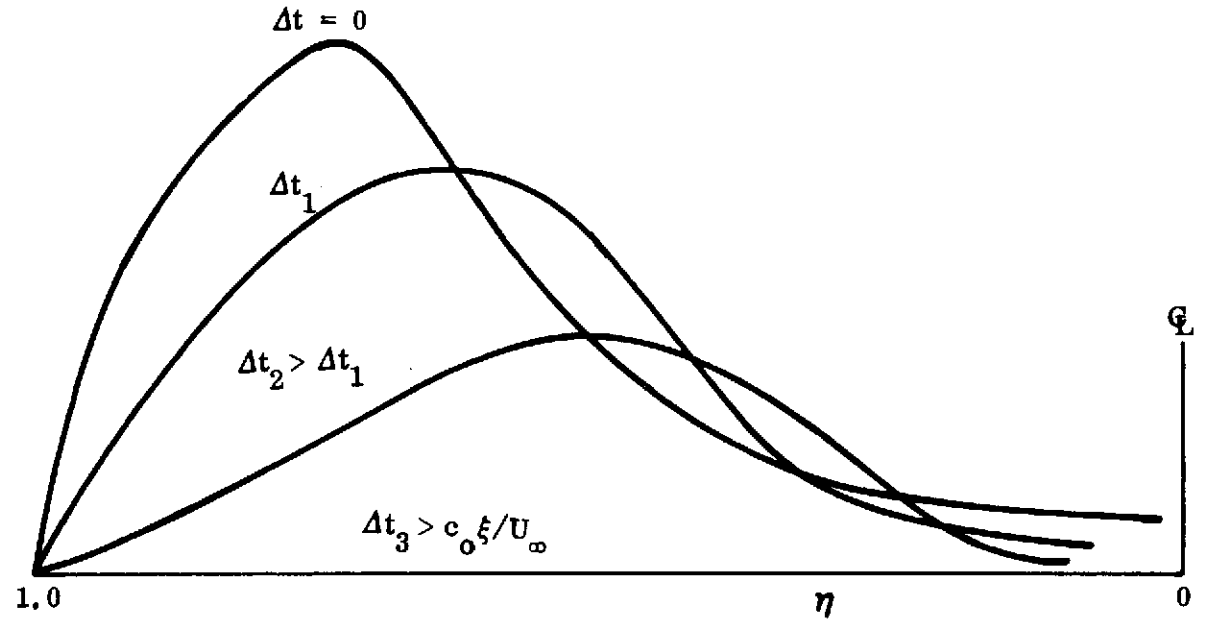

b. DECREASING α

Figure 25. Suggested Transient Spanwise Lift Distributions (Ref. 41)

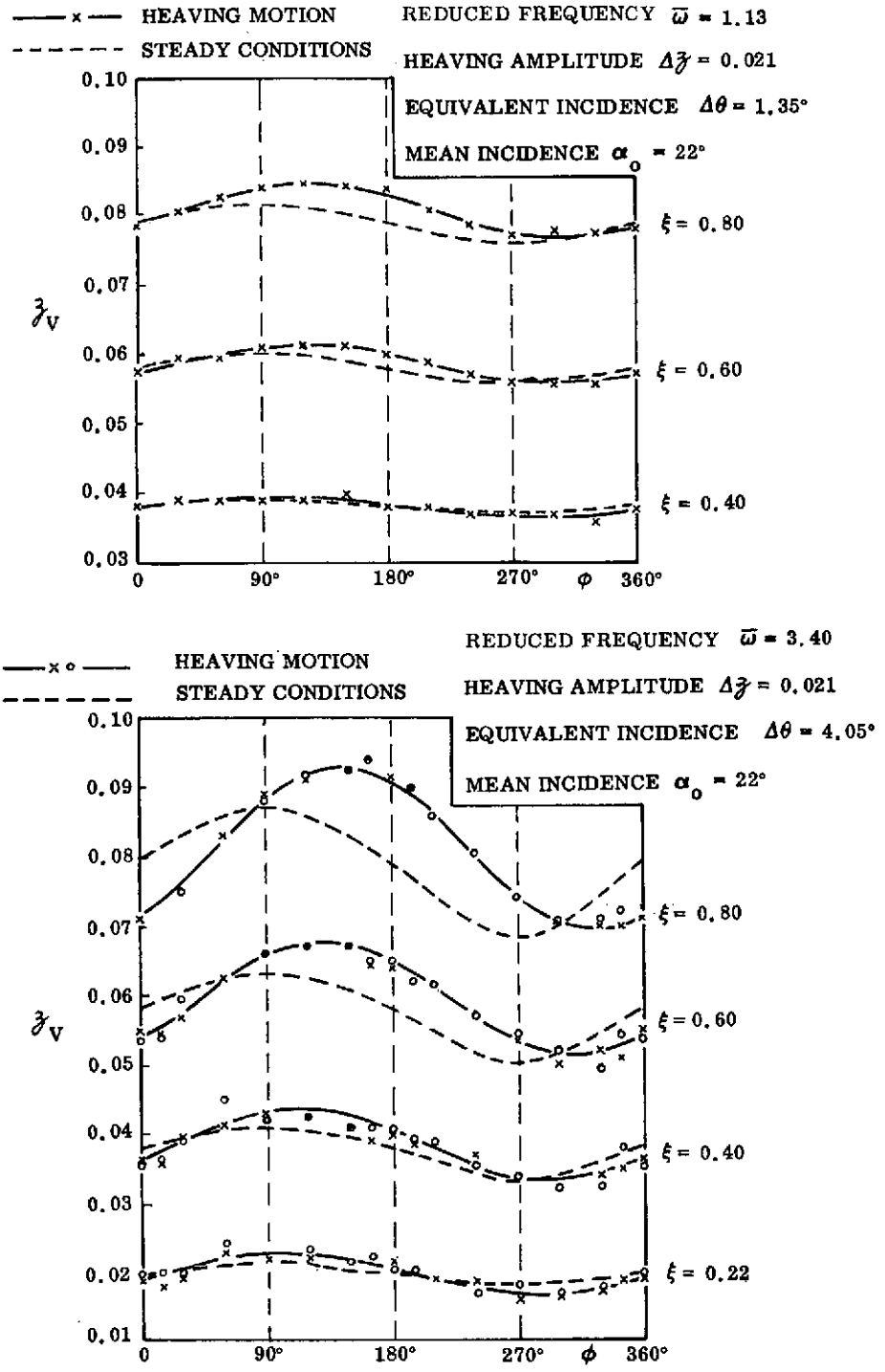

a. NOT CORRECTED FOR PHASE LAG

Figure 26. Cyclic Variation of Vortex Height on a Sharp-Edged A = 1 Delta Wing (Ref. 19) (Sheet 1 of 2)

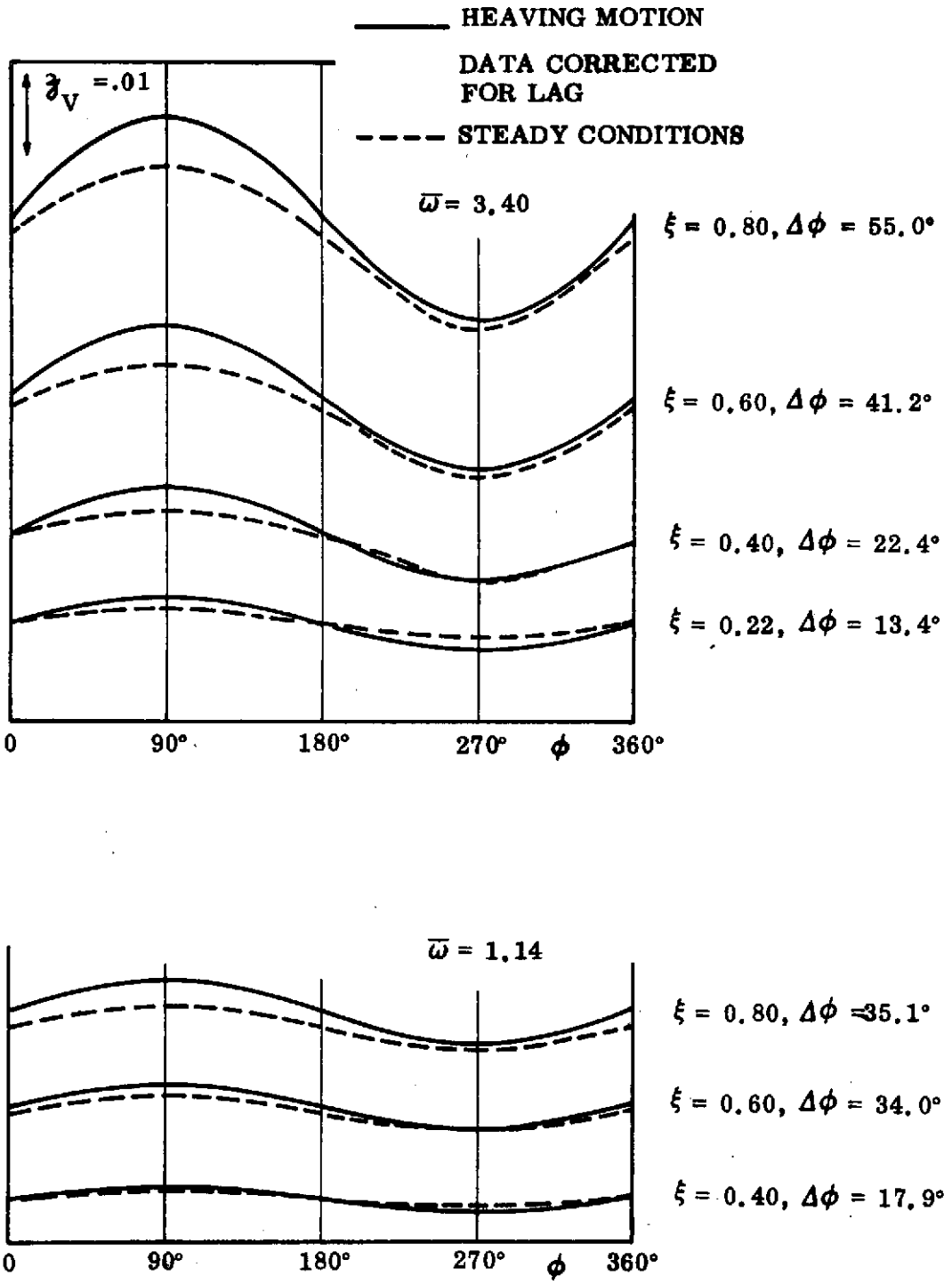

b. CORRECTED FOR PHASE LAG

Figure 26. Cyclic Variation of Vortex Height on a Sharp-Edged A = 1 Delta Wing (Ref. 19) (Sheet 2 of 2)

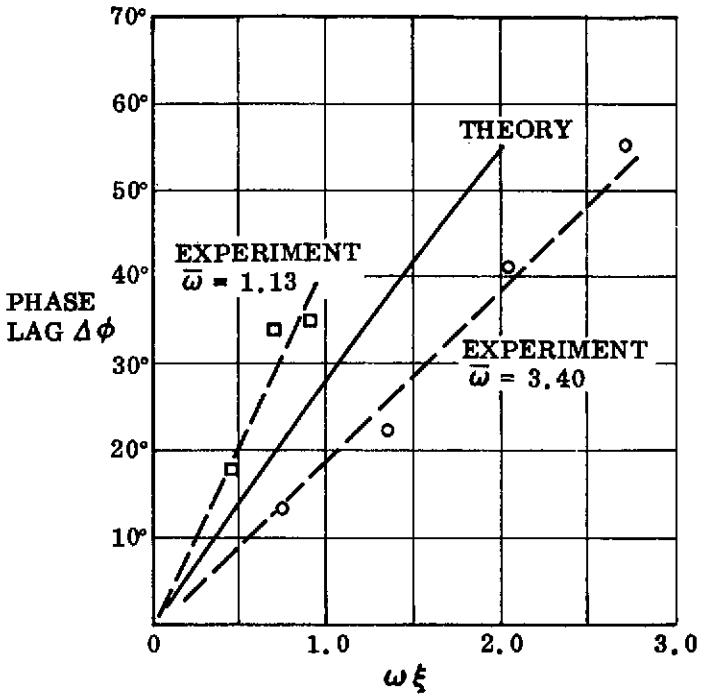

a. PHASE LAG VERSUS LOCAL FREQUENCY PARAMETER

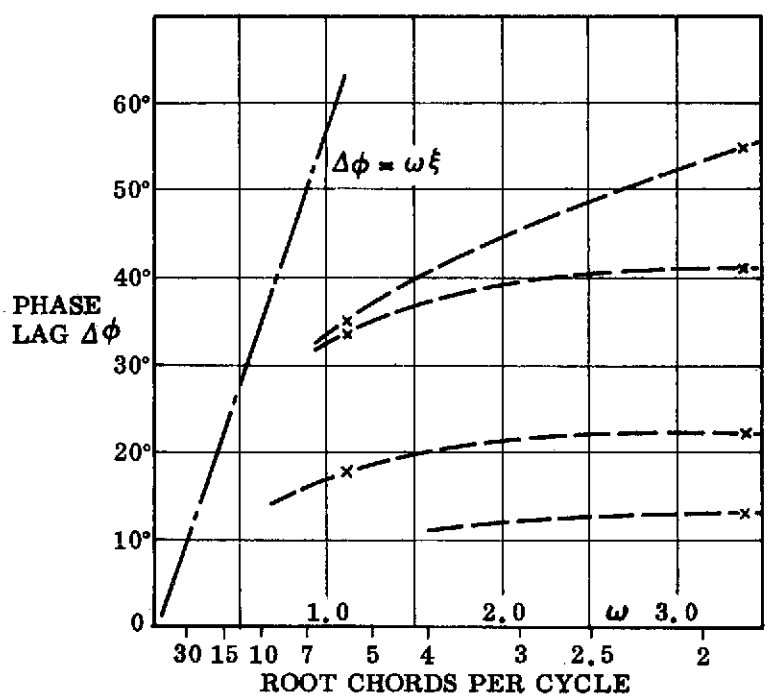

b. PHASE LAG VERSUS REDUCED FREQUENCY

Figure 27. Effect of Frequency on Cyclic Vortex Height Variation (Ref. 19)

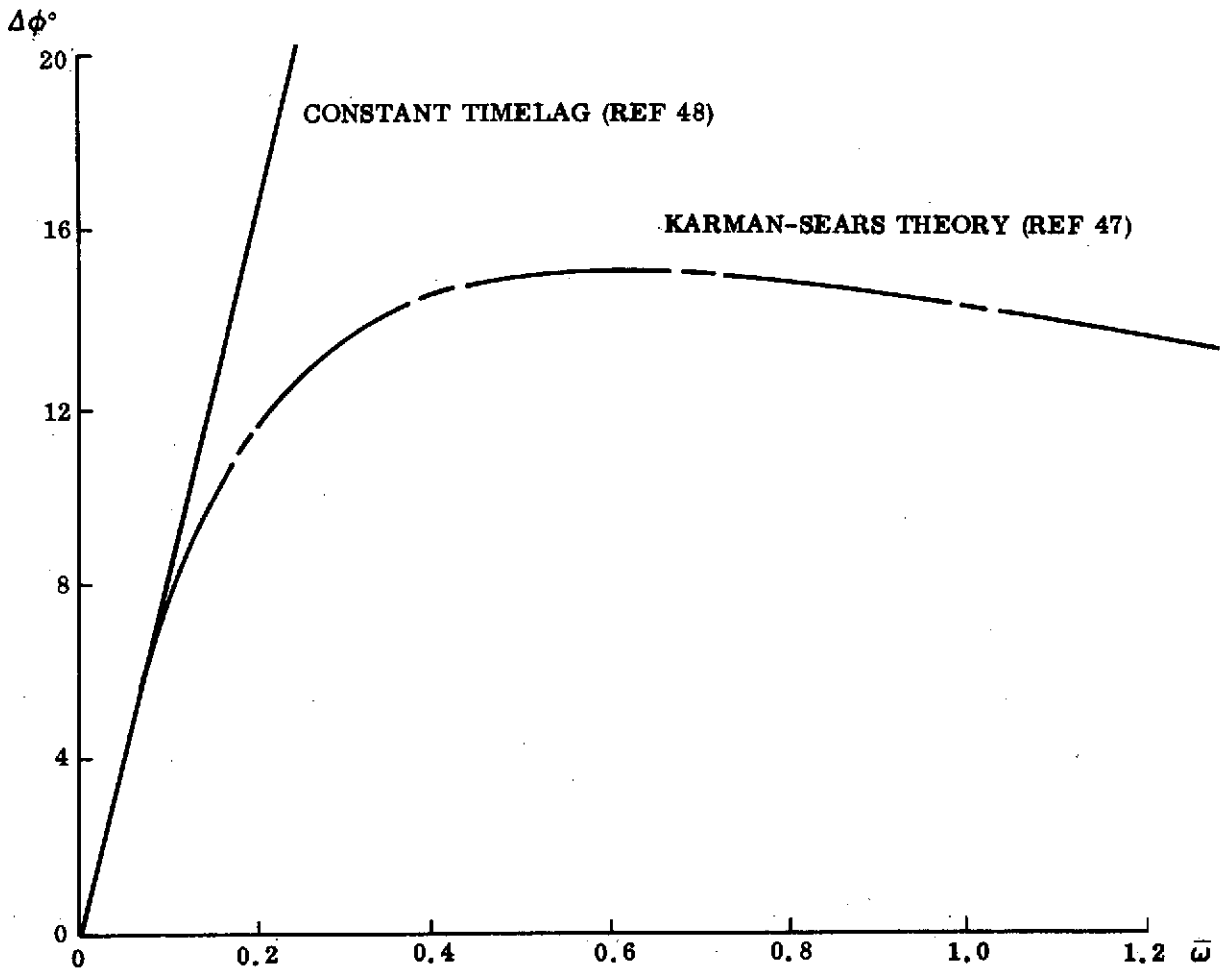

Figure 28. Karman-Sears Vortex-Wake Lag

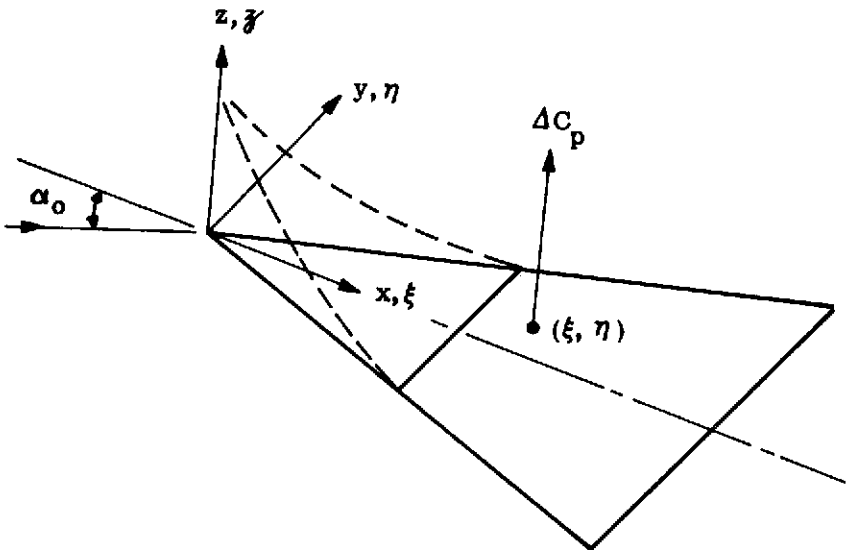

a. COORDINATE SYSTEM

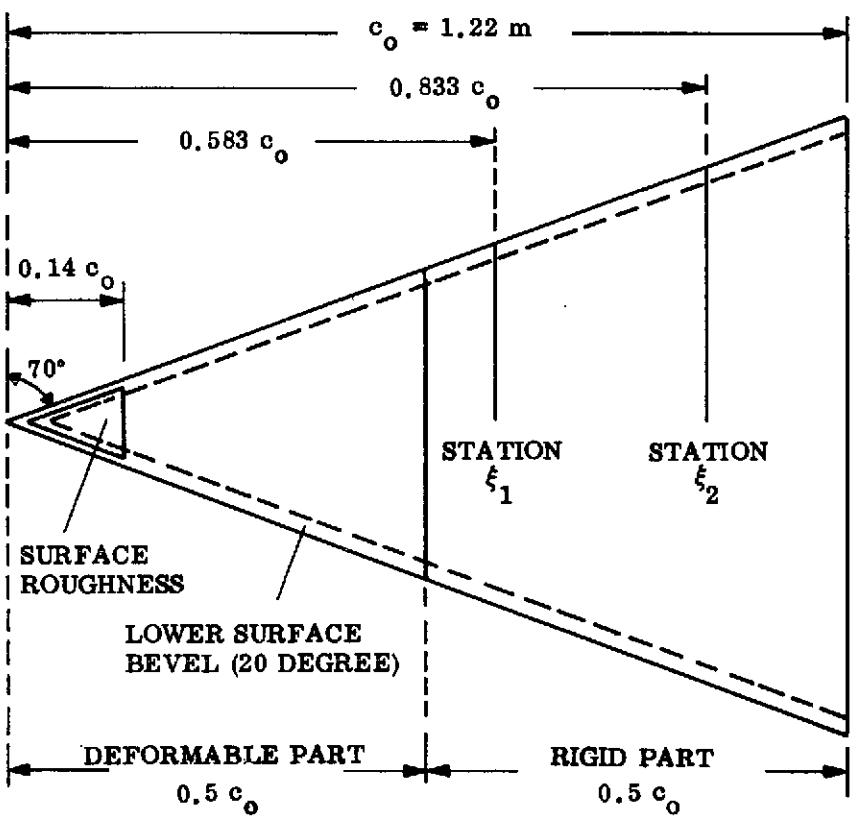

b. MODEL AND INSTRUMENTATION

Figure 29. Oscillatory Bending Deformation (Ref. 42)

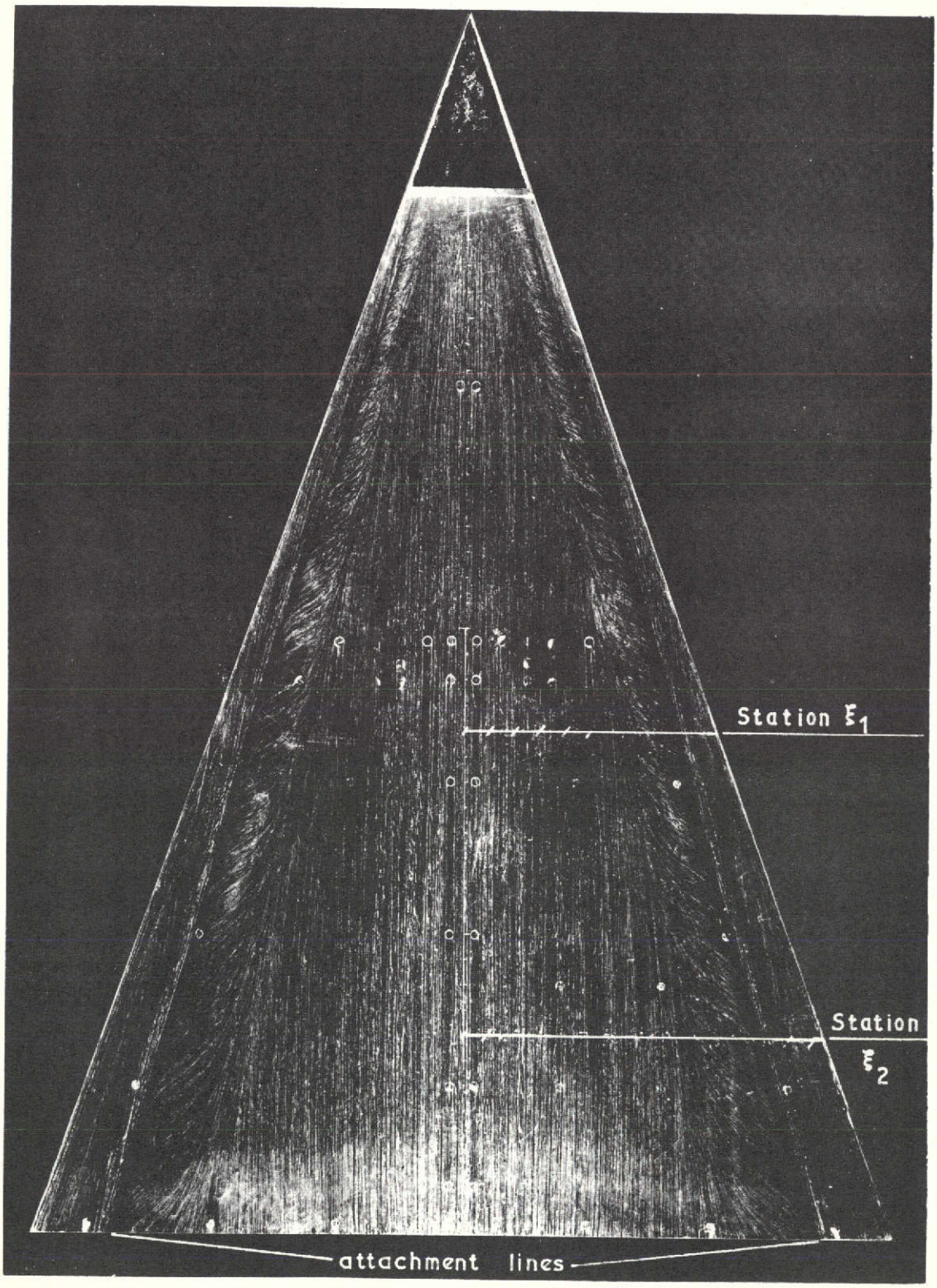

a. CLEAN WING

Figure 30. Oil Flow Patterns on Undeformed Wing at $\alpha = 5^\circ$ (Ref. 42)
(Sheet 1 of 2)

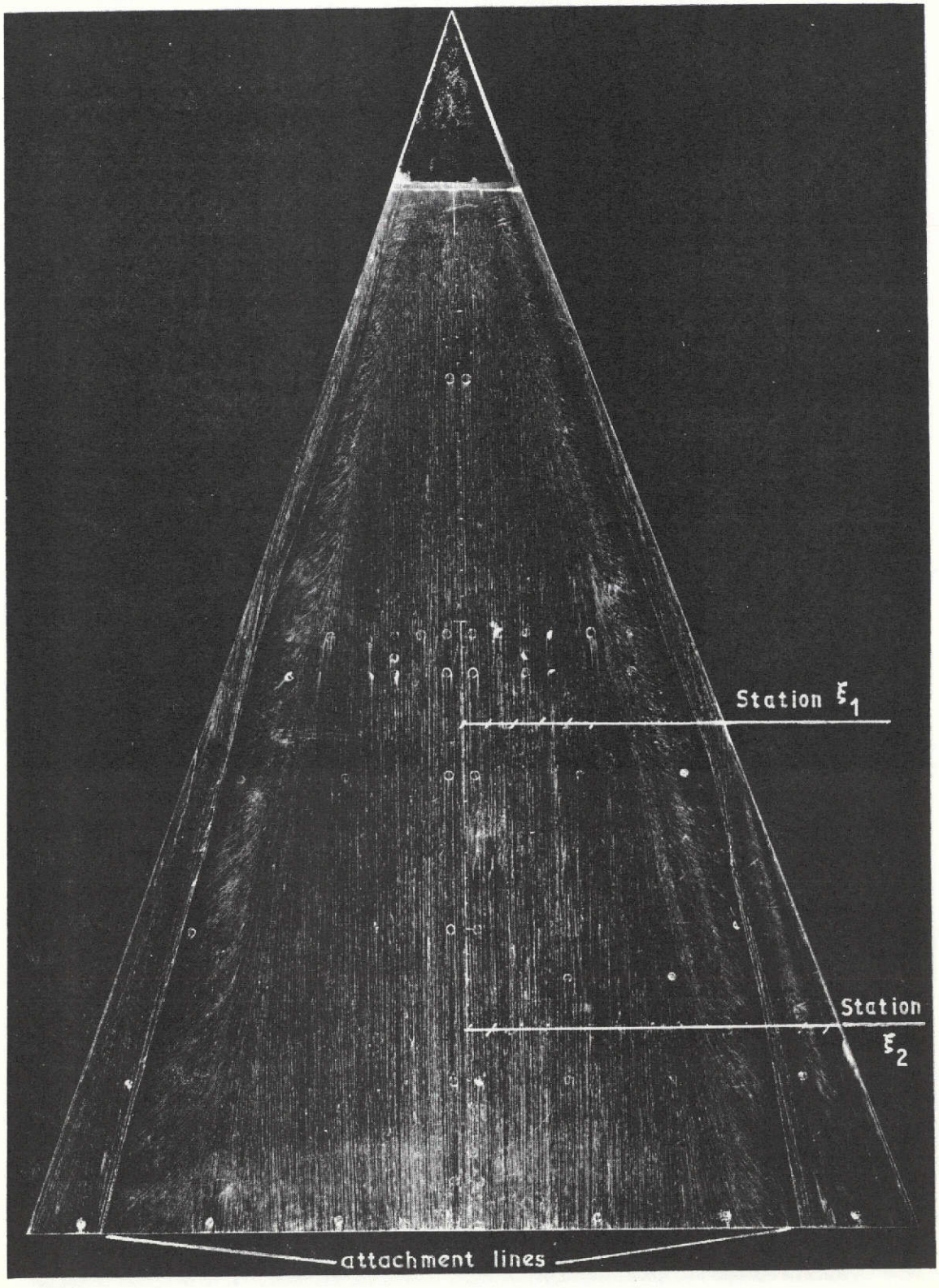

b. PRESSURE TRANSDUCER AT $\xi_1 = 0.583$, $\eta = 0.90$

Figure 30. Oil Flow Patterns on Undeformed Wing at $\alpha = 5^\circ$ (Ref. 42)
(Sheet 2 of 2)

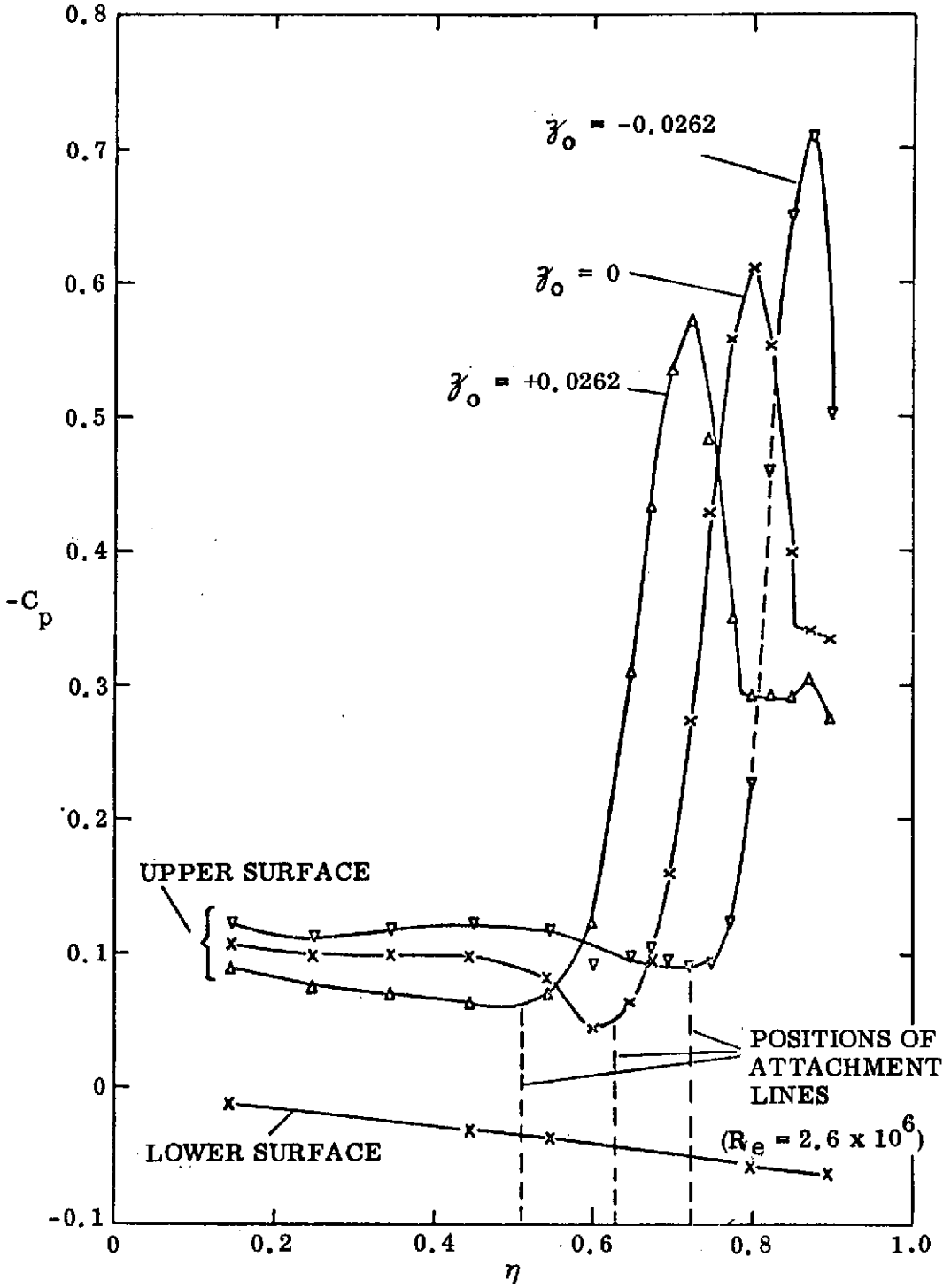

a. STATION ξ_1, R_e = 5.11 x 10^6

Figure 31. Spanwise Pressure Distribution for Steady Deformation (Ref. 42) (Sheet 1 of 2)

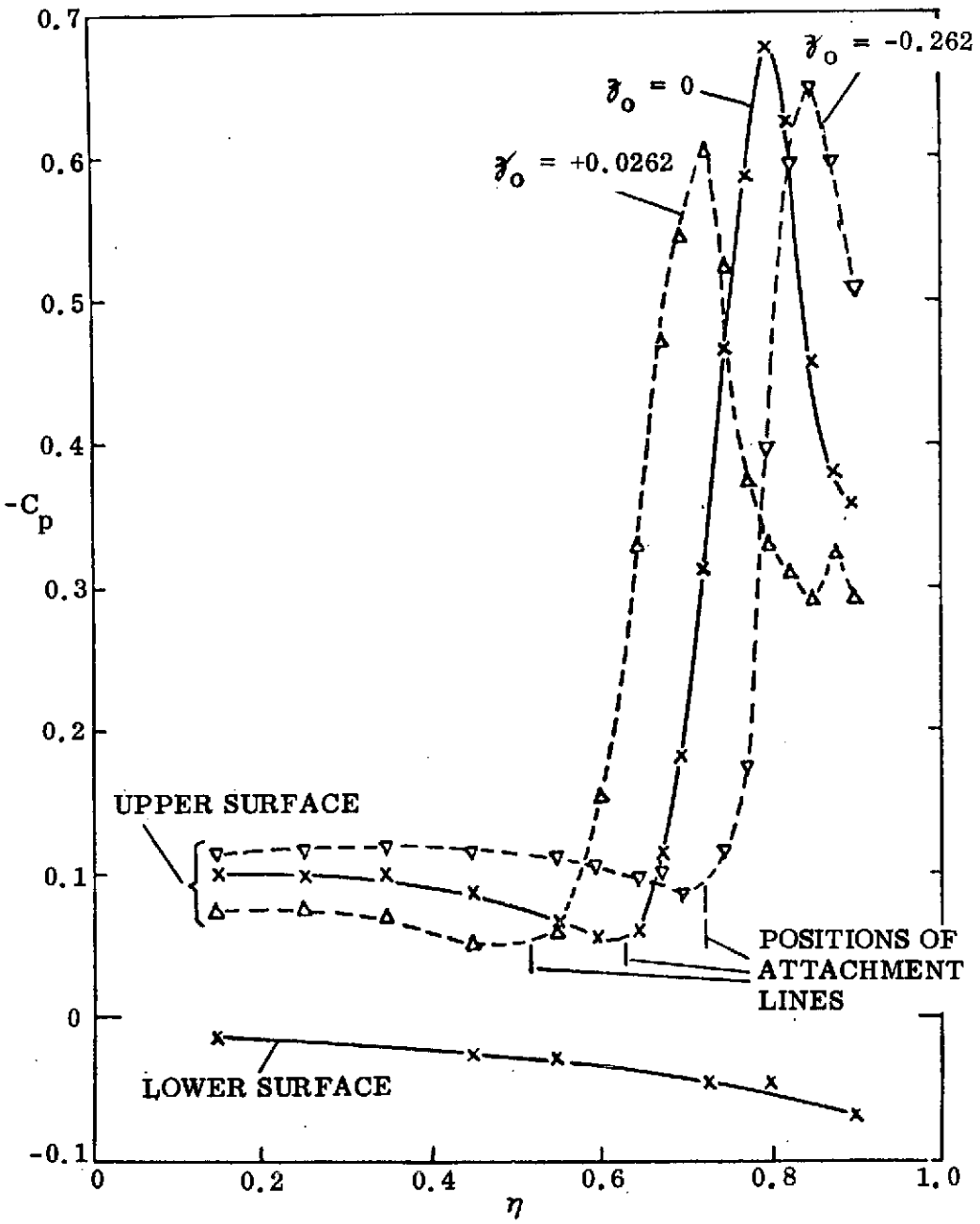

b. STATION ξ_1, $R_e = 2.56 \times 10^6$

Figure 31. Spanwise Pressure Distribution for Steady Deformation (Ref. 42) (Sheet 2 of 2)

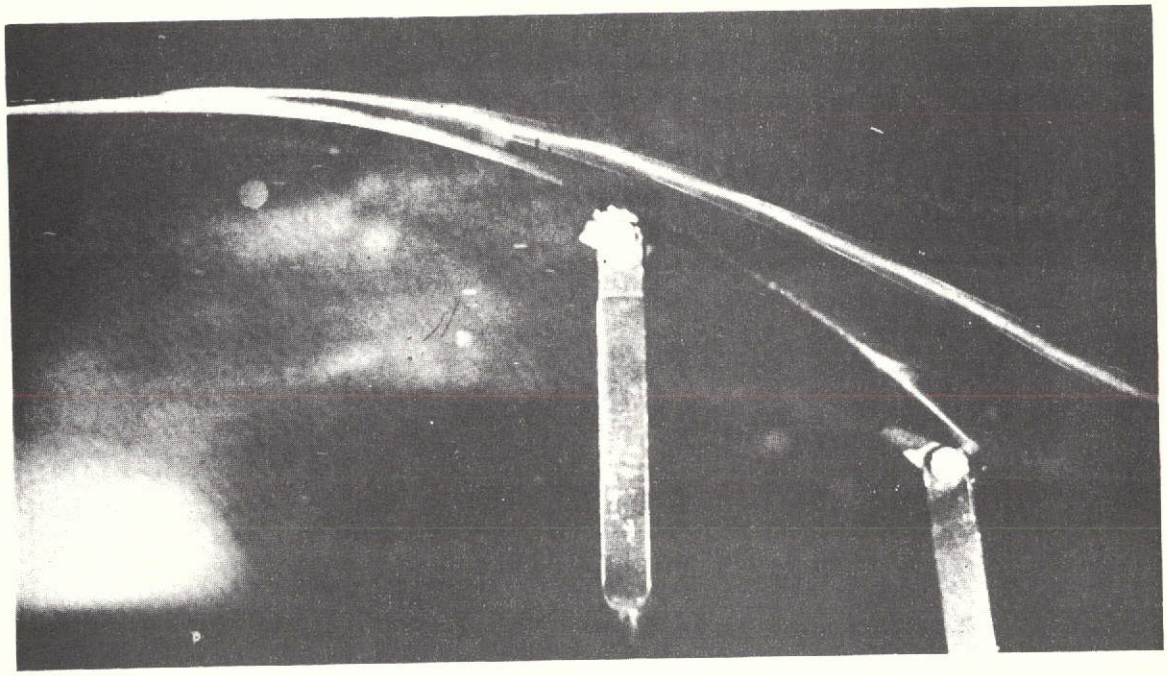

a. LOCAL INCIDENCE INCREASING WITH DISTANCE FROM APEX

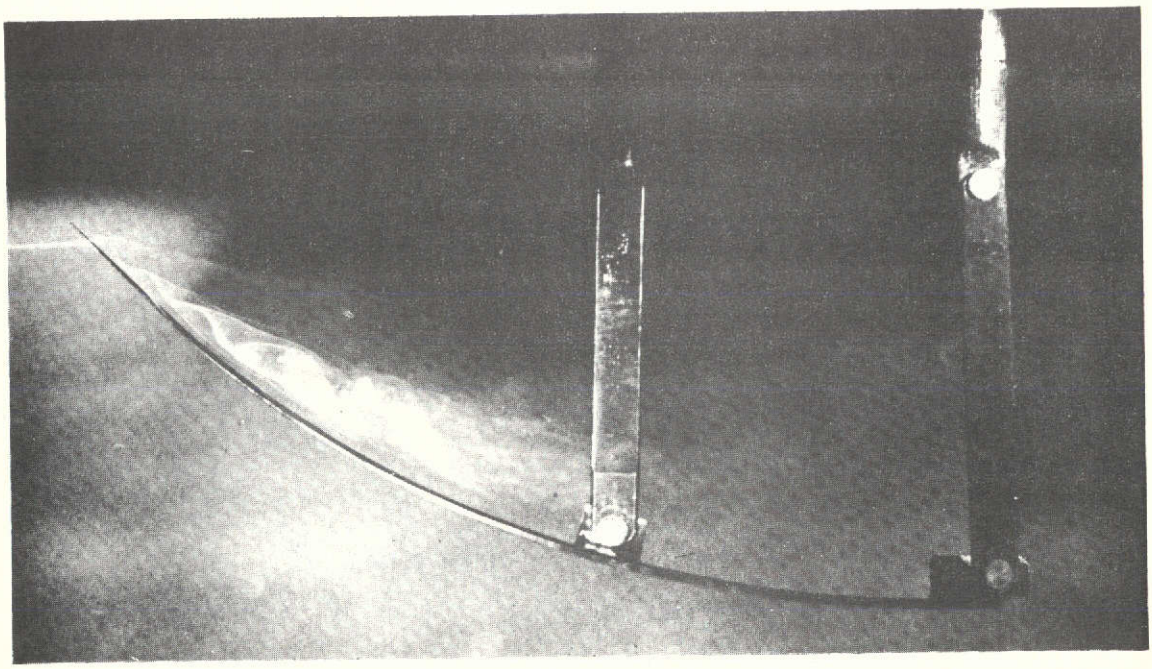

b. LOCAL INCIDENCE DECREASING WITH DISTANCE FROM APEX

Figure 32. Vortices for Cambered Delta Plate with 80° Leading Edge Sweep (Ref. 49)

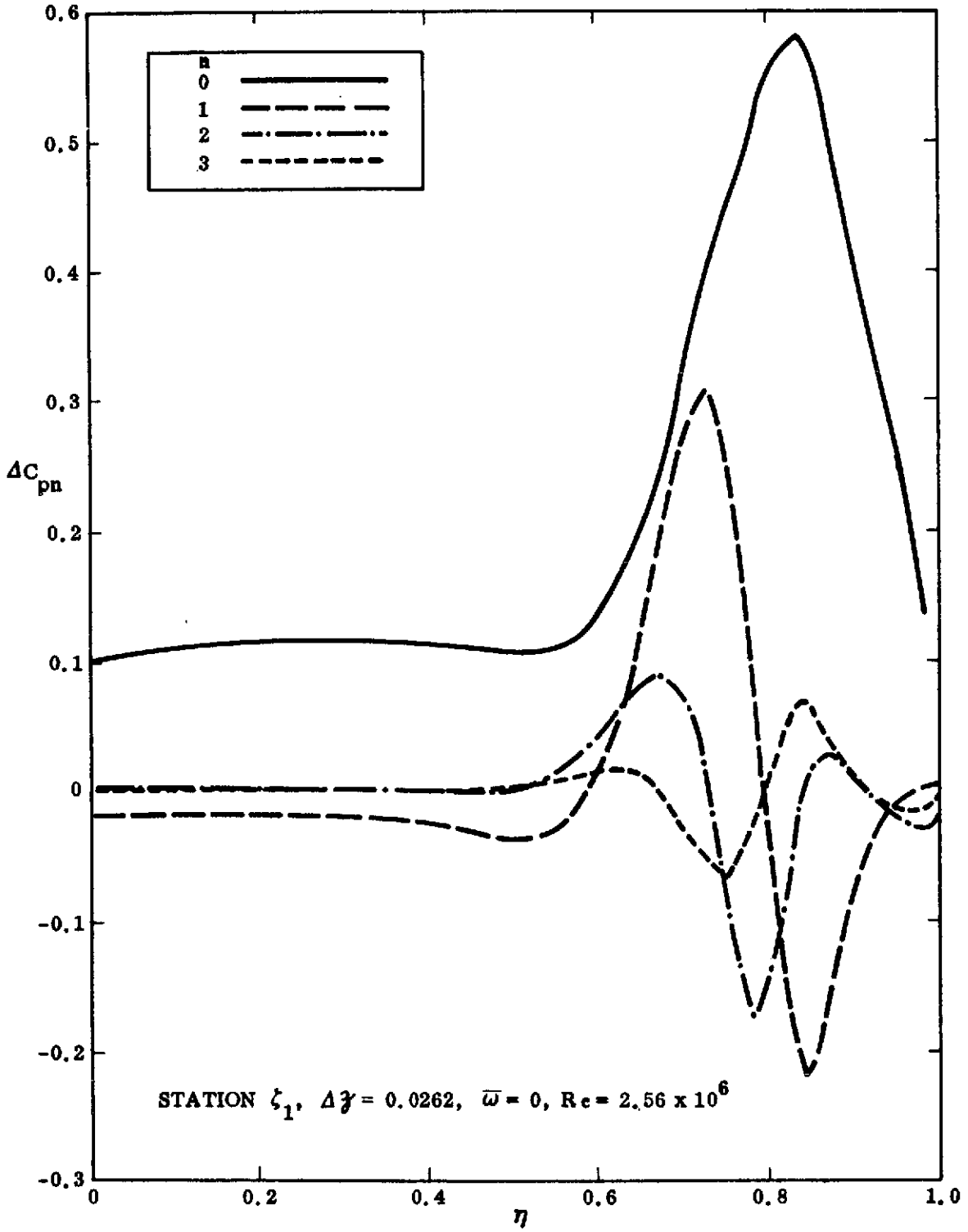

Figure 33. Spanwise Distributions of Harmonic Components for Quasi-steady Variation (Ref. 42)

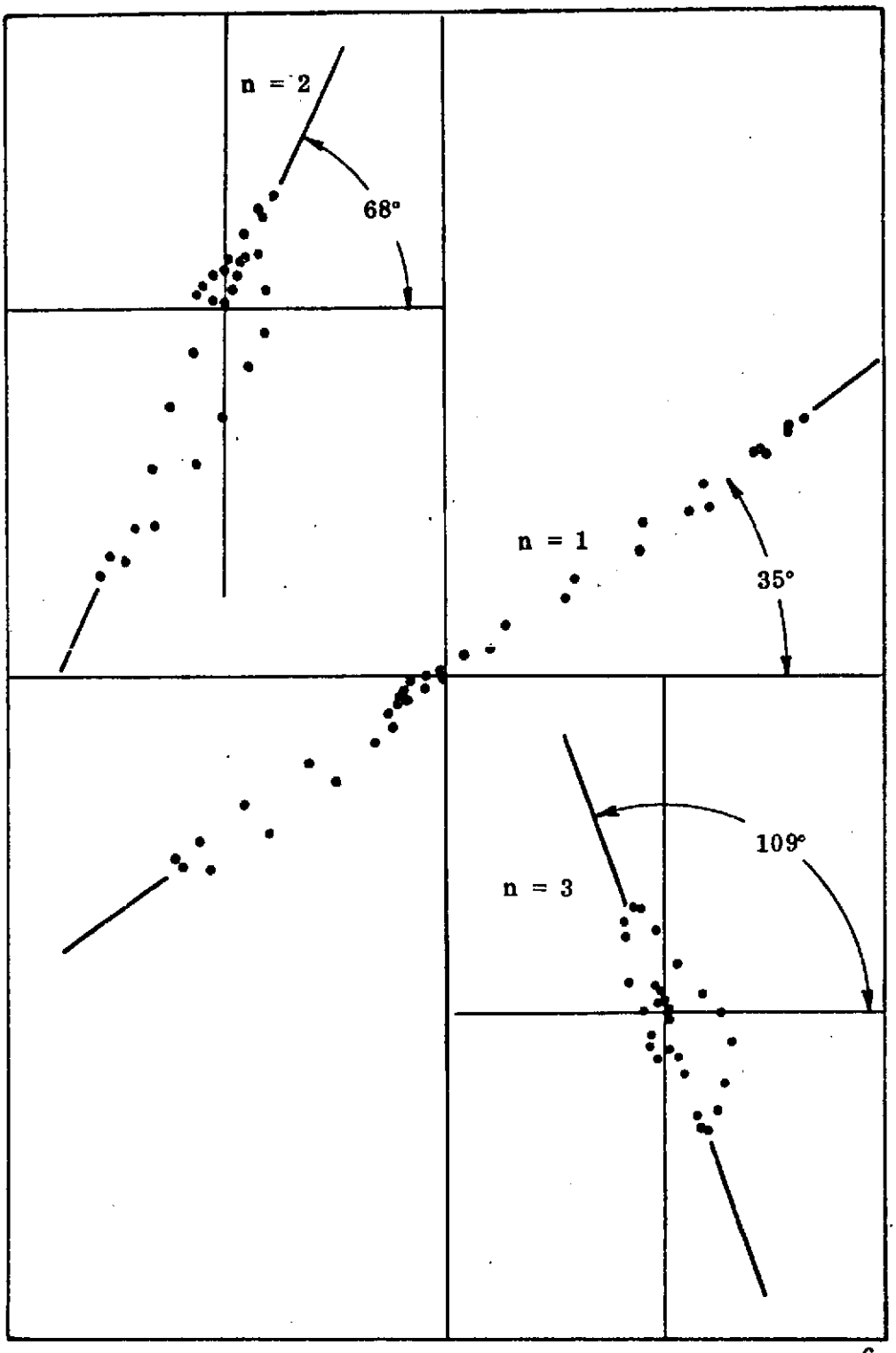

a. STATION ξ_1, $\Delta\bar{z} = 0.0262$, $\bar{\omega} = 1.0$, $Re = 2.56 \times 10^6$

Figure 34. Polar Diagrams of Amplitude - Phase Angle for Various Spanwise Positions (Ref. 42) (Sheet 1 of 2)

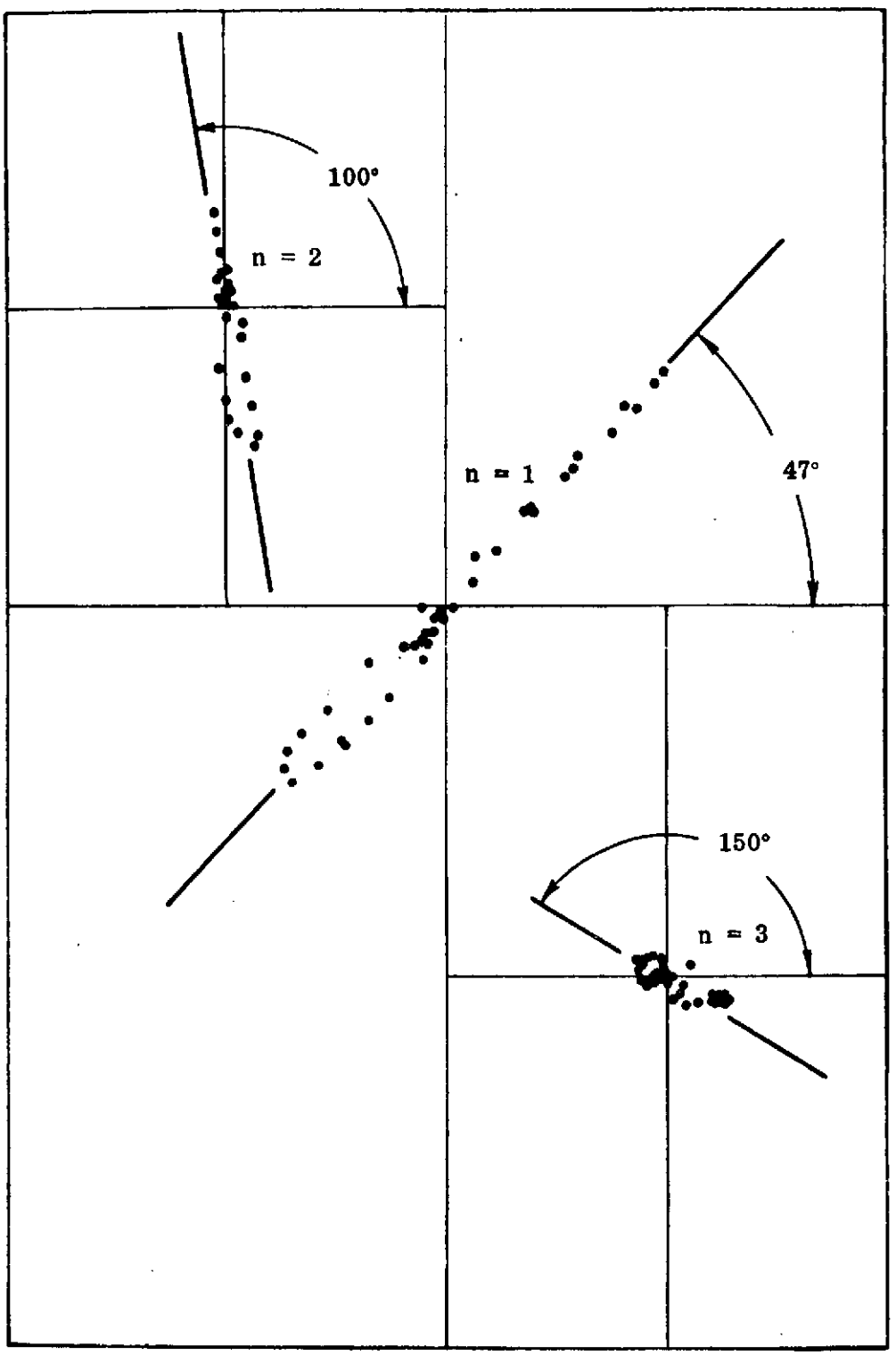

b. STATION ξ_2, $\Delta\zeta = 0.0262$, $\bar{\omega} = 1.0$, Re = 2.56×10^6

Figure 34. Polar Diagrams of Amplitude - Phase Angle for Various Spanwise Positions (Ref. 42) (Sheet 2 of 2)

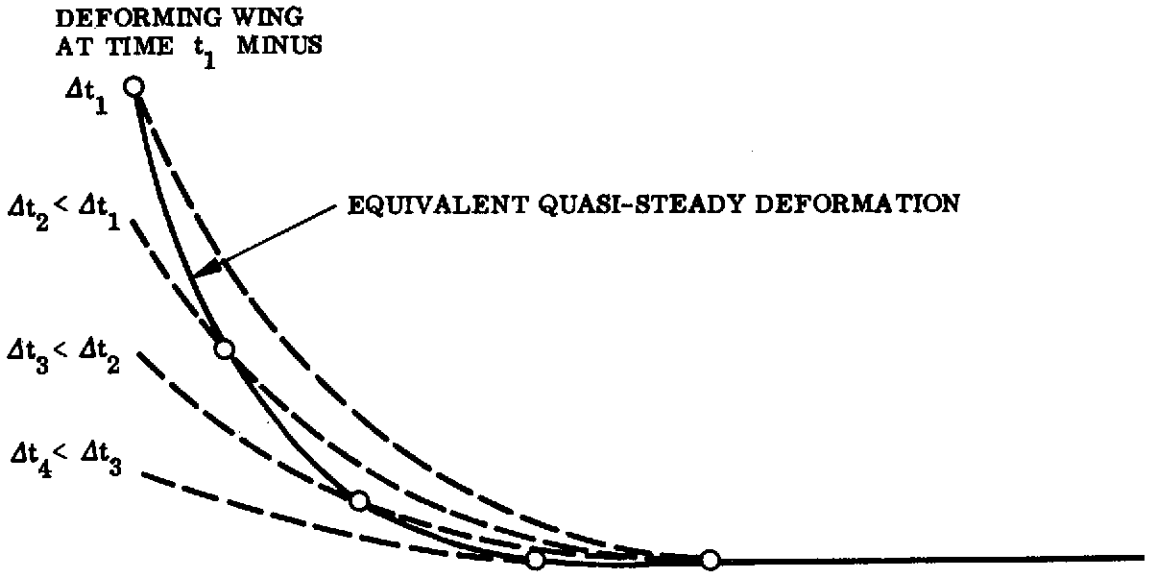

a. BENDING WING

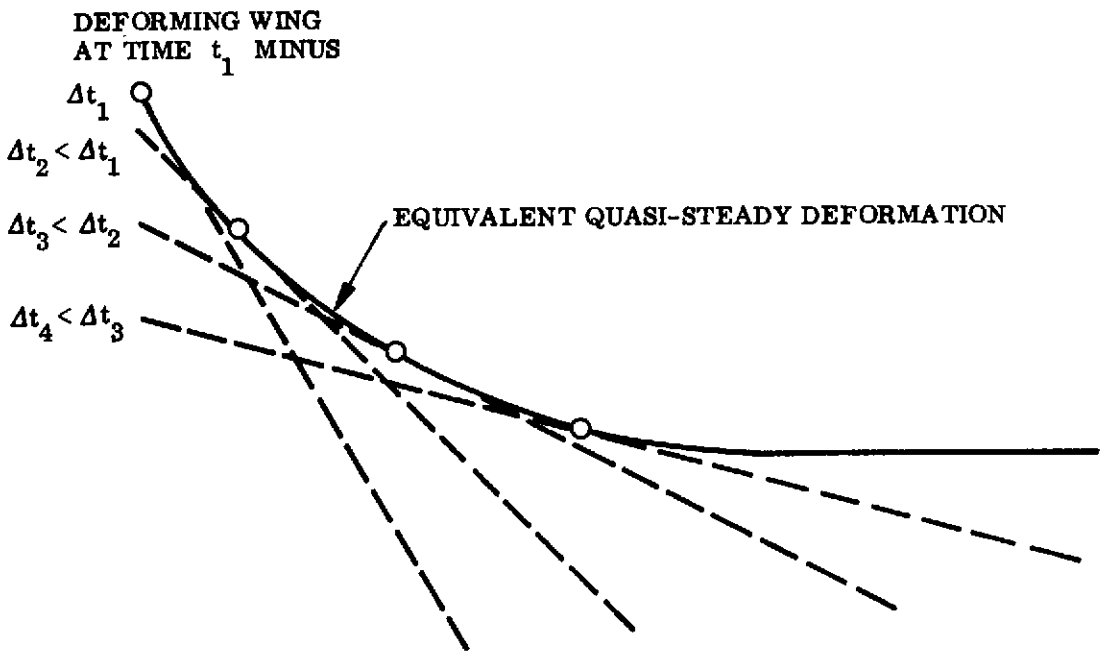

b. PLUNGING WING

Figure 35. Deformation Shapes for Vortex Build-Up in Steady and Unsteady Case

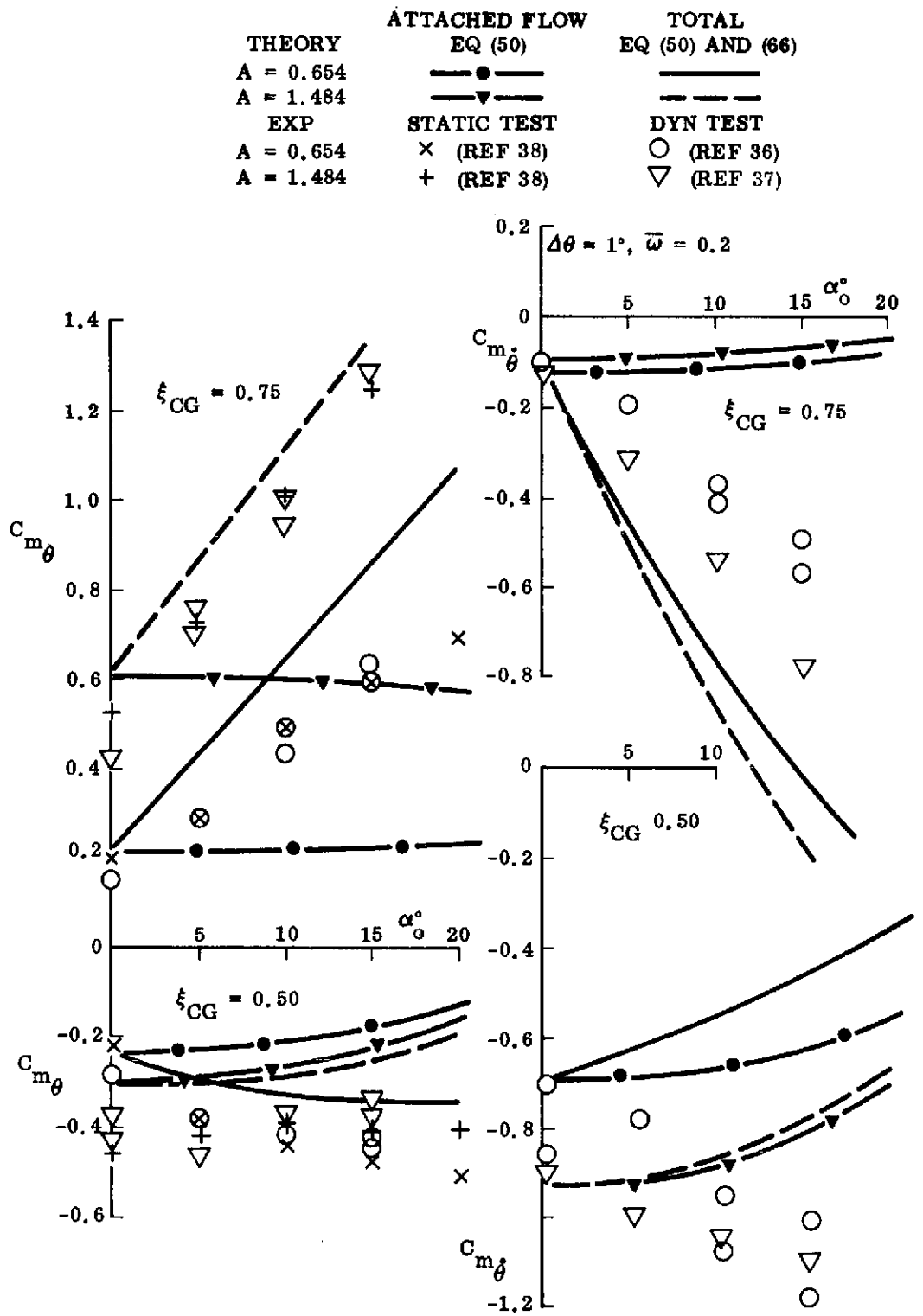

Figure 36. Pitch Stability Derivatives for Sharp-Edged Delta Wings at M = 0

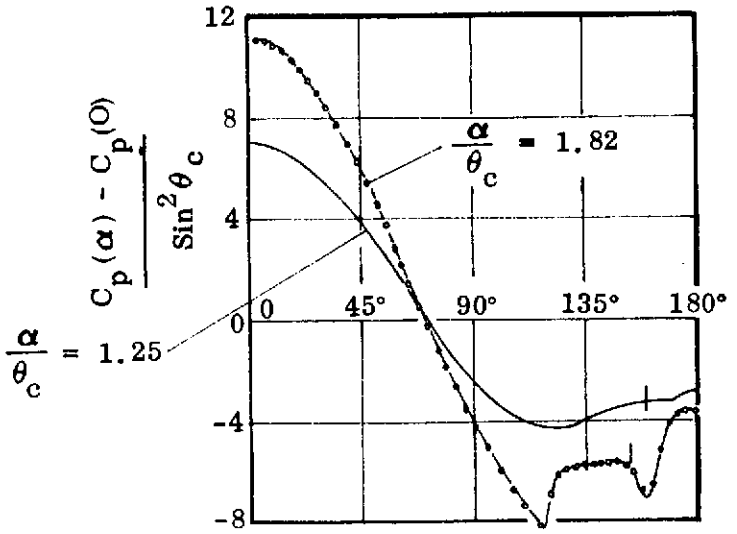

a. CIRCUMFERENTIAL PRESSURE DISTRIBUTIONS

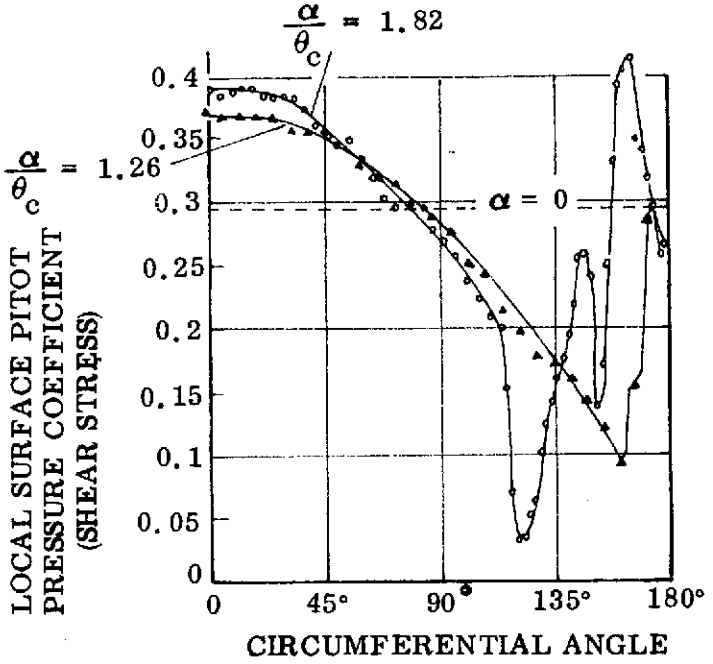

b. SURFACE SHEAR STRESS DISTRIBUTIONS AROUND CONE

Figure 37. Free Body Vortex Effects on a 12.5° Sharp Cone (Ref. 53)

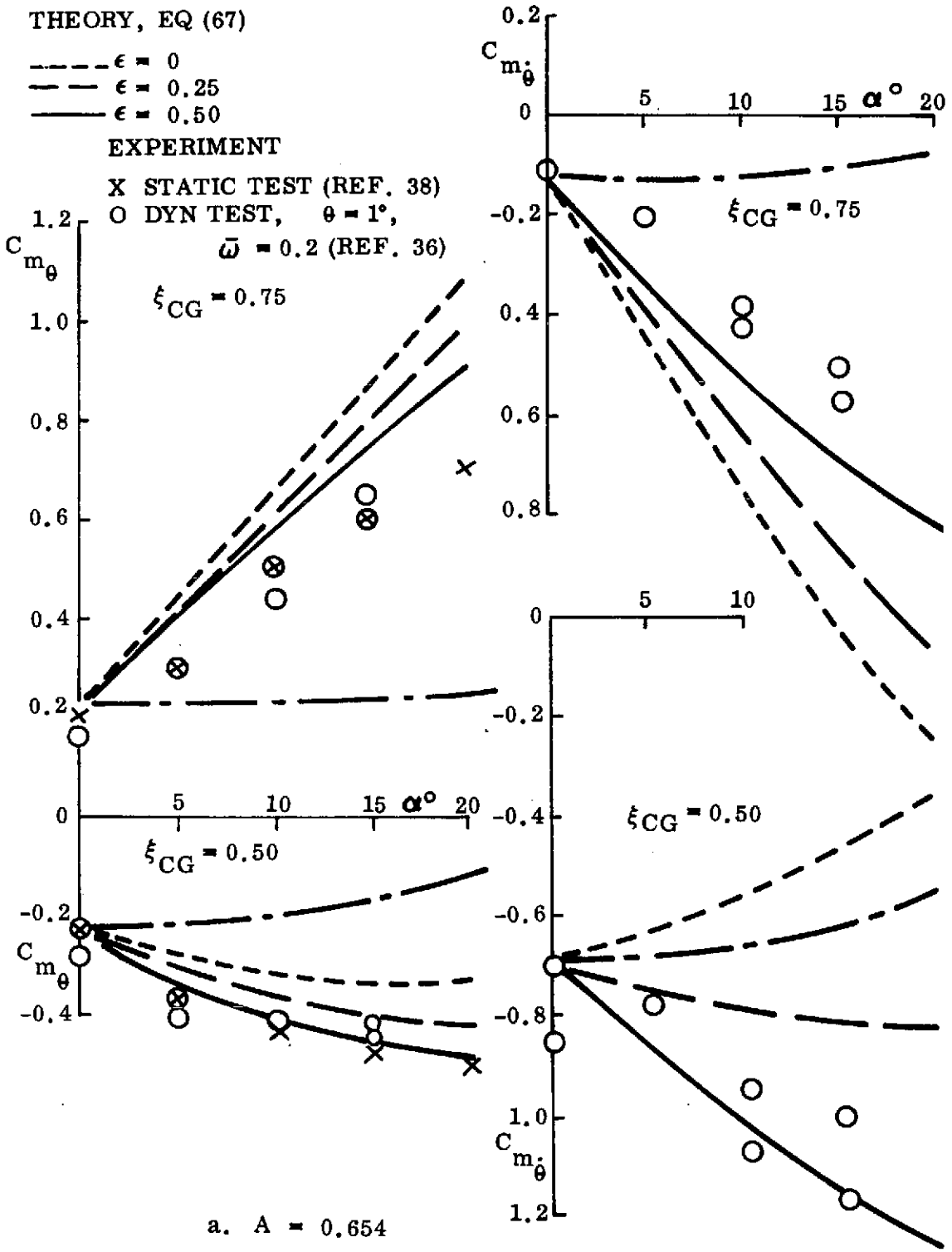

Figure 38. Pitch Oscillation Derivatives for Sharp-Edged Delta Wings
(Sheet 1 of 2)

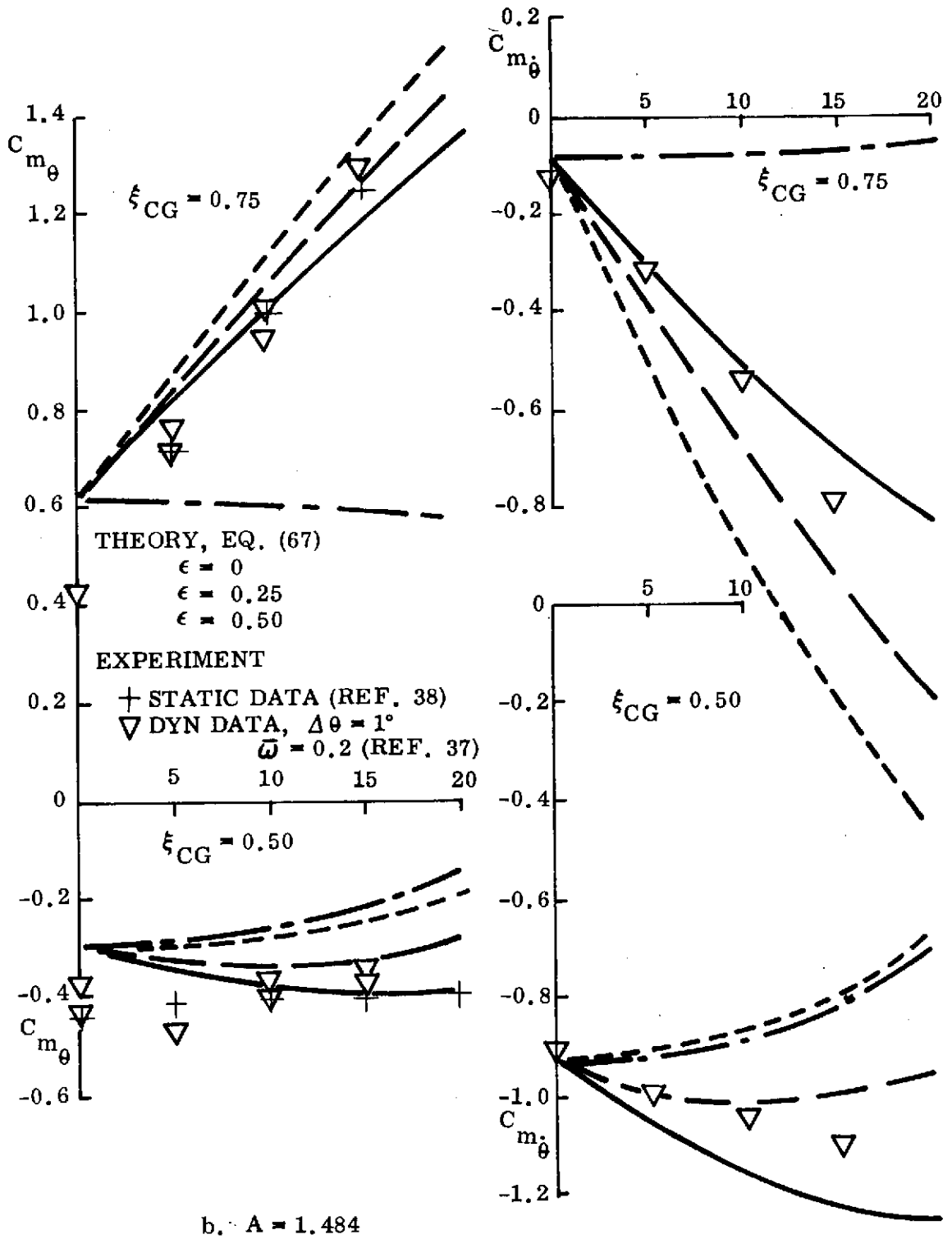

Figure 38. Pitch Oscillation Derivatives for Sharp-Edged Delta Wings (Sheet 2 of 2)

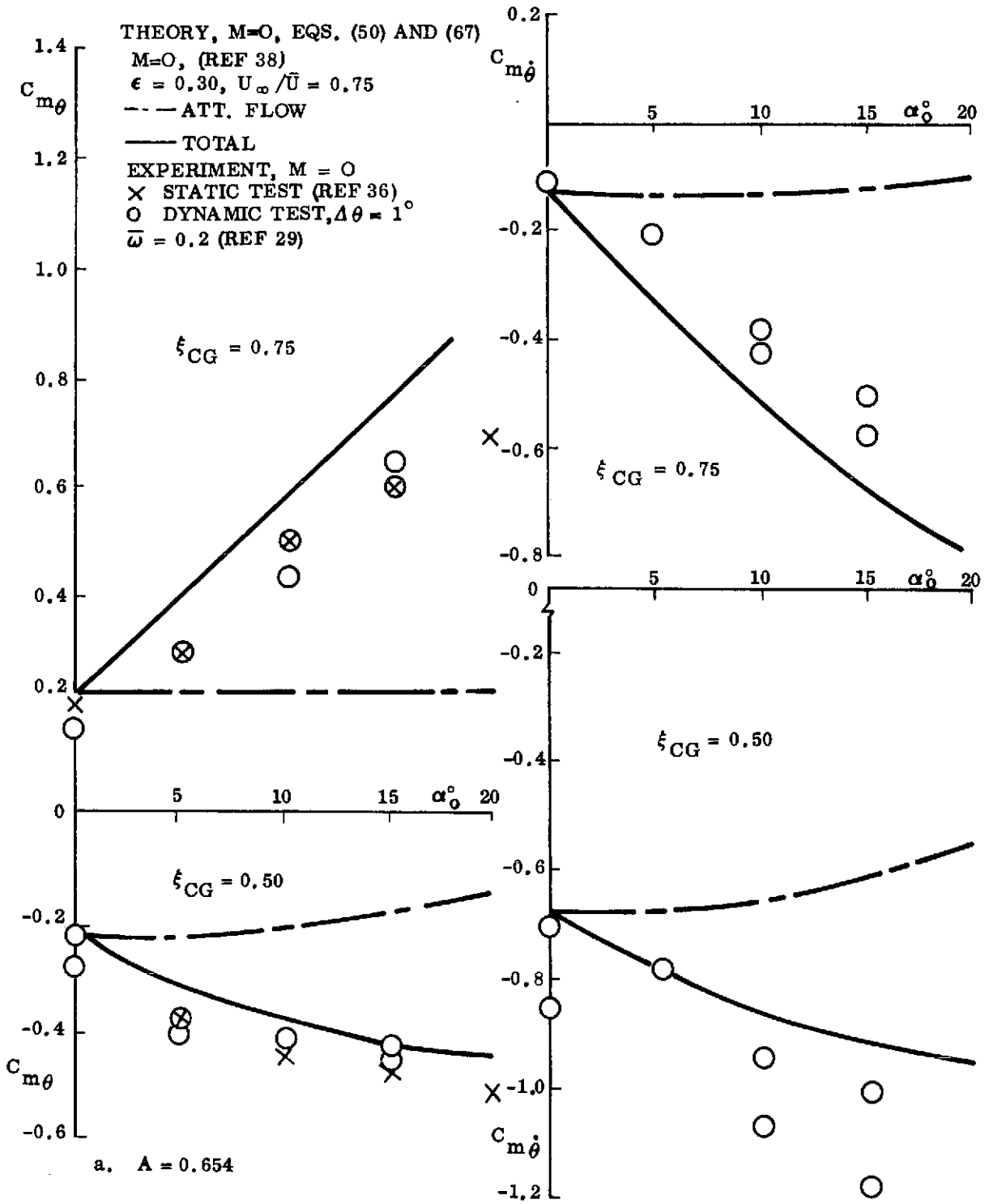

Figure 39. Dynamic Stability Derivatives for Sharp-Edged Delta Wings
(Sheet 1 of 2)

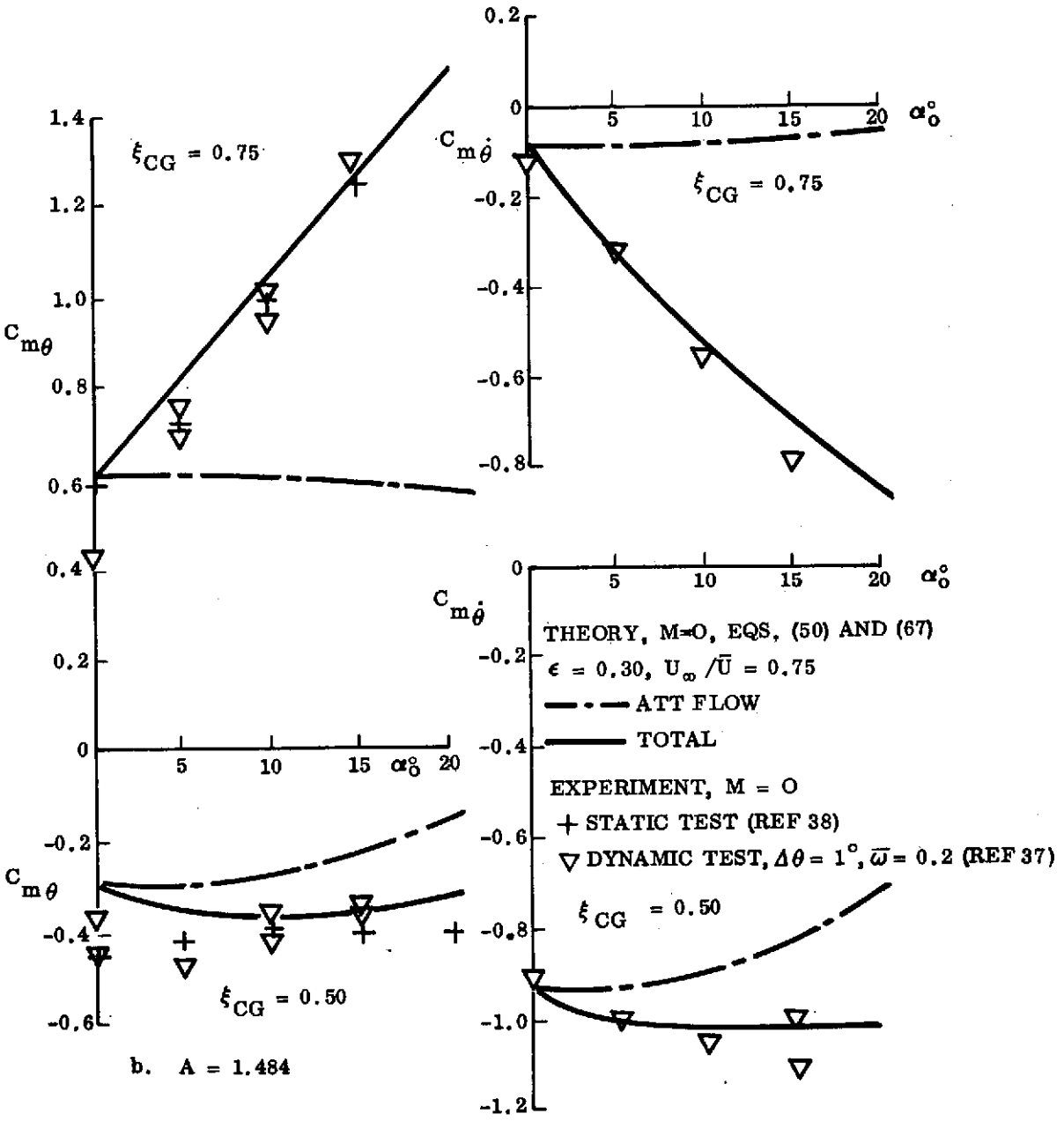

b. A = 1.484

Figure 39. Dynamic Stability Derivatives for Sharp-Edged Delta Wings
(Sheet 2 of 2)

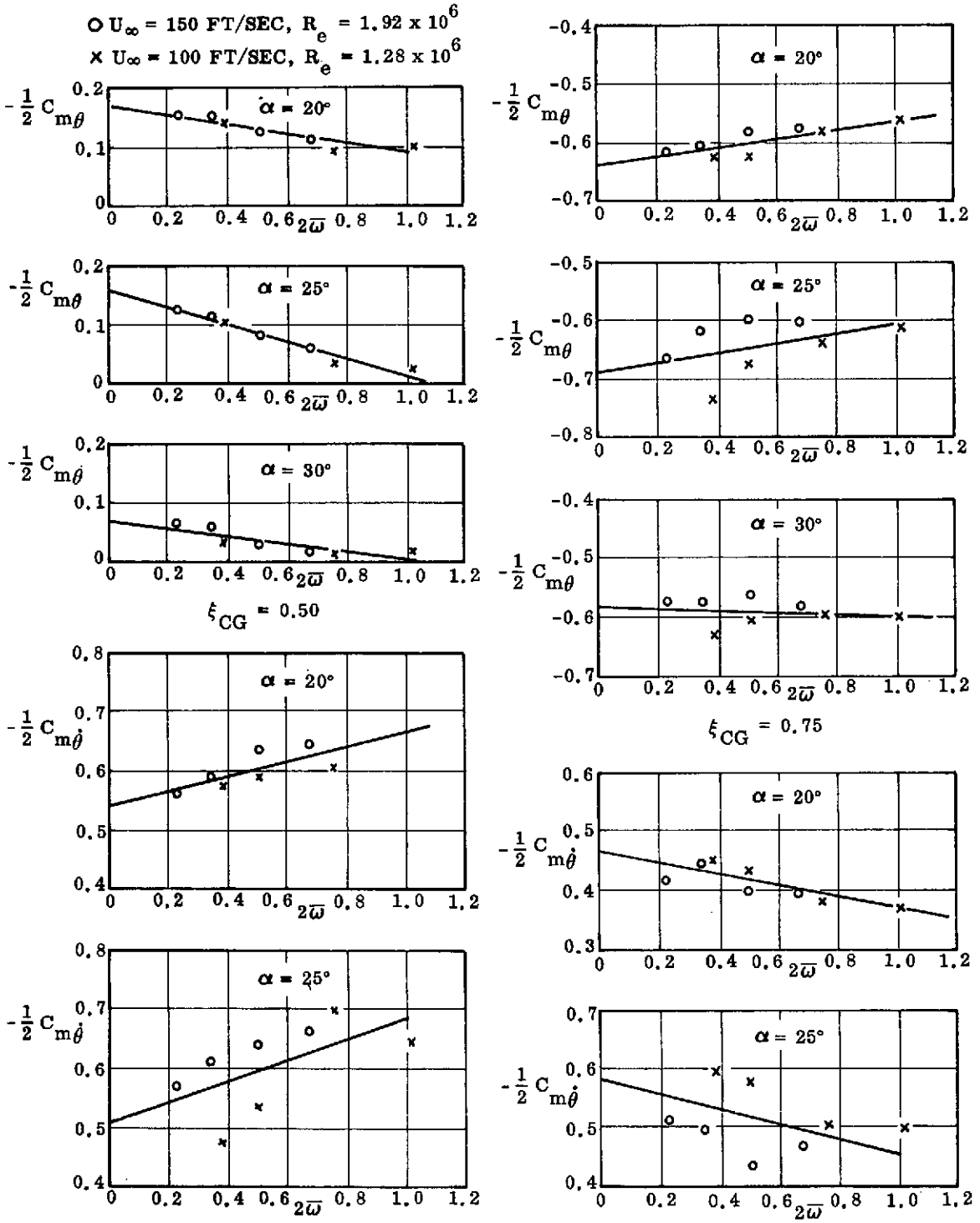

a. C_{m_θ} AND $C_{m_{\dot\theta}}$ AS FUNCTIONS OF REDUCED FREQUENCY

Figure 40. Frequency Effects on Dynamic Derivatives for 1° Pitch Oscillations (Ref. 57) (Sheet 1 of 2)

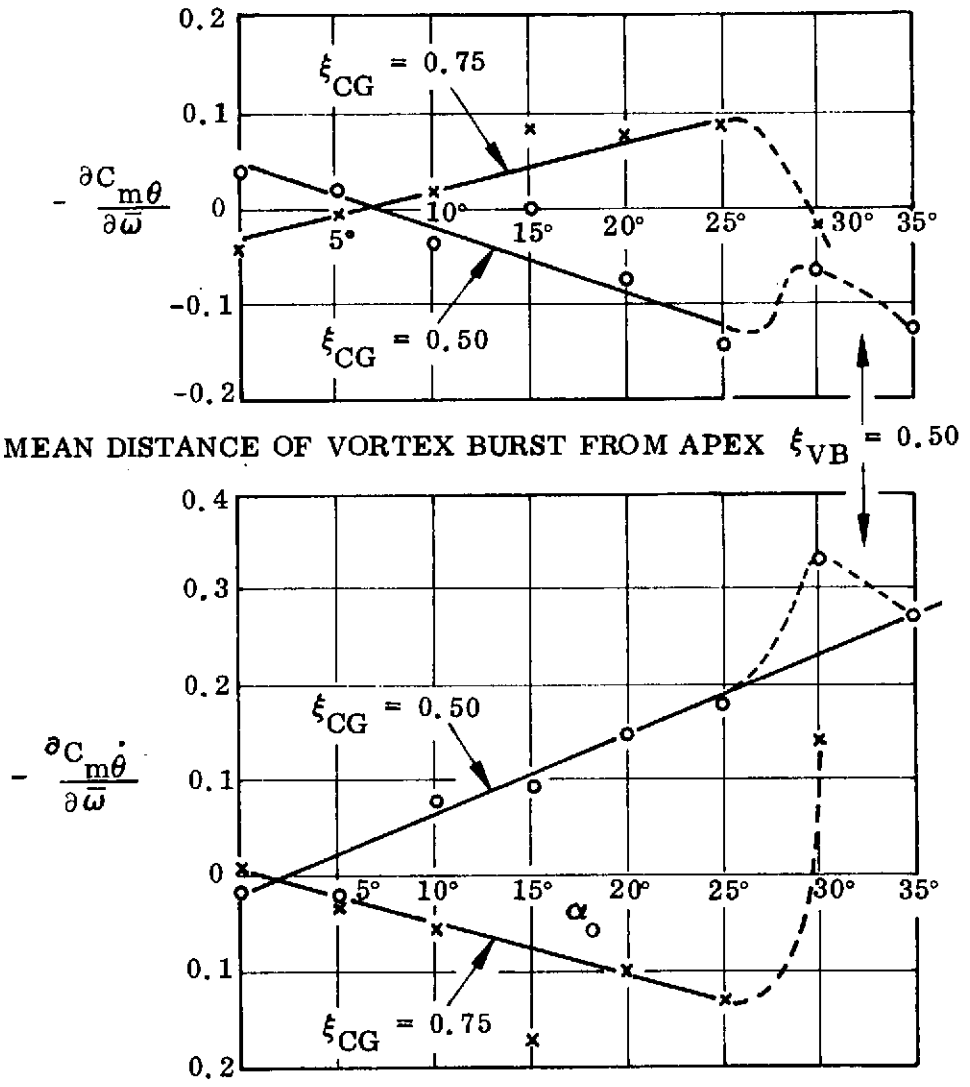

b. $\partial C_{m_\theta} / \partial \bar{\omega}$ AND $\partial C_{m_{\dot{\theta}}} / \partial \bar{\omega}$ VERSUS α_o

Figure 40. Frequency Effects on Dynamic Derivatives for 1° Pitch Oscillations (Ref. 57) (Sheet 2 of 2)

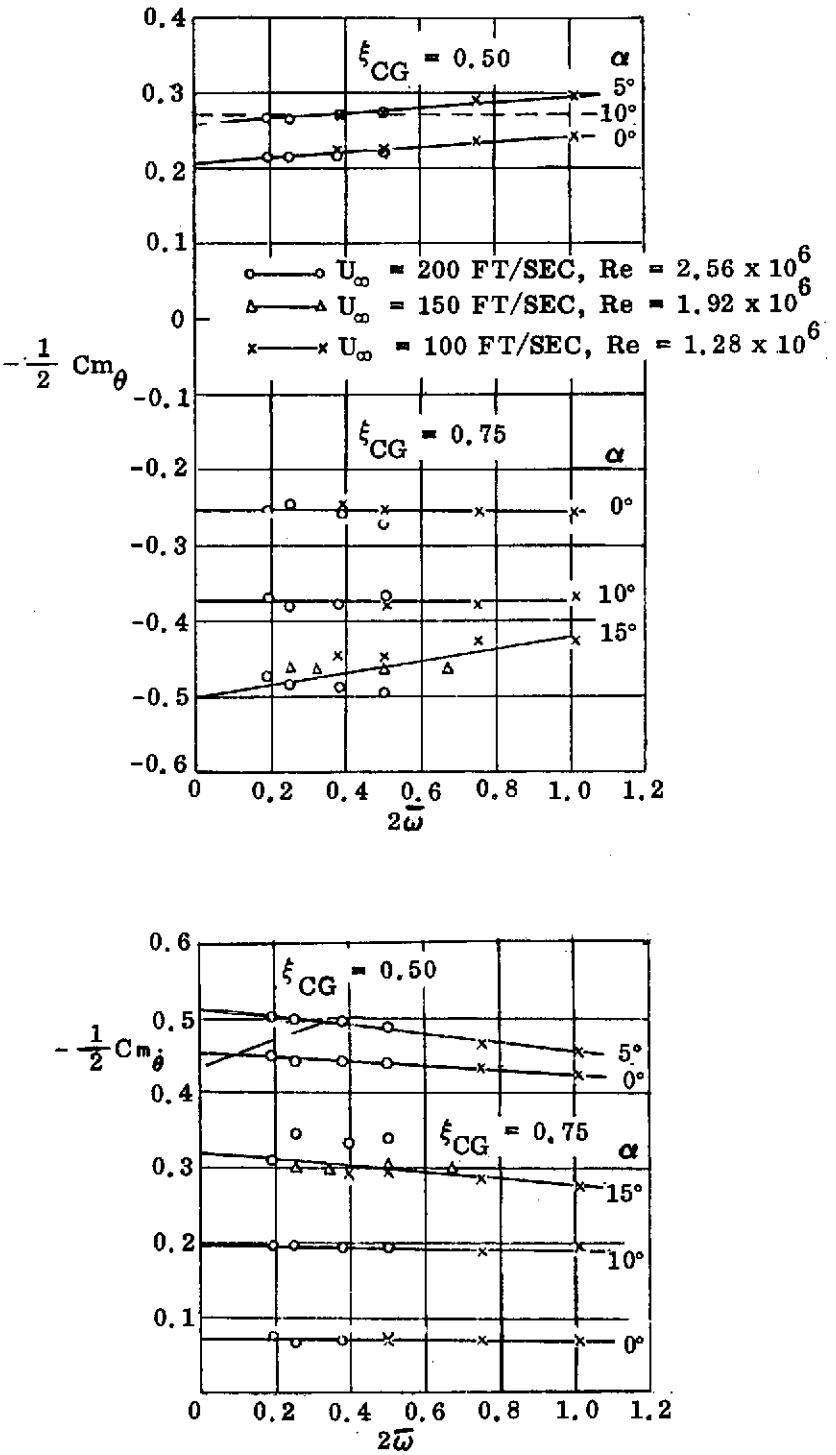

Figure 41. Frequency Effects on an A = 0.654 Delta Wing (Ref. 36)

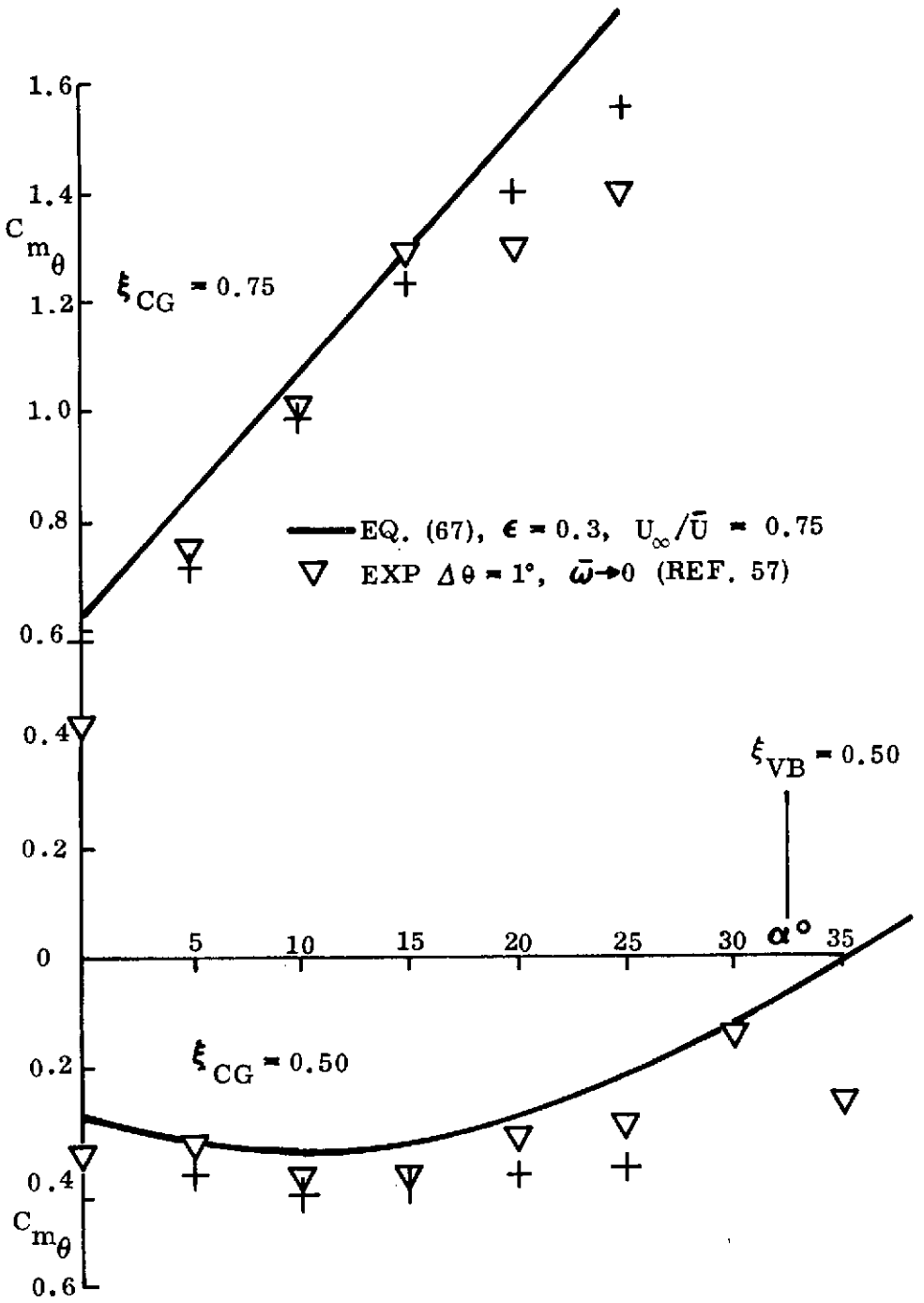

Figure 42. Effect of Vortex Burst on the Pitch Stability Derivatives of an A = 1.484 Delta Wing (Sheet 1 of 2)

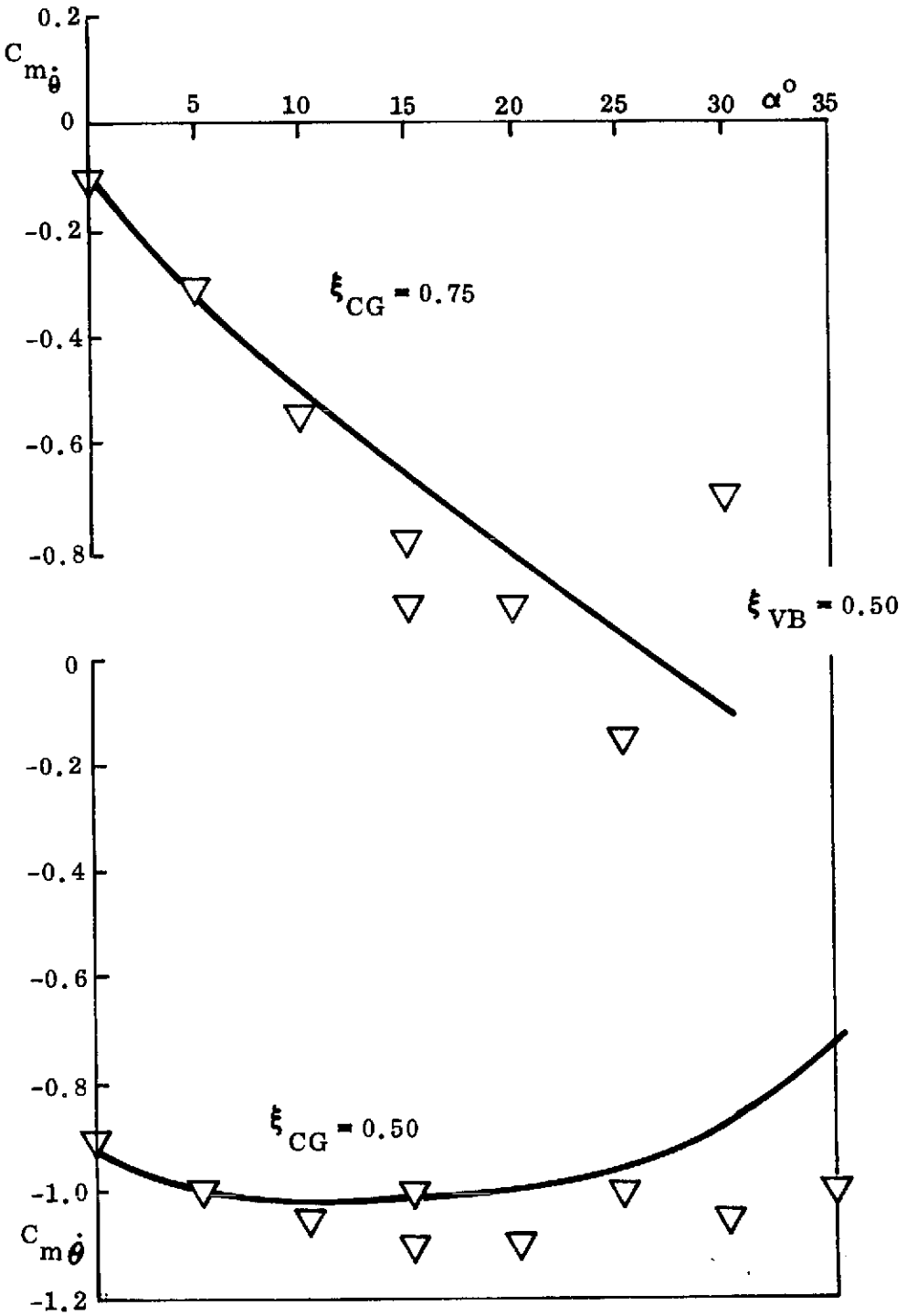

Figure 42. Effect of Vortex Burst on the Pitch Stability Derivatives of an A = 1.484 Delta Wing (Sheet 2 of 2)

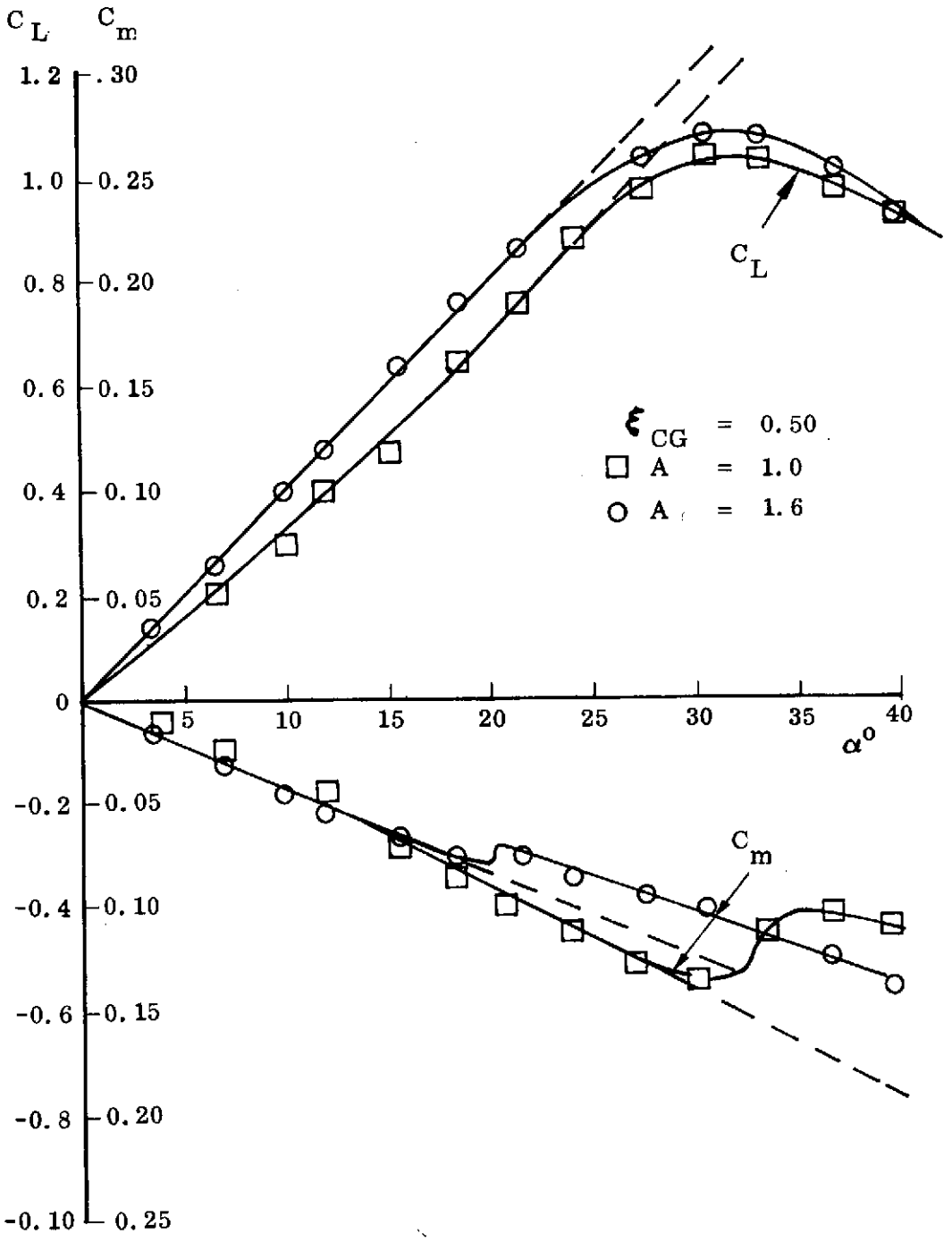

Figure 43. Effect of Vortex Burst on Static Longitudinal Characteristics of Sharp-Edged Delta Wings (Ref. 60)

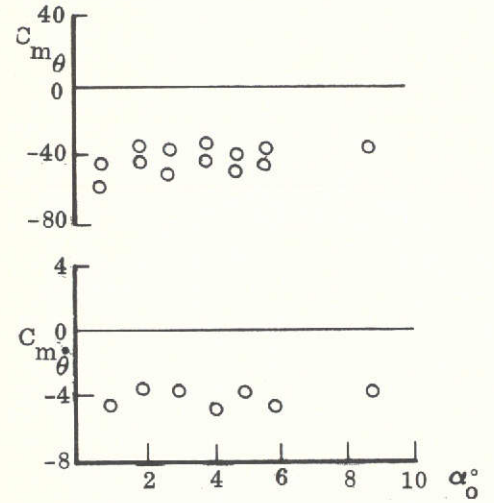

b. PITCH STABILITY DERIVATES FOR $\Delta\theta = 1°$, $\bar\omega^2 \ll 1$

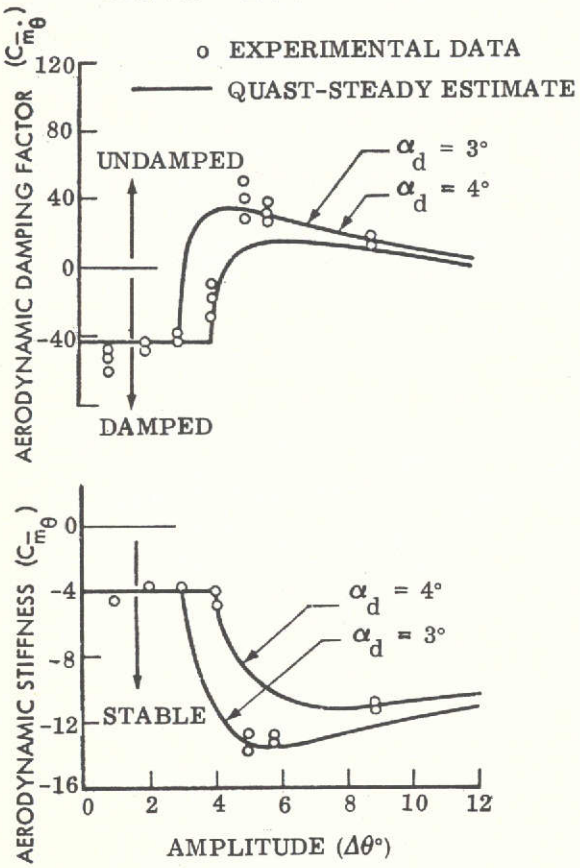

c. EFFECTIVE AERODYNAMIC STIFFNESS AND DAMPING FOR $\alpha_o = 0, \bar\omega^2 \ll 1$

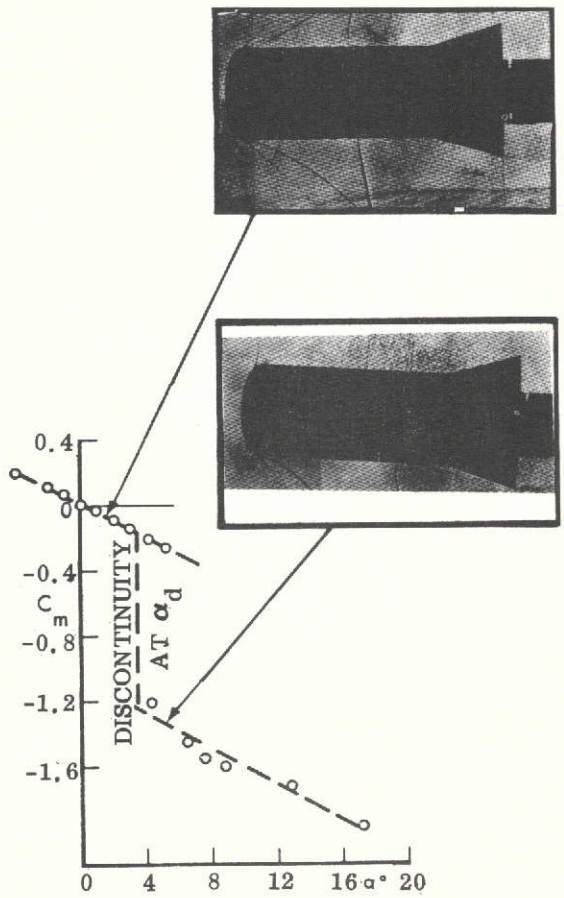

a. STATIC CHARACTERISTICS

Figure 44. Nonlinear Pitch Stability Characteristics of a Blunt Cylinder-Flare Body at M = 1.05 (Ref. 61)

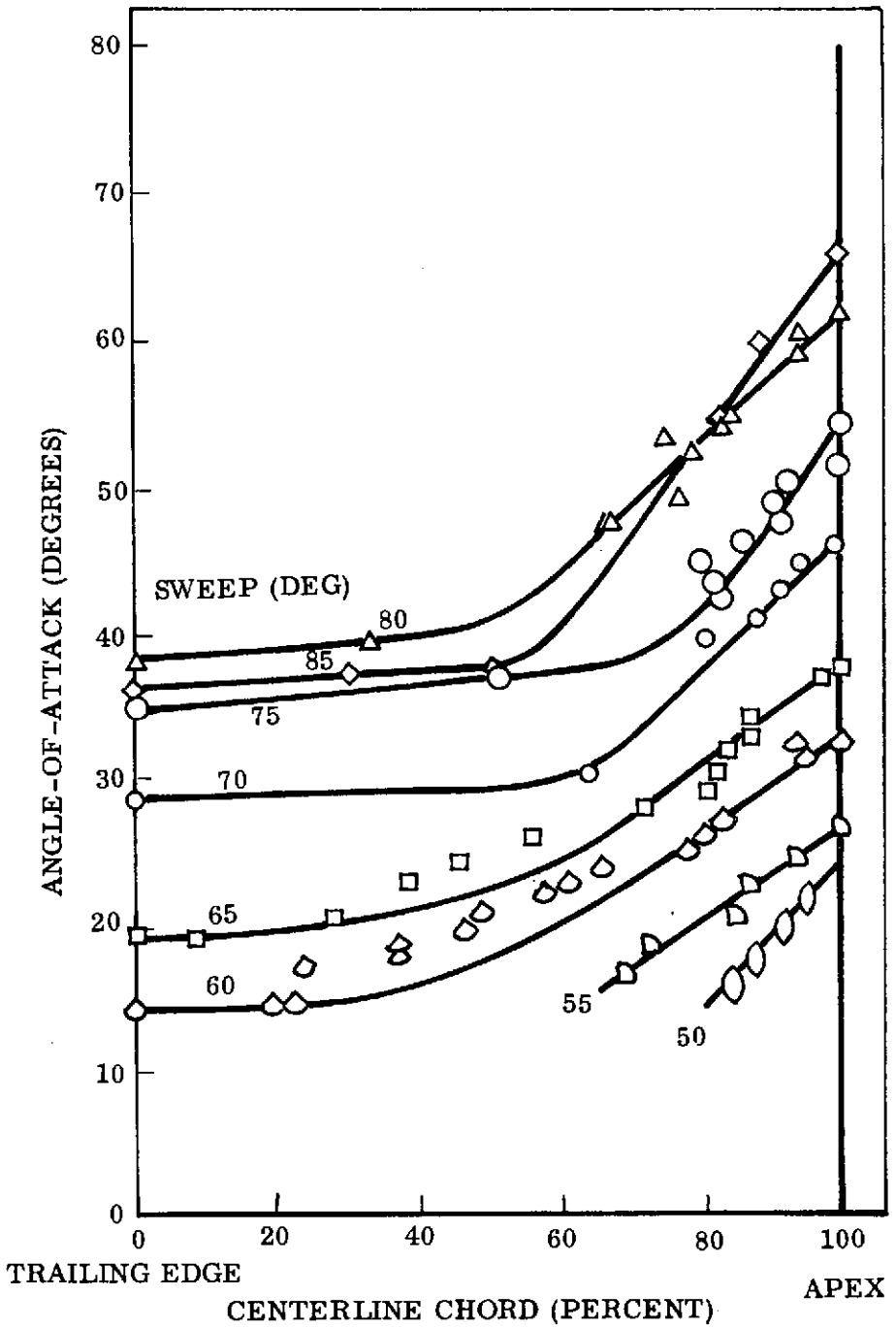

Figure 45. Vortex Burst Position on Sharp-Edged Delta Wings (Ref. 66)

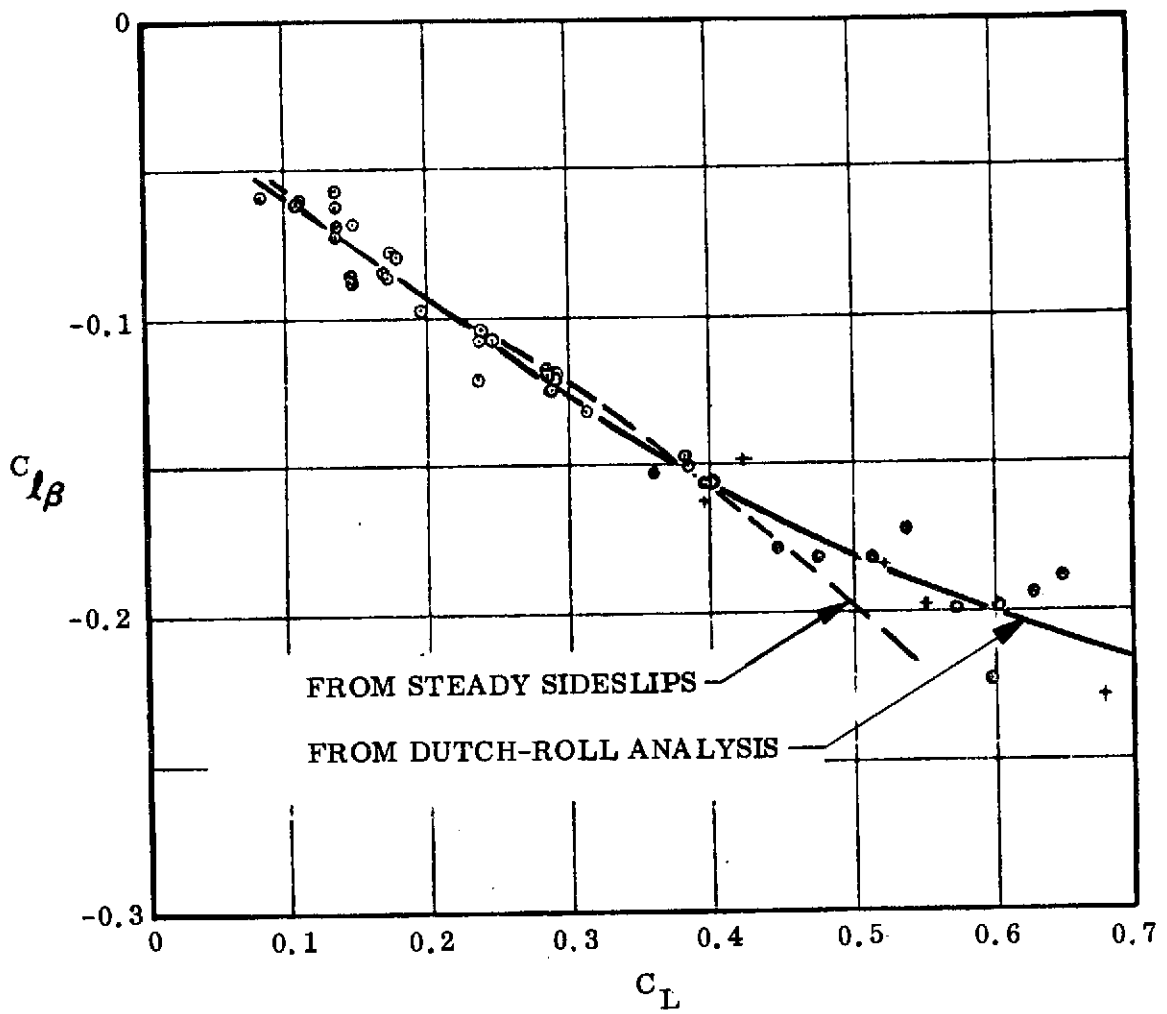

Figure 46. Flight Test Data for C_{l_β} of the Handley Page-115 (Ref. 71)

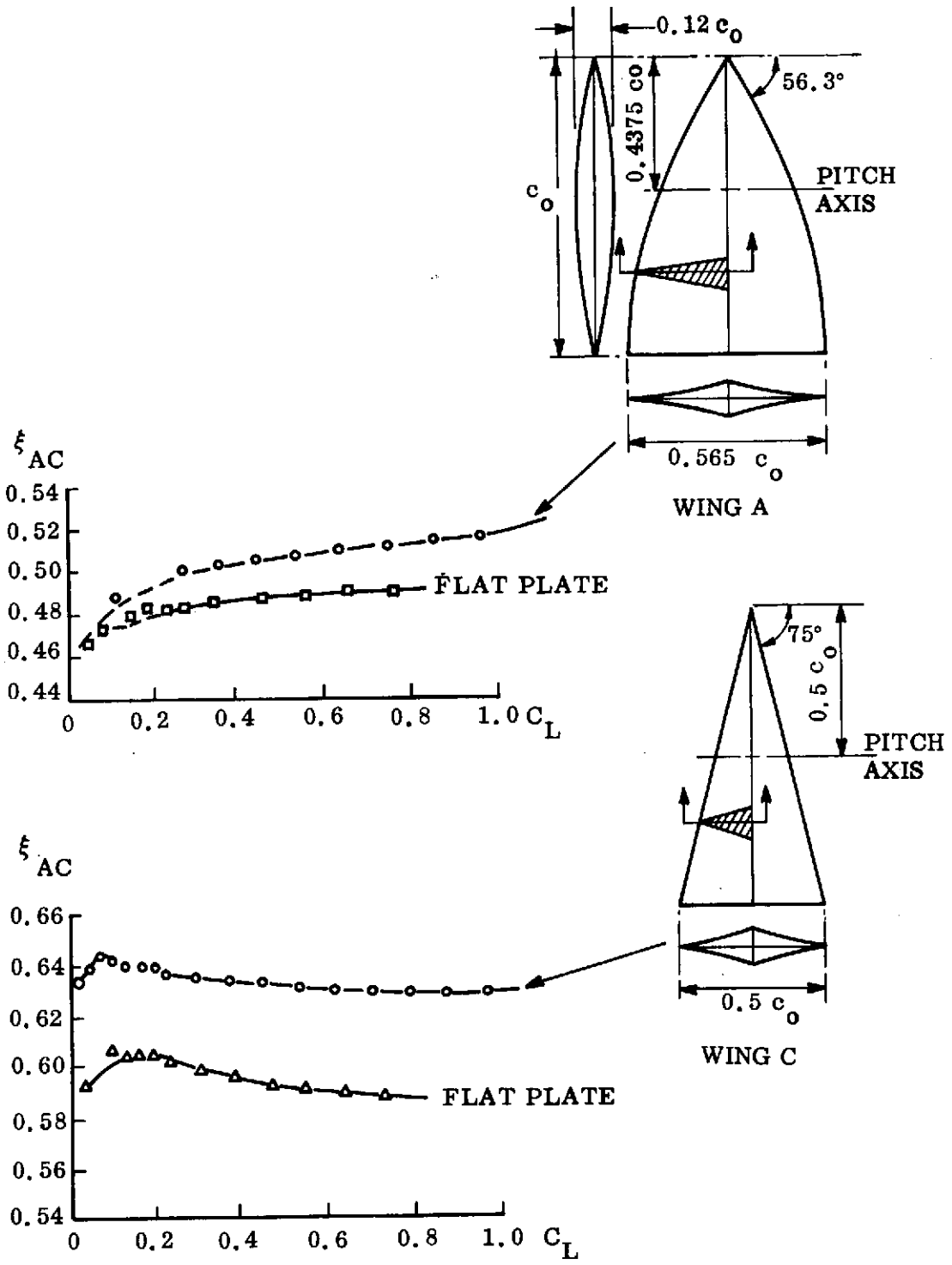

Figure 47. Center of Pressure of A = 1 Gothic and Delta Wings (Ref. 7)

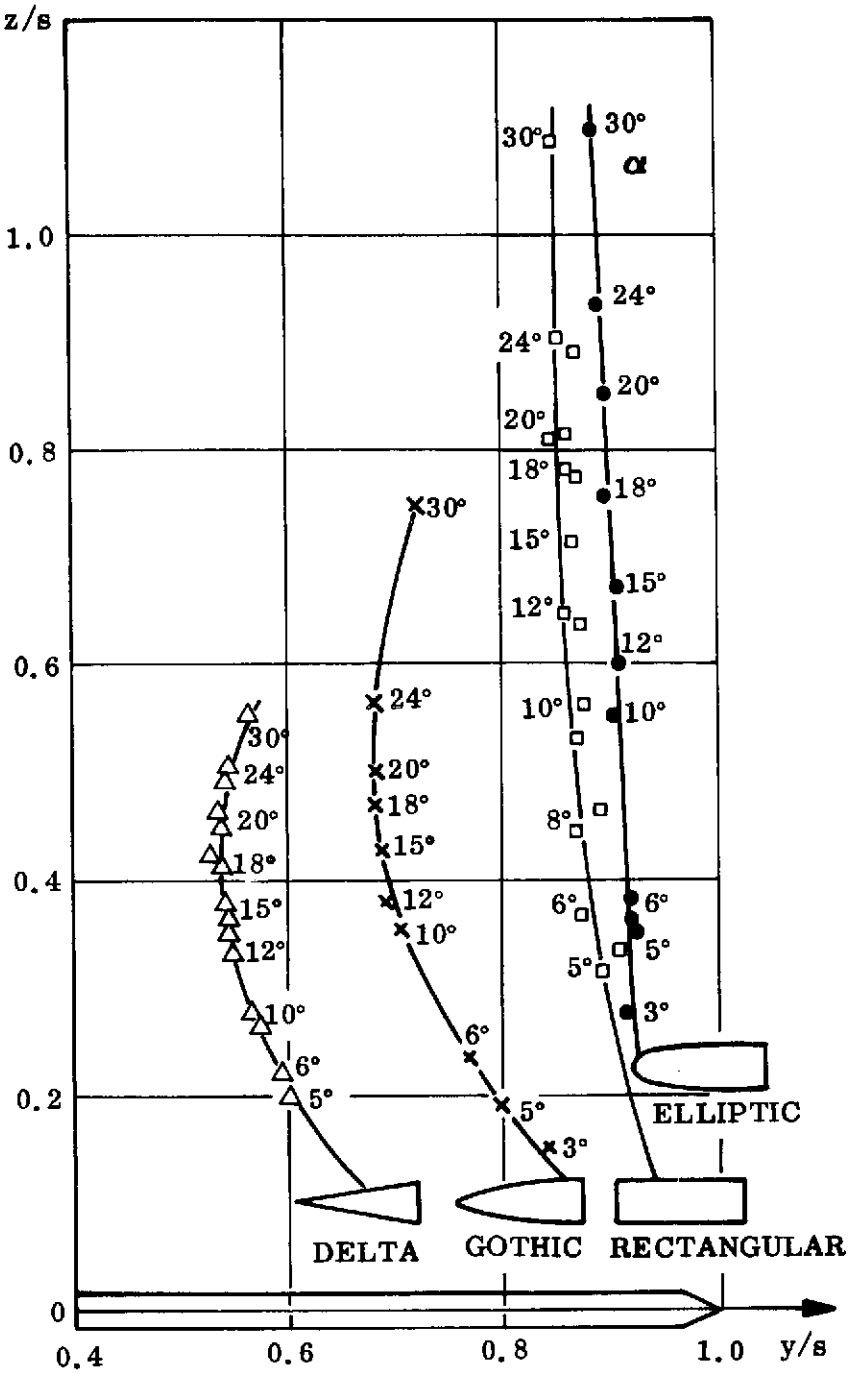

Figure 48. Spanwise Vortex Position at the Trailing Edge of Slender Sharp-Edged Wings (Ref. 72)

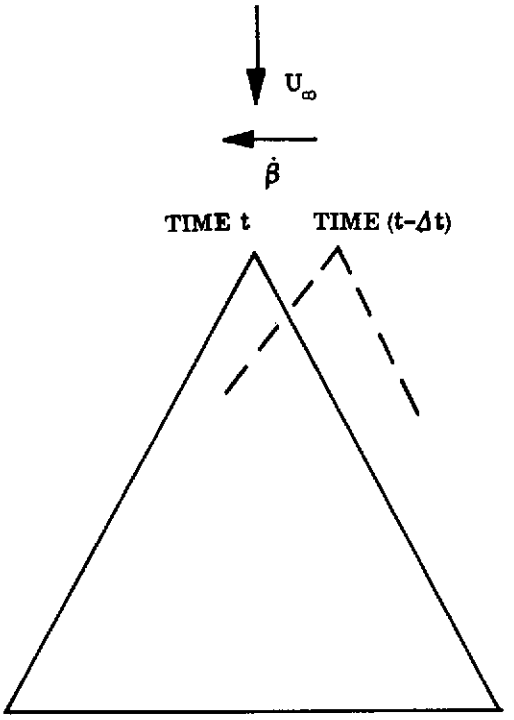

a. SIDESLIPPING DELTA WING

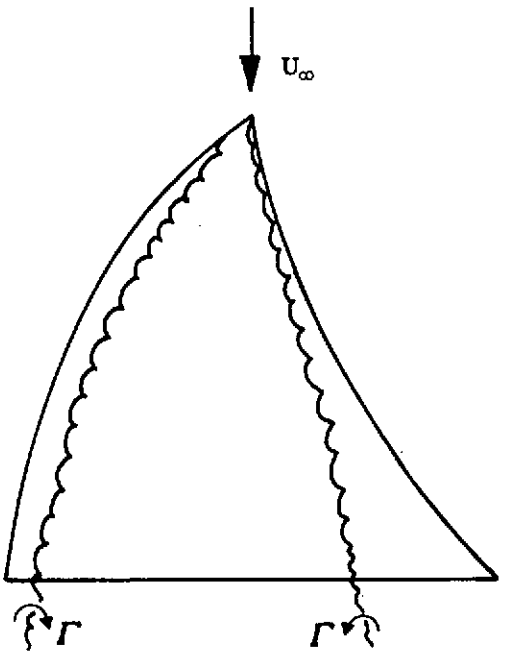

b. EQUIVALENT QUASI-STEADY WING

Figure 49. Quasi-Steady Equivalence for a Side-Slipping Delta Wing

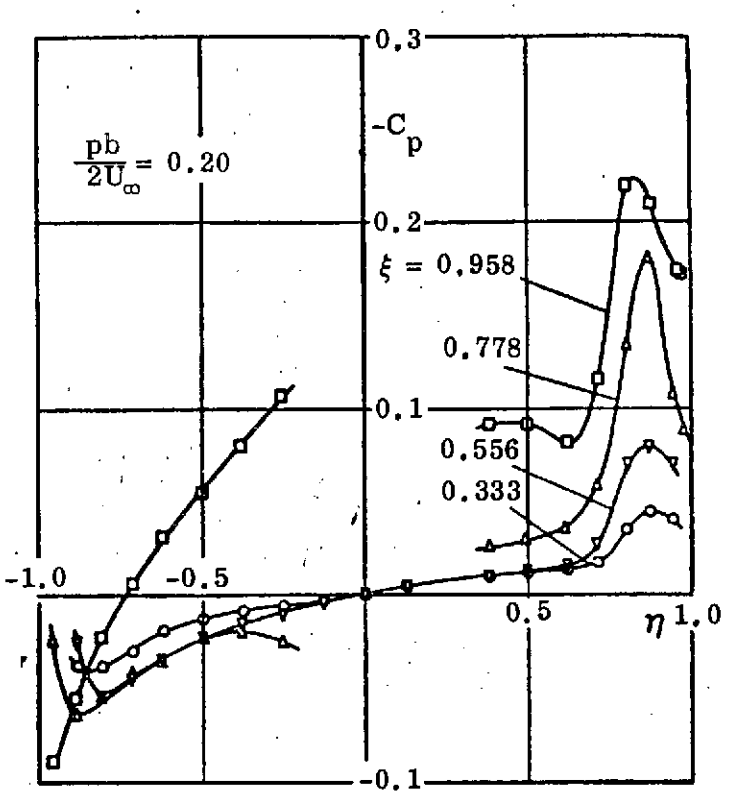

Figure 50. Roll-Induced Vortex Loads on an A = 0.7 Sharp-Edged Delta Wing at α = 0 (Ref. 74)

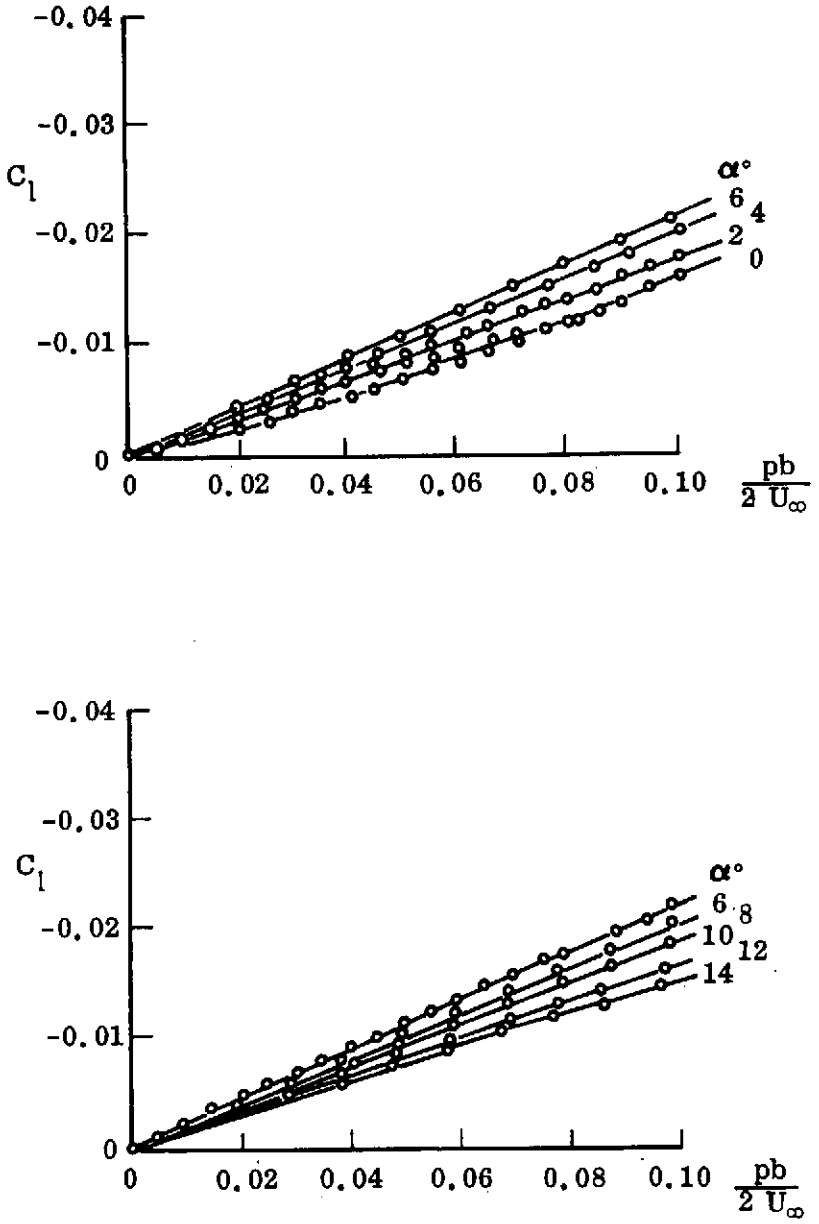

Figure 51. Effect of Roll Rate and α_o on the Rolling Moment of an A = 1 Sharp-Edged Delta Wing (Ref. 75)

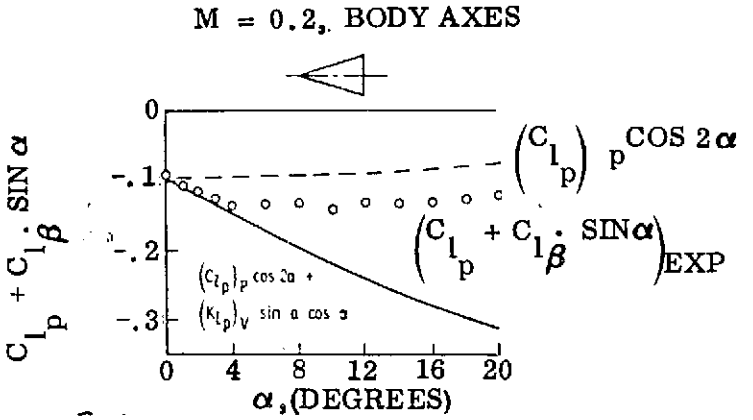

a. COMPARISON OF THEORY AND EXPERIMENT FOR 74° SWEEP DELTA WING

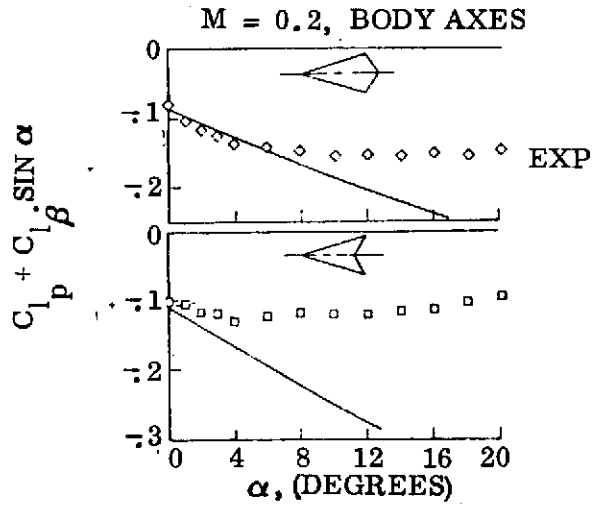

b. COMPARISON OF THEORY AND EXPERIMENT FOR 74° SWEEP DIAMOND AND ARROW WINGS

Figure 52. Roll Damping of Slender Wings (Ref. 76)

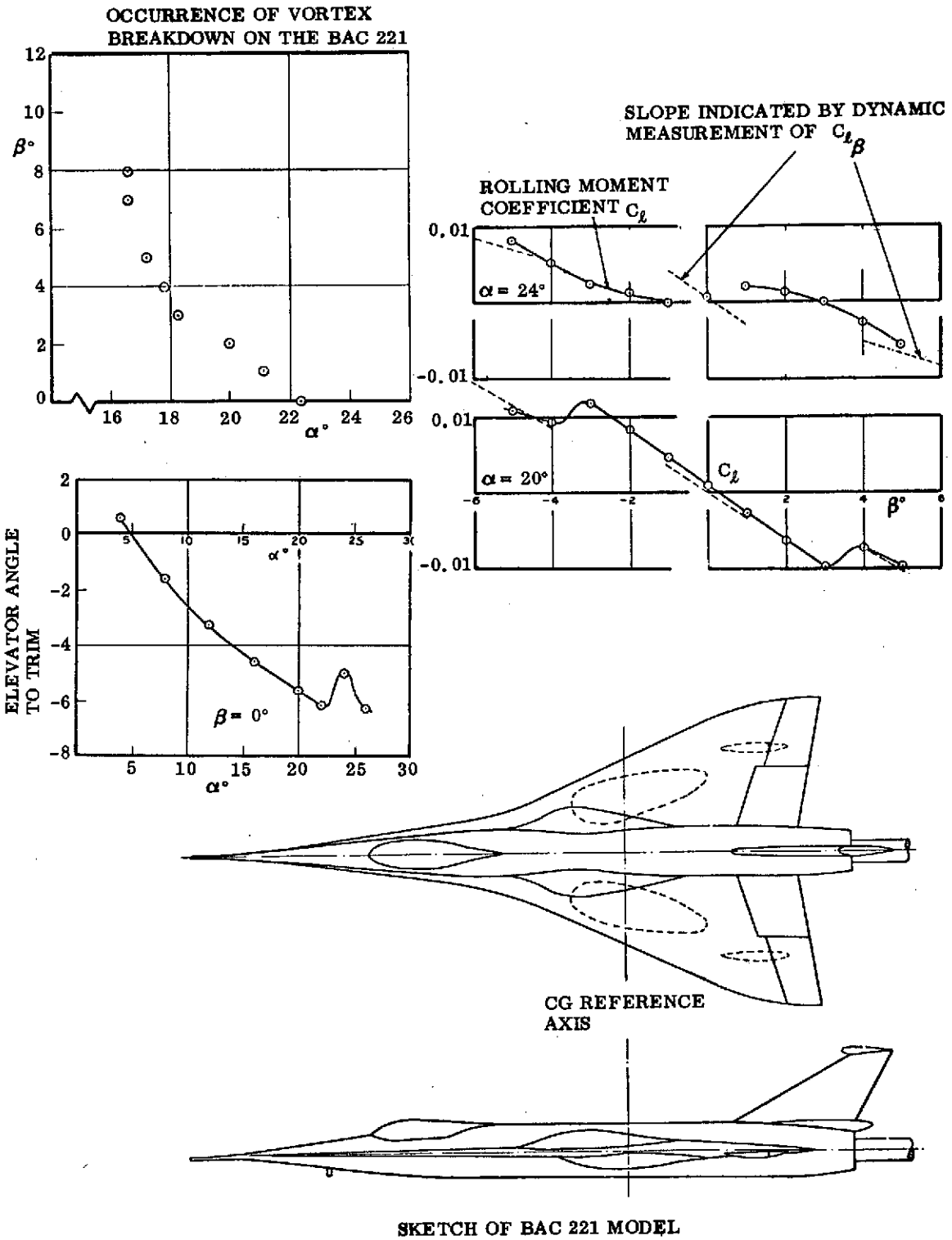

Figure 53. Slender Aircraft Lateral Stability Characteristics (Ref. 77)

Section 3
CONCLUSIONS

A study of the steady and unsteady aerodynamics of sharp-edged slender wings has shown the following:

- Through a simple modification, Jones' slender wing theory can give the potential flow static loads for M = O.
- A redistribution of Polhamus' vortex lift, based on experimental data, provides improved prediction of the aerodynamic center.
- The present analytic approximation provides consistently good predictions of static aerodynamic characteristics also for swept trailing edges (forward or back).
- Based upon the present analytic approximation, universal scaling concepts have been developed that collapse experimental lift and rolling moment data to the accuracy needed for preliminary design. When better accuracy is needed, the analytic approximation will give it very inexpensively on a digital computer.
- The present analytic approximation gives good prediction of experimental data at M = O and M = 1. Simple means could be developed to handle the compressibility effects in the interim speed range, $O<M<1$.
- The slender wing unsteady aerodynamics at small angles of attack, i.e., the attached flow characteristics, are obtained using first-order momentum theory at M = 1. At M = O, an equivalent wing is defined based on static characteristics, and first order momentum theory is applied to it. The predictions agree well with experimental data for aspect ratios up to A = 2.
- The effects of leading edge vortices on slender wing unsteady aerodynamics are obtained using Lambourne's simple convective timelag concept in combination with postulated vortex entrainment effects on the effective apparent mass. The agreement with available experimental data is good.

Section 4
RECOMMENDATIONS FOR FUTURE STUDY

The results obtained in the present study are very encouraging. However, they are based on empiricism. Static experimental data for an $A = 1.147$ delta wing was used to define the vortex lift distribution. The good agreement with experimental data for a wide A-range would indicate that the distribution as well as the total vortex lift is independent of aspect ratio. Before the empiricism can be removed, one has to understand in more quantitative detail why the vortex lift does not grow downstream of $\xi = 0.4$. Use of (α/θ_{LE})-correlation results for delta and nondelta planforms could provide the information needed to define how (and where) the tight vortex-leading edge connection is lost. To extend the present analysis to cover the intermediate Mach numbers between $M = 0$ and $M = 1$ should be a relatively simple matter.

The qualitative results obtained in the present study in regard to vortex-induced effects on lateral unsteady aerodynamics indicate that quantitive prediction methods can be developed. Whether or not the dependence upon static experimental data can be removed depends strongly on the success of predicting the observed (α/θ_{LE})-trends, the task described in the previous paragraph. One has reasons to believe that analytic prediction techniques can be developed that will handle the complicated pitch-yaw-roll coupling effects from leading edge vortices.

In the present analysis the unsteady aerodynamics of a delta wing describing bending oscillations in the chordwise plane were defined. One needs to develop the analytic tools for predictions of the unsteady aerodynamics for more general deformation shapes and to compare analytic predictions with available experimental data. Furthermore, motion-independent buffet forces and effects of atmospheric gusts have also to be considered before a complete analysis of the aeroelastic characteristics of slender wings is possible. The results obtained in the present study indicate that a complete analytic theory for the elastic slender wing can be developed without losing much of the simplicity inherent in the presented rigid-wing analysis.

REFERENCES

1. Runyan, H. L. and Reed, W. H., "Dynamics and Aeroelasticity - An Appraisal," Astronautics & Aeronautics, Vol. 9, No. 2, Feb. 1971, pp. 48-57.

2. Tischler, A. O., "Critical Areas - Thermal-Protection Systems, Vehicle Weights, and --- Aero-Elasticity," Astronautics & Aeronautics, Vol. 9, No. 8, Aug. 1971, p. 8.

3. Ericsson, L. E. and Reding, J. P., "Unsteady Aerodynamic Analysis of Space Shuttle Vehicles: Part I. Summary Report," LMSC D352320 Part I, Aug. 1973, Lockheed Missiles & Space Company, Inc., Sunnyvale, California

4. Polhamus, E. C., "A Concept of the Vortex Lift of Sharp-Edge Delta Wings Based on a Leading-Edge-Suction Analogy," NASA TN D 3767, Dec. 1966.

5. Polhamus, E. C., "Predictions of Vortex-Lift Characteristics by a Leading-Edge Suction Analogy," Journal of Aircraft, Vol. 8, No. 4, Apr. 1971, pp. 193–199.

6. Jones, R. T., "Properties of Low-Aspect-Ratio Pointed Wings at Speeds Below and Above the Speed of Sound," NASA Report No. 835, May 1945.

7. Peckham, O. H., "Low-Speed Wind-Tunnel Tests on a Series of Uncambered Slender Pointed Wings with Sharp Edges," R&M 3186, Aeronautical Research Council, Great Britain, Dec. 1958.

8. Earnshaw, P. B. and Lawford, J. A., "Low-Speed Wind-Tunnel Experiments on a Series of Sharp-Edged Delta Wings: Part 1. Forces, Moments, Normal-Force Fluctuations, and Positions of Vortex Breakdown," Tech. Note AERO 2780, Aeronautical Research Council, Great Britain, Aug. 1961.

9. Fink, P. T., "Some Low Speed Experiments with 20-Degree Delta Wings," Z. Flugwiss, Vol. 4, No. 7, pp. 247 – 249, July 1956.

10. Lawford, J. A. and Beauchamp, A. R., "Low-Speed Wind-Tunnel Measurements on a Thin Sharp-Edged Delta Wing with 70° Leading-Edge Sweep, with Particular Reference to the Position of Leading-Edge-Vortex Breakdown," R&M No. 3338, Aeronautical Research Council, Great Britain, Nov. 1961.

11. Bartlett, G. E. and Vidal, R. J., "Experimental Investigation of Influence of Edge Shape on the Aerodynamic Characteristics of Low Aspect Ratio Wings at Low Speeds," Journal of the Aeronautical Sciences, Vol. 22, No. 8, Aug. 1955, pp. 517 – 533.

12. Tosti, L. P., "Low Speed Static Stability and Damping-in-Roll Characteristics of Some Swept and Unswept Low-Aspect-Ratio Wings," NACA TN 1468, 1947.

13. Hummel, D., "Zur Umströmung scharfkantiger schlanker Deltaflügel bei grossen Anstellwinkeln," Z. Flugwiss, Vol. 15, No. 10, 1967, pp. 376 – 385.

14. Smith, J. H. B., "Improved Calculations of Leading-Edge Separation from Slender Delta Wings," RAE Tech. Rpt. No. 66070, Aeronautical Research Council, Great Britain, 1966.

15. Örnberg, T., "A Note on the Flow Around Delta Wings," KTH Aero TN 38, Royal Institute of Technology, Stockholm, Sweden, Feb. 1954.

16. Wentz, W. H. Jr., "Effects of Leading-Edge Camber on Low-Speed Characteristics of Slender Delta Wings," NASA CR 2002, 1972.

17. Margason, R. J. and Lamar, J. E., "Vortex-Lattice FORTRAN Program for Estimating Subsonic Aerodynamic Characteristics of Complex Planforms," NASA TND 6142, 1971.

18. Snyder, M. H., Jr., and Lamar, J. E., "Application of the Leading-Edge Suction Analogy to Prediction of Longitudinal Load Distribution and Pitching Moments for Sharp-Edged Delta Wings," NASA TND 6994, Aug. 1972.

19. Maltby, R. L., Engler, P. B., and Keating, R. F. A., with Addendum by Moss, G. F., "Some Exploratory Measurements of Leading-Edge Vortex Positions on a Delta Wing Oscillating in Heave," R&M 3176, Aeronautical Research Council, Great Britain, July 1963.

20. Elle, B. J., "An Investigation at Low Speed of the Flow Near the Apex of Thin Delta Wings with Sharp Leading Edges," R&M 3176, Aeronautical Research Council, Great Britain, Jan. 1958.

21. Parkinson, G. V., Sun, Y. C., and Davis, H. R., "Observations on Low Aspect Ratio Wings at High Incidence," Canadian Aeronautics and Space Journal, Vol. 13, March 1967, pp. 111 – 116.

22. Davenport, E. E. and Huffman, J. K., "Experimental and Analytical Investigation of Subsonic Longitudinal and Lateral Aerodynamic Characteristics of Slender Sharp-Edge 74° Swept Wings," NASA TND-6344, July 1971.

23. Stivers, L. S. and Levy, L. L., Jr., "Effects of Sting-Support Diameter on the Base Pressures of an Elliptic Cone at Mach Numbers from 0.60 to 1.40," NASA TND 354, Feb. 1961.

24. Reding, J. P. and Ericsson, L. E., "Dynamic Support Interference," Journal of Spacecraft and Rockets, Vol. 9, No. 7, May 1972, pp. 547 – 553.

25. Kraemer, K., "Kraft und Druckverteilungsmessungen an einem Deltaflügel bei inkompressibler Strömung und Vergleich mit der Theorie," Z. Flugwiss., Vol. 10, No. 8, Aug. 1962, pp. 297 – 305.

26. Wendtz, W. H. and Kohleman, D. L., "Vortex Breakdown on Slender Sharp-Edged Wings," AIAA Paper No. 69-778, July 1969.

27. Engler, P. B. E. and Moss, G. F., "Low-Speed Wind-Tunnel Tests on a 1/8th Scale Model of the Handley-Page HP 115," R&M No. 3486, Aeronautical Research Council, Great Britain, Aug. 1965.

28. Lambourne, N. C., "The Breakdown of Certain Types of Vortex," R&M No. 915, Aeronautical Research Council, Great Britain, Sept. 1965.

29. Bird, J., "Tuft-Grid Surveys at Low Speeds for Delta Wings," NASA TND 5045, Feb. 1969.

30. Hummel, D. and Redeker, G., "Über den Einfluss des Aufplatzens der Wirbel auf die aerodynamische Beiwerte von Deltaflügeln mit Kleinen Seitenverhältnis beim Schiebeflug," Jahrbuch der W. G. LR, 1967, pp. 232 – 240.

31. Hummel, D., "Untersuchungen uber das Aufplatzen der Wirbel an schlanken Deltaflügeln," Z. Flugwiss., Vol. 13, No. 5, May 1965, pp. 158 – 169.

32. Bisplinghoff, R. L., Ashley, H., and Halfman, R. L., Aeroelasticity. Addison-Wesley, Cambridge, Mass. 1955, pp 418 – 419.

33. Ericsson, L. E. and Reding, J. P., "Analysis of Flow Separation Effects on the Dynamics of a Large Space Booster," Journal of Spacecraft and Rockets, Vol. 2, No. 4, Jul – Aug. 1965, pp. 481 – 490.

34. Ericsson, L. E., Reding, J. P., and Guenther, R. A., "Launch Vehicle Gust Penetration Loads," Journal of Spacecraft and Rockets, Vol. 9, No. 1, Jan. 1973, pp. 19 – 25.

35. Ericsson, L. E., Reding, J. P., and Guenther, R. A., "Elastic Launch Vehicle Response to Sinusoidal Gusts," Journal of Spacecraft and Rockets, Vol. 10, No. 5, May 1973, pp. 244-252.

36. Woodgate, L., "Measurements of the Oscillatory Pitching Moment Derivatives on a Slender Sharp-Edged Delta Wing in Incompressible Flow," R&M No. 3628, Part 2, Aeronautical Research Council, Great Britain, July 1968.

37. Woodgate, L. and Pugh, P. G., "Measurements of the Pitching-Moment Derivatives on a Sharp-Edged Delta Wing in Incompressible Flow," R&M No. 3379, Aeronautical Research Council, Great Britain, 1963.

38. Woodgate, L. and Halliday, A. S., "Measurements of Lift, Drag, and Pitching Moments on a Series of Three Delta Wings," R&M No. 3628, Part 4, Aeronautical Research Council, Great Britain, July 1968.

39. Woodcock, D. L., "A Comparison of Methods Used in Lifting Surface Theory," AGARD Report No. 583, June 1971.

40. Lambourne, N. C., Bryer, D. W., and Maybrey, J. F. M., "A Preliminary Note on the Behavior of the Leading-Edge Vortices on a Delta Wing Following a Sudden Change of Incidence," NPL Aero Note 1006, Aeronautical Research Council, Great Britain, Nov. 1962.

41. Lambourne, N. C., Bryer, D. W., and Maybrey, J. F. M., "The Behavior of the Leading-Edge Vortices over a Delta Wing Following a Sudden Change of Incidence," R&M No. 3645, Aeronautical Research Council, Great Britain, March 1969.

42. Lambourne, N. C., Bryer, D. W., and Maybrey, J. F. M., "Pressure Measurements on a Model Delta Wing Undergoing Oscillatory Deformation," NPL Aero Report 1314, Aeronautical Research Council, Great Britain, March 1970.

43. Roberts, D. R. and Hunt, G. K., "Further Measurements of Transient Pressures on a Narrow Delta Wing due to a Vertical Gust," ARC C.P. No. 1012, Aeronautical Research Council, Great Britain, April 1966.

44. Randall, D. G., "A Theoretical Determination of the Flow Past and the Air Forces on an Oscillating Slender Delta Wing with Leading Edge Separation," RAE Report Structures 284, ARC 24910, Aeronautical Research Council, Great Britain, March 1963.

45. Ericsson, L. E. and Reding, J. P., "Unsteady Airfoil Stall," NASA CR 66787, July 1969.

46. Ericsson, L. E. and Reding, J. P., "Report on Saturn I - Apollo Unsteady Aerodynamics," LMSC A650215, Contract NAS 8-5338, Feb. 1964, Lockheed Missiles & Space Company, Inc., Sunnyvale, California

47. von Karman, Th. and Sears, W. R., "Airfoil Theory for Non-Uniform Motion," Journal Aeronautical Sci., Vol. 5, No. 10, Aug. 1938, pp. 379 – 390.

48. Ericsson, L. E. and Reding, J. P., "Unsteady Airfoil Stall, Review and Extension," Journal of Aircraft, Vol. 8, Aug. 1971, pp 609 – 616.

49. Lambourne, N. C. and Bryer, D. W., "The Bursting of Leading-Edge Vortices - Some Observations and Discussion of the Phenomenon," R&M No. 3282, Aeronautical Research Council, Great Britain, Apr. 1961.

50. Mabey, D. G. and Mitchell, C. G. B., Private Communication, Bedford, Great Britain, May 4, 1973.

51. Ericsson, L. E., "Report on Visits to European Research Institutes and Industry During May and June, 1972," LMSC TIC 2053, 23 June 1972, Lockheed Missiles & Space Company, Inc., Sunnyvale, California.

52. Keating, R. F. A., "Measurement of Pressures on a Delta Wing Oscillating in Heave at a High Angle of Incidence," RAE Report 67241, Aeronautical Research Council, Great Britain, 1967.

53. Rainbird, W. J., "Turbulent Boundary-Layer Growth and Separation on a Yawed Cone," AIAA Journal, Vol. 6, No. 12, Dec. 1968, pp. 2410 – 2416.

54. Rainbird, W. J., Crabbe, R. S., and Jurewicz, L. S., "A Water Tunnel Investigation of the Flow Separation About Circular Cones at Incidence," Aero. Report LR-385, National Research Council, National Aeronautical Establishment, Canada Sep. 1963.

55. Rainbird, W. J., "The External Flow Field about Yawed Circular Cones at Incidence," AGARD Conference Proceedings 30, May 1968.

56. Earnshaw, P. B., "An Experimental Investigation of a Leading Edge Vortex," R&M No. 3281, Aeronautical Research Council, Great Britain, March 1961.

57. Woodgate, L., "Measurements of the Oscillatory Pitching-Moment Derivatives on a Sharp-Edged Delta Wing at Angles of Incidence for which Vortex Breakdown Occurs," R&M No. 3628, Part 3, Aeronautical Research Council, Great Britain July 1968.

58. Ericsson, L. E., "Aeroelastic Instability Caused by Slender Payloads," Journal of Spacecraft and Rockets, Vol. 4, No. 1, Jan. 1967, pp. 65 – 73.

59. Reding, J. P. and Ericsson, L. E., "Review of Delta Wing Shuttle Dynamics," Journal of Spacecraft and Rockets, Vol. 10, No. 7, July 1973, pp. 421 – 428.

60. Hummel, D. and Srinivasan, P. S., "Vortex Breakdown Effects on the Low-Speed Aerodynamic Characteristics of Slender Delta Wings in Symmetrical Flow," J. Royal Aer. Soc., Vol. 71, No. 4, Apr. 1967, pp. 319 – 322.

61. Ericsson, L. D., "Separated Flow Effects on the Static and Dynamic Stability of Blunt Nosed Cylinder-Flare Bodies," LMSC 667991, Contract NAS 8-5338, Lockheed Missiles & Space Company, Inc., Sunnyvale, California, Dec. 1965

62. Ericsson, L. E., "Unsteady Aerodynamics of Separating and Reattaching Flow on Bodies of Revolution," Recent Research on Unsteady Boundary Layers, Vol. 1, IUTAM Symposium, Laval University, Quebec, 24 – 28 May 1971, pp. 481 – 512.

63. Ericsson, L. E. and Reding, J. P., "Dynamics of Separated Flow over Blunt Bodies," Technical Summary Report, LMSC 2-80-65-1, Contract NAS 8-5338, Lockheed Missiles & Space Company, Inc., Sunnyvale, California, Dec. 1965

64. Ericsson, L. E. and Reding, J. P., Re-Entry Capsule Dynamics," Journal of Spacecraft and Rockets, Vol. 8, No. 6, June 1971, pp. 575 – 586.

65. Sforza, P. M., "Aircraft Vortices Benign or Baleful?", Space-Aeronautics, Apr. 1970, pp. 42 – 48.

66. Wendtz, W. H. and Kohleman, D. L., "Vortex Breakdown on Slender Sharp-Edged Wings," AIAA Preprint No. 69-778, July 1969.

67. Lowson, M. V., "Some Experiments with Vortex Breakdown," J. Royal Aeronautical Society, Vol. 68, May 1964, pp. 343 – 346.

68. Tobak, M., Schiff, L. B., and Peterson, V. L., "Aerodynamics of Bodies of Revolution in Coning Motion," AIAA Journal, Vol. 7, No. 1, Jan. 1969, pp. 95 –99.

69. Schiff, L. B., "Preliminary Results from a New Wind-Tunnel Apparatus for Studying Coning and Spinning Motions of Bodies of Revolution," Paper 9, Vol. III, Trans. of the 3rd Technical Workshop on Dynamic Stability Problems, NASA Ames Research Center, Moffett Field, California, Nov. 4–7, 1968.

70. Schiff, L. B., "Nonlinear Aerodynamics of Bodies in Coning Motion," AIAA Journal, Vol. 10, No. 11, Nov. 1972, pp. 1517 – 1522.

71. Bisgood, P. L., "Results of Flight Tests on a Slender Wing Low Speed Research Aircraft," AGARD Report 535, May 1966.

72. Werlé, H., "Vortices from Very Slender Wings," La Recherche Aerospatiale, No. 109, Nov.–Dec. 1965, pp. 1–12.

73. Ericsson, L. E. and Reding, J. P., "Analysis of Flow Separation Effects on the Dynamics of a Large Space Booster," Journal of Spacecraft & Rockets, Vol. 2, No. 4, July–Aug. 1965, pp. 481–490.

74. Harvey, J. J., "A Study of the Flow Field Associated with a Steady-Rolling Slender Delta Wing," J. Royal Aeronautical Society, Vol. 68, No. 2, Feb. 1964, pp. 106–110.

75. Schlottmann, F., "Über die stationären und instationären aerodynamisch Beiwerte für die Rollbewegung schlanke Flügel," Ph.D. Thesis, Bochum, Germany, 1972.

76. Boyden, R. P., "Effects of Leading-Edge Vortex Flow on the Roll Damping of Slender Wings," Journal of Aircraft, Vol. 8, No. 7, July 1971, pp. 543-548.

77. O'Leary, C. O., "Low Speed Wind-Tunnel Measurements of the Oscillatory Lateral Aerodynamic Derivatives of a BAC 221 Model and Comparison of Results with Similar Concorde and H.P. 115 Data," R&M No. 3671, Aeronautical Research Council, Great Britain, May 1970.

Appendix A
NOMENCLATURE

A	aspect ratio, $A = b^2/S$
A(x)	apparent cross-sectional area
A_{TE}	inefficient wing area at M = 0 (Fig. 2)
b	wing span
$\bar{c}$	reference length (usually mean aerodynamic chrod for a delta wing)
c_o	slender wing root chord
D	elastic vehicle damping, Eq. (44) and Eq. (63)
d	ridig body damping, Eq. (45) and Eq. (64)
G(t)	forcing function due to atmospheric gusts, Eq. (44)
I	elastic vehicle aerodynamic inertia, Eq. (44) and Eq. (63)
i	rigid body aerodynamic inertia, Eq. (45) and Eq. (64)
J	momentum
K	elastic vehicle aerodynamic spring, Eq. (44) and Eq. (63)
k	rigid body aerodynamic spring, Eq. (45) and Eq. (64)
K_p, K_V	potential flow and vortex lift factors, Eq. (1)
K_1, K_2	constants, Eq. (52)
k_1	constant for α-dependence of vortex strength, Eq. (53)
L	lift: coefficient $C_L = L/(\rho_\infty U_\infty^2/2)S$
ℓ	rolling moment: coefficient $C_\ell = \ell/(\rho_\infty U_\infty^2/2)Sb$
M	Mach number
M_p	pitching moment: coefficient $C_m = M_p/(\rho_\infty U_\infty^2/2)S\bar{c}$

$\tilde{m}$	generalized mass, Eq. (39)
N	normal force: coefficient $C_N = N/(\rho_\infty U_\infty^2/2)S$
n	yawing moment: coefficient $C_n = n/(\rho_\infty U_\infty^2/2)Sb$
P(t)	generalized force
p	roll rate
p	static pressure: coefficient $C_p = (p - p_\infty)/(\rho_\infty U_\infty^2/2)$
q	pitch rate
q(t)	amplitude of normalized bending deflection, $\delta(x,t) = \phi(x)q(t)$
Re	Reynolds number based on c_o and freestream conditions
S	reference area (= projected wing area)
s	local semi-span
t	time
Δt	timelag
U	horizontal velocity ($U = \partial X/\partial t$)
$\tilde{U}$	convection velocity
W	vertical velocity ($W = \partial Z/\partial t$)
X	horizontal inertial space coordinate (Fig. 18)
x	axial body-fixed coordinate (Fig. 2 and Fig. 18)
y	spanwise body-fixed coordinate (Fig. 2)
Z	vertical inertial space coordinate (Fig. 18)
z	vertical body-fixed coordinate octogonal to the x-y plane (Fig. 29)
ζ	dimensionless z-coordinate, $\zeta = z/c_o$
α	angle of attack
α_o	trim angle of attack

β	sideslip angle
$\delta(x, t)$	elastic vehicle deflection, $\delta(x, t) = \phi(x)\, q(t)$ (See Fig. 18)
ϵ	vortex contribution to apparent mass, Eq. (67)
Γ	vortex strength
ζ	structural damping, fraction of critical damping, Eq. (39)
η	dimensionless y-coordinate, $\eta = y/s$
θ	angular perturbation (Fig. 18)
θ_c	cone half angle
θ_{LE}	apex half angle (Fig. 2)
θ_{TE}	trailing edge sweep angle (Fig. 2)
Λ	leading edge sweep angle, $\Lambda = \pi/2 - \theta_{LE}$
ξ	dimensionless x-coordinate, $\xi = (x_A - x)/c_o$
ρ	air density
ϕ	phase angle
$\Delta\phi$	phase lag
$\phi(x)$	x-distribution of normalized bending deflection, $\delta(x, t) = \phi(x)\, q(t)$
ω	free-free bending frequency and rigid body pitching frequency
$\bar{\omega}$	reduced frequency, $\bar{\omega} = \omega_o/U_\infty$

Subscripts

A	apex
a	attached flow
AC	aerodynamic center
b	buffet
CG	center of gravity
d	discontinuity

Subscripts, (Continued)

eff	effective
LE	leading edge
max	maximum
N or $\perp$	normal to leading edge
n	harmonic component
g	gust
s	separated flow
TE	trailing edge
V	vortex
VB	vortex burst
1,2,3...	numbering subscript
∞	freestream conditions

Superscripts

(*)	trailing edge coordinate, Eqs. (8) and (9)
(')	prime denoting x-derivative, e.g., $\phi' = \partial\phi/\partial x$
(-)	barred quantities denote integrated mean values, e.g., centroid of aerodynamic loads

Differential Symbols

$$\dot{\theta} = \partial\theta/\partial t \; ; \; \ddot{\theta} = \partial^2\theta/\partial t^2$$

$$C_{L\alpha} = \partial C_L/\partial\alpha \; ; \; C_{\ell\beta} = \partial C_\ell/\partial\beta \; ; \; C_{m_\theta} = \partial C_m/\partial\theta$$

$$C_{m_{\dot{\theta}}} = C_{mq} + C_{m\dot{\alpha}} = \partial C_m/\partial(\bar{c}\dot{\theta}/U_\infty): \; C_{mq} = \partial C_m/\partial(\bar{c}q/U_\infty):$$

$$C_{m_{\ddot{\theta}}} = \partial C_m/\partial(\bar{c}\ddot{\theta}/U_\infty^2)$$

$$C_{\ell_p} = \partial C_\ell/\partial(bp/2\,U_\infty) : \; C_{\ell_{\dot{\beta}}} = \partial C_\ell/\partial(b\dot{\beta}/2\,U_\infty)$$